

VOLUME 35

OCTOBER 1957

NUMBER 10

# Canadian Journal of Physics

*Editor:* H. E. DUCKWORTH

*Associate Editors:*

L. G. ELLIOTT, *Atomic Energy of Canada, Ltd., Chalk River*

J. S. FOSTER, *McGill University*

G. HERZBERG, *National Research Council of Canada*

L. LEPRINCE-RINGUET, *Ecole Polytechnique, Paris*

B. W. SARGENT, *Queen's University*

G. M. VOLKOFF, *University of British Columbia*

W. H. WATSON, *University of Toronto*

G. A. WOONTON, *McGill University*

*Published by* THE NATIONAL RESEARCH COUNCIL  
OTTAWA CANADA

## CANADIAN JOURNAL OF PHYSICS

(Formerly Section A, Canadian Journal of Research)

Under the authority of the Chairman of the Committee of the Privy Council on Scientific and Industrial Research, the National Research Council issues THE CANADIAN JOURNAL OF PHYSICS and five other journals devoted to the publication, in English or French, of the results of original scientific research. Matters of general policy concerning these journals are the responsibility of a joint Editorial Board consisting of: members representing the National Research Council of Canada; the Editors of the Journals; and members representing the Royal Society of Canada and four other scientific societies.

### EDITORIAL BOARD

#### Representatives of the National Research Council

R. B. Miller, *University of Alberta*  
H. G. Thode, *McMaster University*

D. L. Thomson, *McGill University*  
W. H. Watson (Chairman), *University of Toronto*

#### Editors of the Journals

D. L. Bailey, *University of Toronto*  
T. W. M. Cameron, *Macdonald College*  
H. E. Duckworth, *McMaster University*

K. A. C. Elliott, *Montreal Neurological Institute*  
Léo Marion, *National Research Council*  
R. G. E. Murray, *University of Western Ontario*

#### Representatives of Societies

D. L. Bailey, *University of Toronto*  
Royal Society of Canada  
T. W. M. Cameron, *Macdonald College*  
Royal Society of Canada  
H. E. Duckworth, *McMaster University*  
Royal Society of Canada  
Canadian Association of Physicists

K. A. C. Elliott, *Montreal Neurological Institute*  
Canadian Physiological Society  
R. G. E. Murray, *University of Western Ontario*  
Canadian Society of Microbiologists  
H. G. Thode, *McMaster University*  
Chemical Institute of Canada  
T. Thorvaldson, *University of Saskatchewan*  
Royal Society of Canada

#### Ex officio

Léo Marion (Editor-in-Chief), *National Research Council*  
F. T. Rosser, Vice-President (Administration and Awards), *National Research Council*

---

*Manuscripts* for publication should be submitted to Dr. H. E. Duckworth, Editor, Canadian Journal of Physics, Hamilton College, McMaster University, Hamilton, Ontario.

(For instructions on preparation of copy, see **Notes to Contributors** (inside back cover).)

*Proof, correspondence concerning proof, and orders for reprints* should be sent to the Manager, Editorial Office (Research Journals), Division of Administration and Awards, National Research Council, Ottawa 2, Canada.

*Subscriptions, renewals, requests for single or back numbers, and all remittances* should be sent to Division of Administration and Awards, National Research Council, Ottawa 2, Canada. Remittances should be made payable to the Receiver General of Canada, credit National Research Council.

The journals published, frequency of publication, and prices are:

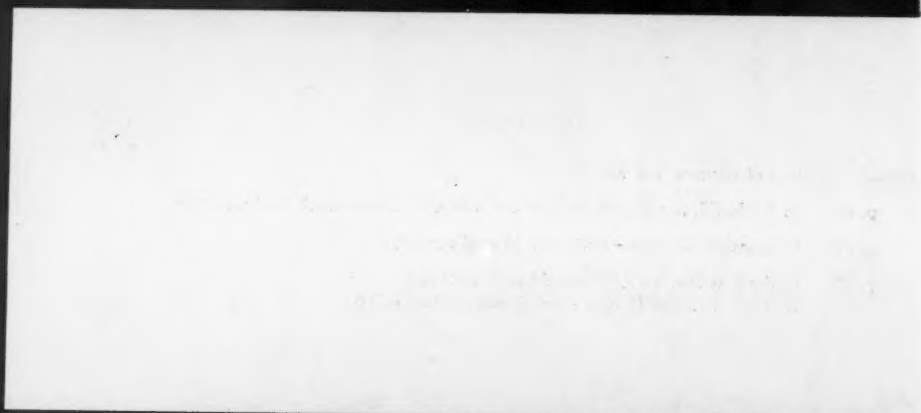
Canadian Journal of Biochemistry and Physiology	Monthly	\$3.00 a year
Canadian Journal of Botany	Bimonthly	\$4.00 a year
Canadian Journal of Chemistry	Monthly	\$5.00 a year
Canadian Journal of Microbiology	Bimonthly	\$3.00 a year
Canadian Journal of Physics	Monthly	\$4.00 a year
Canadian Journal of Zoology	Bimonthly	\$3.00 a year

The price of single numbers of all journals is 75 cents.

#### CORRECTION

Canadian Journal of Physics, Vol. 35.

- p. 972. In Table III, last line,  $8.20 \times 10^{13}$  and  $8.28 \times 10^{13}$  should both read  $6.8 \times 10^{13}$ .
- p. 976. In equation (4),  $\exp(-n\sigma_a\lambda)$  should read  $\exp(n\sigma_a\lambda)$ .
- p. 977. In the first line,  $8.6 \times 10^{13}$  should read  $6.8 \times 10^{13}$ .  
In Table VII, line B,  $5.19 \times 10^{16}$  should read  $5.19 \times 10^{15}$ .





# Canadian Journal of Physics

Issued by THE NATIONAL RESEARCH COUNCIL OF CANADA

VOLUME 35

OCTOBER 1957

NUMBER 10

## THE DECAY OF $\text{Os}^{185}$ <sup>1</sup>

M. W. JOHNS, S. V. NABLO,<sup>2</sup> AND W. J. KING<sup>3</sup>

### ABSTRACT

A study of the decay of  $\text{Os}^{185}$  with a magnetic beta-ray spectrometer, scintillation counters, and coincidence circuits reveals radiations of the following energies (in Mev.), intensities, and multiplicities:  $K$ -shell X-rays (65%), 0.0716 (0.4%,  $M1+E2$ ), 0.1255 (2.5%,  $M1+E2$ ), 0.1626 (1%,  $M1$ ), 0.2334 (1.4%,  $E2$ ), 0.5920 (1.1%,  $E2$ ), 0.6458 (80%,  $E2$ ), 0.7177 (4.1%,  $M1+E2$ ), 0.8720 (7.1%,  $M1+E2$ ), and 0.8789 (7.5%,  $M1+E2$ ). These transitions are interpreted in terms of a decay scheme involving the following levels in  $\text{Re}^{185}$ : 0(5/2+), 0.1255(7/2+), 0.6458(1/2+), 0.7176(3/2+), 0.872(3/2+), and 0.879(3/2+) Mev.

The ratio of  $L$ -capture to  $K$ -capture considering decay to all levels of  $\text{Re}^{185}$  is  $0.38 \pm 0.07$ . The ratio of  $L$ -capture to  $K$ -capture to the 0.872 and 0.879 Mev. levels is  $1.04 \pm 0.04$ . This implies that the  $\text{Os}^{185}$ - $\text{Re}^{185}$  atomic energy difference is  $0.985 \pm 0.007$  Mev. The half-life of  $\text{Os}^{185}$  was found to be  $93.6 \pm 0.5$  days.

### INTRODUCTION

The osmium  $n$ - $\gamma$  reaction leads to three activities: 94-day  $\text{Os}^{185}$ , 15-day  $\text{Os}^{191}$ , and 32-hour  $\text{Os}^{193}$ . Each of these decay processes is rich in gamma-ray transitions and the total spectrum is further complicated by the presence of the stronger lines of  $\text{Ir}^{192}$  and  $\text{Ir}^{194}$  which appear even with sources of "specpure" (i.e. total impurity less than 0.005%) osmium metal. Since both of the iridium spectra had been carefully studied in this laboratory (Johns and Nablo 1954) and since some of the radiations ascribed by earlier workers to osmium were due to this impurity, it was felt that a careful study of the osmium spectra with the same equipment which had been used for iridium would prove profitable. This paper will deal only with  $\text{Os}^{185}$ ; subsequent papers will discuss the results obtained for the two shorter-lived nuclides.

The experiments of Goodman and Pool (1947) and Katzin and Poberskin (1948) established that  $\text{Os}^{185}$  decayed by orbital electron capture to  $\text{Re}^{185}$  with a half-life of  $94.7 \pm 2$  days. The complexity of the accompanying gamma-ray spectrum was revealed by the work of Bunker, Canada, and Mitchell (1950), Swan and Hill (1952), and Cork *et al.* (1953). Miller and Wilkinson (1951) showed that  $L$ -capture occurred in a significant fraction of the disintegrations while recently Pruett and Wilkinson (1955) have described a detailed study of the decay process in abstract form.

<sup>1</sup>Manuscript received in original form January 21, 1957, and, as revised, July 2, 1957.

Contribution from the Department of Physics, McMaster University, Hamilton, Ontario.

<sup>2</sup>Present address: Convair, Fort Worth, Texas.

<sup>3</sup>Recipient of an Imperial Oil Graduate Fellowship.

## APPARATUS AND METHOD

The internal and external conversion spectra associated with the decay of  $\text{Os}^{185}$  have been studied with a 50-cm. Siegbahn-type beta-ray spectrometer, adjusted to an instrumental resolution of 0.65% in momentum. External conversion electrons were produced in foils of gold or uranium with linear dimensions  $3.0 \times 0.8$  cm. and thicknesses ranging from 0.4 to  $10 \text{ mg./cm.}^2$ . The internal conversion spectrum was studied with sources of about the same superficial area mounted on  $40 \text{ }\mu\text{g./cm.}^2$  VYNS film. The instrument was calibrated, using the external conversion peak of the 0.6616 Mev.  $\text{Cs}^{137}$  radiation and the low-energy internal conversion lines of  $\text{Th B+C+C''}$ . Intensities were determined using a modification of the Deutsch formula (Johns and Nablo 1954).

The electron detector used in the instrument consisted of an anthracene crystal  $3 \times 1.5 \times 0.3$  cm. mounted directly on the face of a Dumont 6291 photomultiplier tube. The tube was operated within the gap of the spectrometer by shielding it with an Armco iron cylinder of wall thickness 1.3 cm. With this instrument it was possible to have 100% detection of 20 kev. electrons with a noise background of about 60 counts per minute. At energies above 100 kev., the background was less than 10 counts per minute.

Sources were prepared from "spec-pure" osmium metal by irradiation in the Brookhaven reactor for periods ranging from 3 days to 3 weeks. The gamma-ray sources consisted of three hollow quartz needles about 3 cm. long and 0.1 cm. in diameter, each containing about 150 mg. of finely divided metal whose effective density was roughly  $10 \text{ g./cm.}^3$ . These needles were fastened with glyptal to the back of the  $240 \text{ mg./cm.}^2$  aluminum sheet which served as a support for the gold or uranium radiators. The source-radiator assembly was inserted or removed from the spectrometer as a unit, thus maintaining a fixed source-radiator geometry over the entire period of 18 months during which measurements were taken. By following the decay of individual photoelectron peaks, it was possible to assign each radiation to its parent nuclide and at the same time to determine the half-life of each of the three activities under study. No chemistry was performed on these sources.

The material for beta sources was obtained by irradiation of quartz ampoules containing about 15 mg. of metal. These were crushed under concentrated nitric acid and heated gently until the metal went into solution. It was necessary to be very careful to avoid volatilization of the toxic osmium tetroxide. Beta-sources prepared by evaporation from this solution were found to be reasonably uniform and to give well-defined conversion peaks without much low-energy straggling at energies above 60 kev. Sources prepared in this way all showed the stronger conversion lines of the  $\text{Ir}^{192}$  spectrum. It seemed wiser to accept this contaminant than to reduce the specific activity of the source material by carrying out a further purification process.

Since it was felt that the  $\gamma$ - $\gamma$  coincidences from the iridium contaminant might cause considerable confusion in the interpretation of the osmium coincidence data, the source material used for coincidence experiments was

repurified by a method due to Meinke (1949). The active osmium was placed in a flask and covered with perchloric acid. When the flask was heated gently and oxygen bubbled through the mixture, the osmium was removed as either osmium sesquioxide or osmium tetroxide. These oxides were carried over with the gas into a test tube containing magnesium chips and hydrochloric acid and there reduced to metallic osmium. After the reduction was complete, the excess magnesium was dissolved by the addition of further acid and the solution centrifuged to separate the osmium. Suitable scintillation counters were used to measure the intensity of the *K*-shell X-rays, to measure the internal conversion coefficient of the 0.646 Mev. radiation, to study  $\gamma$ - $\gamma$  coincidences, and to compare the number of *K*- and *L*-shell vacancies produced in rhenium. Whenever possible the measurements were made to depend on a comparison between the radiations of Os<sup>185</sup> and those of Cs<sup>137</sup> whose relative intensities are well known.

The intensity of the 0.06 Mev. X-rays from Re<sup>185</sup> was compared with the 0.646 Mev. radiation, using a NaI(Tl) crystal 5 cm. thick and 3.8 cm. in diameter. Since the detection efficiency of such a crystal is dependent on both gamma-ray energy and source-crystal distance (Rietjens *et al.* 1955), the instrument was calibrated by placing a source of Cs<sup>137</sup> at the same distance from the crystal. The intensity of the 0.032 Mev. X-rays relative to the 0.661 Mev. quanta from the latter source is given by  $\alpha_K \omega_K = 0.0827 \pm 0.005$  (Heath and Bell 1952; Bergstrom 1955). The efficiency of detection of both the barium and rhenium X-rays is effectively 100%, except for small and readily made corrections for absorption in the aluminum housing covering the crystal, and for the iodine escape peaks, while the energies of the 0.646 and 0.661 Mev. radiations are so nearly equal that their detection efficiencies are the same. This comparison method therefore eliminates uncertainties in the intensity measurements caused by geometric factors.

The total internal conversion coefficient of the 0.646 Mev. radiation was also obtained by comparison with Cs<sup>137</sup>, using an anthracene crystal to compare the number of conversion electrons emitted by osmium and cesium sources placed at equal distances from the detector, and using NaI(Tl) detectors to make the gamma intensity measurement. The conversion electrons from a repurified osmium source were superimposed on a bremsstrahlung background, while the conversion electrons from the Cs<sup>137</sup> source were superimposed on a beta continuum. In the latter case subtraction of the background posed no difficulties, but in the former case it was necessary to determine the shape of the bremsstrahlung continuum alone by covering the source with 200 mg./cm.<sup>2</sup> of aluminum before the subtraction could be made.

Gamma-gamma and gamma-X-ray coincidence experiments were carried out using 5X3.8 cm. sodium iodide crystals coupled to 5819 photomultiplier tubes as detectors. These detectors were used in a coincidence circuit of the fast-slow type (Bell, Graham, and Petch 1952) with a resolving time of 0.01  $\mu$ sec. when recording gamma-X-ray coincidences. In order to obtain sufficient amplification for the 60 kev. X-rays, the photomultipliers were operated at

1600 v., and the output pulses clipped and then fed to two Hewlett Packard wide-band amplifiers in cascade. The side-channel pulses were taken from the fifth dynode of the photomultiplier and energy selection was carried out with two Tracerlab pulse height analyzers. Under these conditions of operation the side-channel pulse heights were not a linear function of the gamma-ray energy, but this lack of linearity caused no difficulty in interpreting the results.

The osmium source was mounted in a hole in an anti-Compton shield (Bell 1955) and the source-detector geometry so arranged that neither crystal could see more than the edge of the other through the hole. These precautions were found to be very necessary because the backscattered Compton radiation following scattering of the strong 872-878 kev. doublet in one detector has an energy distribution in the region of the weak 163 and 233 kev. gamma rays. In earlier experiments carried out without the shield the true coincidences were seriously masked by the scattering effects. With the arrangement used, the solid angle subtended by the source at each crystal was about 0.5 steradian and the gamma-gamma coincidence rates recorded were quite low ( $\sim 5$  counts per minute). In order to avoid pile-up effects due to the strong X-ray component from the source, the detectors were covered with 0.5 g./cm.<sup>2</sup> tin sheeting except when gamma-X-ray coincidences were to be recorded. The rates for these coincidences were two to three orders of magnitude greater than the gamma-gamma rates.

The number of K-shell vacancies was determined by placing very small grains of active metal (about 1  $\mu$  in diameter) between two sodium iodide crystals each 0.3 cm. thick and 2 cm. in diameter. The two crystals were then optically coupled to each other and to a 6292 photomultiplier with silicone oil. In this arrangement, both the X-rays and Auger electrons contributed to the pulse and hence a comparison of the *L* and *K* peaks provided a direct measurement of the ratio of *L*- to *K*-shell vacancies without the necessity of using fluorescent yields or the number of *L*-shell vacancies created by a *K*-shell vacancy.

The measured *K*-shell internal conversion coefficients were compared directly with the values tabulated by Sliv (1956). Sliv's calculations for the *K*-shell include corrections for the finite size of the nucleus and should represent a significant improvement over the more extensive tables of Rose and his collaborators (1955, 1956), which ignore this parameter. Since Rose's *K/L* ratios are presumably reasonably independent of the nuclear radius, the measured *L*-shell coefficients were compared with values obtained by combining Sliv's *K*-shell coefficients with Rose's *K/L* ratios.

#### EXPERIMENTAL RESULTS

The decay of the strong 0.646 Mev. radiation was followed with the beta spectrometer for about a year (four half-lives). Throughout this period the three osmium needles forming the source were left attached to the backing of the 10 mg./cm.<sup>2</sup> uranium radiator. From the slope of the semilogarithmic plot of peak-height versus time, the half-life was determined to be  $93.6 \pm 0.5$  days.

A typical external conversion spectrum for the momentum region above 2500 gauss-cm. is shown in Fig. 1. In addition to the gross features of the spectrum which have been observed by several workers, evidence is presented

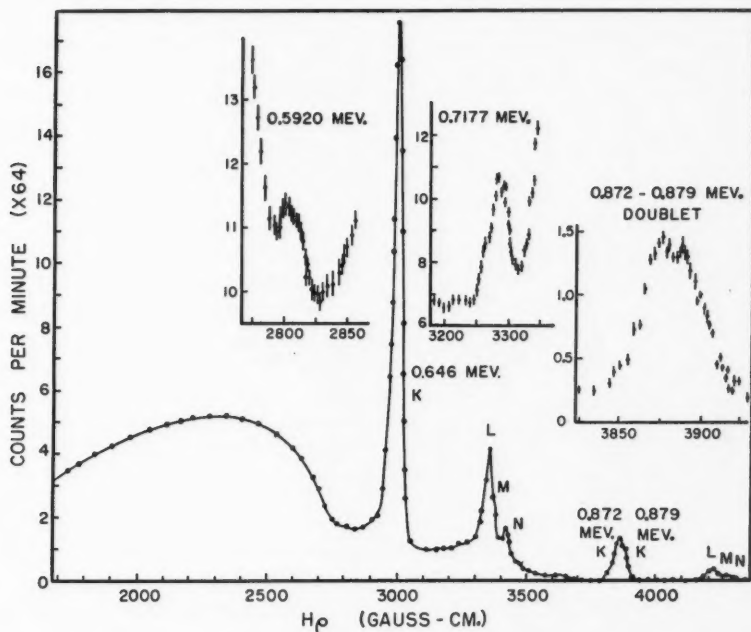


FIG. 1. Conversion electron spectrum of  $\text{Os}^{185}$  produced in a 10.3 mg./cm.<sup>2</sup> uranium radiator. Inserts show details of the weak 0.592 and 0.7177 Mev. photopeaks. The 0.872-0.879 Mev. doublet profile as obtained with a 1.8 mg./cm.<sup>2</sup> uranium radiator is also shown.

for the weak 0.5920 and 0.7177 Mev. radiations and for the 0.872-0.879 Mev. doublet. Although only partially resolved with the 10 mg./cm.<sup>2</sup> radiator, it was possible to make accurate energy and intensity measurements of both its components by graphical analysis using the well-known profile of the 0.8854 Mev. radiation of  $\text{Ir}^{192}$  which had been examined earlier (Johns and Nablo 1954) with the same equipment.

Portions of the low-energy external conversion spectrum are shown in Fig. 2. By an appropriate choice of radiator material and thickness, it was possible to disentangle the photopeaks of the weak radiations of energy 0.1255 and 0.2334 Mev. from the X-ray photopeaks and the  $\text{Os}^{191}$  lines which abound in this region. The line profiles for these weak peaks were drawn by comparison with the strong  $\text{Os}^{191}$  peaks which fall nearby.

The K-peak of the 0.1626 Mev. radiation is masked by X-ray peaks in the uranium conversion spectrum; it was only possible to set an upper limit on its intensity from the search conducted with a gold radiator.

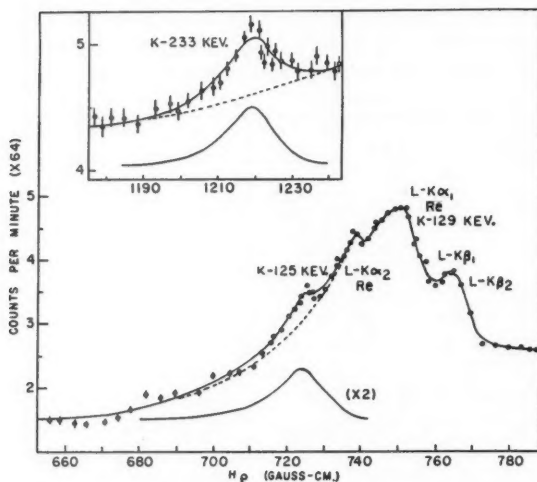


FIG. 2. The low-energy conversion electron spectrum of  $\text{Os}^{185}$  produced with  $400 \mu\text{g./cm.}^2$  gold foil. The insert shows the 0.2334 Mev. gamma-ray photopeak obtained with a  $1.8 \text{ mg./cm.}^2$  uranium radiator.

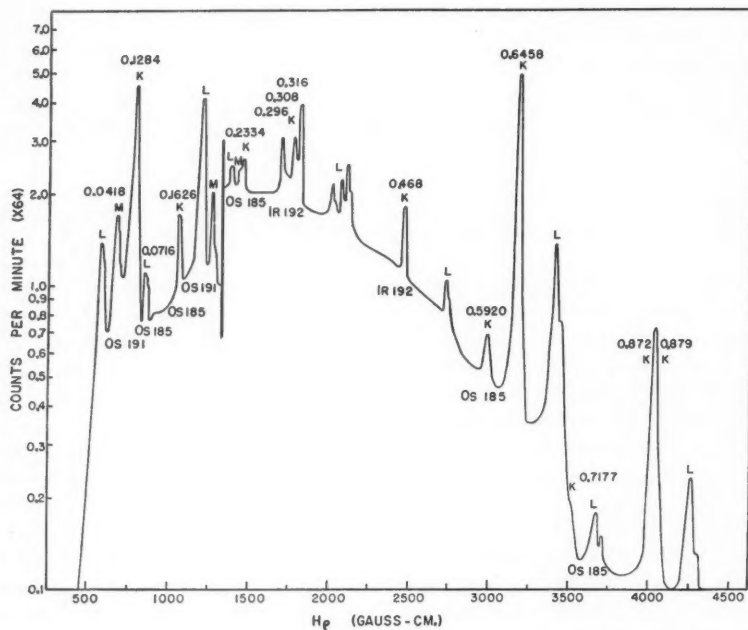


FIG. 3. Internal conversion spectrum of  $\text{Os}^{185}$  and  $\text{Os}^{191}$ . The spectrum below  $H_p$  1300 gauss-cm. was recorded four months after the high-momentum region. The weak continuum in the high-momentum region is due to  $\text{Ir}^{192}$  contaminant.

Fig. 3 shows a semilogarithmic representation of the internal conversion electron spectrum of  $\text{Os}^{185}$ , together with the more prominent features of the  $\text{Os}^{191}$  spectrum. The  $\text{Ir}^{192}$  accounts for a few of the conversion lines and all of the continuum above  $H\rho$  1500 gauss-cm. Although the region below  $H\rho$  1300 gauss-cm. was obtained 4 months after the higher energy portion, the  $\text{Os}^{191}$  spectrum is still dominant. Internal conversion lines are in evidence for all the gamma rays observed in external conversion except the 0.1255 Mev. transition; its peaks converted in rhenium fall directly beneath the strong conversion lines of the 0.129 Mev. radiation associated with 15-day  $\text{Os}^{191}$ . Although the decay of the 0.129 Mev.  $K$ -conversion peak was followed for 120 days (eight half-lives), the 0.1255 Mev. conversion line was still not evident. By this time the counting rates were so low that it was impossible to set more than an upper limit on its intensity. In addition, the internal conversion spectrum shows the weak  $L$ -peaks of the 0.0716 Mev. transition with sufficient resolution to estimate the  $L_1:L_2:L_3$  ratio, and the  $K$  and  $L$  conversion lines of the 0.1626 Mev. radiation.

The results of these measurements are presented in Table I. The transition energies given are based chiefly on external conversion data. At least four independent determinations of the energy were made for each radiation except the 0.5920 and 0.1255 Mev. transitions. For these, only two measurements were made. The errors quoted represent probable errors in the mean arbitrarily increased by a factor of 2 to allow for systematic errors of calibration. The relative gamma-ray intensities are normalized to 100 for the strong 0.6458 Mev. radiation, while the conversion electrons are normalized to 111 for the  $K$ -conversion peak of the same transition. The rather large errors on the intensities of some of the lines reflect their weakness or their incomplete resolution from other peaks. The intensities quoted for the 0.1255 and 0.1626 Mev. radiations are estimates based chiefly on the coincidence measurements. The  $K$ -shell X-ray intensity was obtained from scintillation counter measurements.

To obtain the values of  $\alpha_K$  and  $\alpha_L$  from these data, it was necessary to relate the two intensity scales by making an absolute determination of one conversion coefficient. The total conversion coefficient of the strong 0.646 Mev. radiation was therefore measured by comparison with that of the 0.661 Mev. radiation of  $\text{Cs}^{137}$  in the manner already described. Using the value of  $0.117 \pm 0.005$  (Heath and Bell 1952; Bendel *et al.* 1952) for the latter radiation, a value of  $0.017 \pm 0.003$  was obtained for the 0.646 Mev. transition. This value, when combined with the value of  $\alpha_T/\alpha_K$  obtained with the spectrometer, leads to  $\alpha_K = 0.013 \pm 0.003$ . This value and the measured  $K/L$  ratio are both consistent with the theoretical value for an  $E2$  transition and no other. It was therefore decided to accept this assignment as correct, and to normalize the two sets of intensities to give Sliv's (1956) theoretical value, 0.0111, for the 0.646 Mev. transition.

Although the internal conversion coefficients of Table I are not very precisely known, it has been possible to use them to make unique multipole assignments in most cases. All of the transitions appear to be  $M1$  or  $E2$ , or mixtures of



TABLE I  
TRANSITIONS IN  $\text{Re}^{185}$

Energy of photon in kev.	Relative quantum intensity	Relative conversion electron intensities		$\alpha_K$	$\alpha_L$	Multipole assignment	Transition probability, %	Transition assignment
		$N_K$	$N_L$					
<i>K</i> X-rays								
71.6 $\pm$ 0.3	82 $\pm$ 9	—	—	—	—	—	64.7 $\pm$ 8 <sup>1</sup>	—
125.5 $\pm$ 0.4	0.8 $\pm$ 0.4 <sup>3</sup>	<50	36 $\pm$ 20 <sup>2</sup>	—	—	M1+E2	0.4	E $\rightarrow$ D
162.6 $\pm$ 0.2	0.8 $\pm$ 0.4 <sup>4</sup>	33 $\pm$ 3	8 $\pm$ 2	<1.25	—	M1+E2	2.5 $\pm$ 1.5	B $\rightarrow$ A
233.4 $\pm$ 0.6	1.5 $\pm$ 0.4	15 $\pm$ 4	5 $\pm$ 3	0.41	0.10	M1	1	G $\rightarrow$ E
592.0 $\pm$ 0.4	1.3 $\pm$ 0.3	2.1 $\pm$ 0.4	— <sup>5</sup>	0.10	0.033	E2	1.4	G $\rightarrow$ D
645.8 $\pm$ 0.3	100 <sup>6</sup>	111 <sup>6</sup>	30 $\pm$ 4	1.6 $\times$ 10 <sup>-2</sup>	—	E2	1.1	E $\rightarrow$ B
717.7 $\pm$ 0.5	5.1 $\pm$ 0.5	3.4 $\pm$ 1	1.6 $\pm$ 0.5	1.11 $\times$ 10 <sup>-2</sup>	0.30 $\times$ 10 <sup>-2</sup>	E2	80	D $\rightarrow$ A
872.0 $\pm$ 1.5	8.9 $\pm$ 0.6	8.3 $\pm$ 1.5	1.2 $\pm$ 0.6	6.7 $\times$ 10 <sup>-3</sup>	3.1 $\times$ 10 <sup>-3</sup>	M1+E2	4.1	E $\rightarrow$ A
878.9 $\pm$ 1.0	9.4 $\pm$ 0.6	6.0 $\pm$ 1.0	1.7 $\pm$ 1	1.0 $\times$ 10 <sup>-2</sup>	1.3 $\times$ 10 <sup>-3</sup>	M1+E2	7.1	F $\rightarrow$ A
				6.4 $\times$ 10 <sup>-3</sup>	1.8 $\times$ 10 <sup>-3</sup>	M1+E2	7.5	G $\rightarrow$ A

<sup>1</sup>This includes *K*-shell X-rays from capture and internal conversion; probability of *K*-capture is 67 $\pm$ 8, measured ratio of *L*- to *K*-capture is 0.38 $\pm$ 0.07.

<sup>2</sup> $L_1:L_2:L_3 = 10:5:5$ . This ratio is satisfied by a mixture of 90% M1 + 10% E2.

<sup>3</sup>Intensity from Au radiator 0.7, from coincidence measurements 0.9; internal conversion lines masked by Os<sup>191</sup> peaks; upper limit  $\alpha_K$  estimated from lower limit of gamma intensity.

<sup>4</sup>Multipole assignment based on *K*/*L* ratio.

<sup>5</sup>*L* peak falls under 646 *K* peak.

<sup>6</sup>Normalized value:  $N_{M+N} = 7.2\pm 3$ ;  $\alpha_T/\alpha_K = 1.33$ .



these types, but the data are not generally good enough to establish the mixture ratio with any confidence.

The transition probabilities were calculated from the quantum and conversion electron intensities, with the assistance of theoretical conversion coefficients where necessary, and the scale normalized to make the sum of the transition probabilities leading to the ground state total 100%.

The fluorescent yield in the  $K$ -shell for rhenium is 0.94 (Bergstrom 1955) so that  $K$ -shell vacancies are created in 69% of the disintegrations. Of these, 2.0% are due to internal conversion, the remainder being caused by  $K$ -electron capture. Thus, the number of  $K$ -electron captures per disintegration is  $67 \pm 8\%$ ; presumably the remaining  $33 \pm 8\%$  represent  $(L+M+N)$ -electron captures. If we make the reasonable assumption that the  $(M+N)$ -capture probability is 0.2 of that for  $L$ -capture, there are  $27.5 \pm 7\%$   $L$ -captures per disintegration. The  $L/K$  capture ratio resulting from these two numbers is  $0.41 \pm 0.15$ .

A typical pulse spectrum obtained by the split-crystal technique is shown in curve A of Fig. 4. The  $L/K$  capture ratio obtained from data such as are presented in curve A was  $0.38 \pm 0.05$  in good agreement with the value predicted from the  $K$ -shell X-ray intensity. The limits of error quoted are those imposed by the difficulty in subtracting the photomultiplier noise contribution underlying the  $L$ -peak. These limits are probably too small when one takes into consideration the fact that absorption of  $L$ -Auger electrons in the source

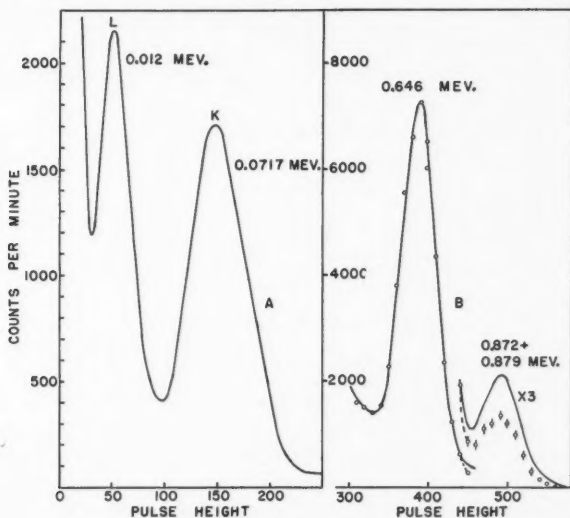


FIG. 4. Scintillation spectrometer spectrum of the gamma rays of  $\text{Os}^{185}$ .

(A) The low-energy pulse spectrum obtained with a split crystal. The ratio of  $L$ -capture to  $K$ -capture for transitions to all levels may be deduced directly from the areas of these peaks.

(B) The solid curve shows the single-channel, high-energy pulse spectrum of  $\text{Os}^{185}$ . The experimental points present the spectrum of coincidences between gamma-rays and  $K$ -shell X-rays normalized to the single-channel pulse spectrum in the region of the 0.646 Mev. peak. The presence of  $K$ -capture to levels  $F$  and  $G$  is clearly indicated.

material and the thin film of oil bonding the two halves of the crystal would make the measured  $L/K$  ratio too low. On the other hand, the pulse distribution following  $M$ -shell capture would be imperfectly resolved from the broad  $L$ -peak distribution. If these were being detected, the measured ratio would be too large. Since it seems impossible to assess the relative importance of these two effects, it becomes very difficult to place realistic limits of error on this measurement. From the agreement between the two methods of estimating the  $L/K$  ratio, it would seem reasonable to assume these effects are small and to quote a value of  $0.38 \pm 0.07$  for this ratio.

Although it is quite difficult to obtain a precise value of the  $L/K$  capture ratio for the entire decay process, the level structure of  $\text{Re}^{185}$  makes it possible to determine the  $L/K$  capture ratio for the  $0.872 + 0.879$  Mev. doublet level with much greater accuracy. It is readily shown that when a level, fed only by electron capture, is de-excited by a gamma-ray transition, the number of coincidences between gamma-rays and  $K$ -shell X-rays per recorded gamma-ray is  $P_K \epsilon_X$ , where  $P_K$  is the fraction of the transitions to the level concerned which follow  $K$ -electron capture and  $\epsilon_X$  is the over-all detection efficiency factor for the X-ray detector. A comparison of  $N_{\gamma X}/N_\gamma$  for gamma-rays de-exciting two different levels gives the ratio of the  $P_K$  values for the two levels directly, provided that the internal conversion coefficients for the gamma-rays are small. The value of  $P_K$  is quite insensitive to the energy available for the capture process, except when this energy is close to the  $K$ -shell binding energy. If the energy available is close to this limit for transitions to the upper level and is much greater than this limit for transitions to the lower level, a comparison of  $P_K$  for the two levels provides a sensitive means of measuring the  $L/K$  capture ratio for the upper level.

Curve B of Fig. 4 shows both the single-channel pulse spectrum in the gamma-ray detector and the spectrum of coincidences recorded with  $K$ -shell X-rays. It is clear from a casual inspection of the curves that  $P_K(0.646)$  is much larger than  $P_K(0.872 + 0.879)$ . The ratio  $P_K(0.646)/P_K(0.872 + 0.879)$  was found to be  $1.59 \pm 0.03$ . The measured ratio was found to be independent of source-counter geometry as long as there was no overloading of the side-channel pulse height analyzers.

From the theory of electron capture, it is known that

$$P_K = [1 + \{(g_{LI}^2 + g_{LII}^2)/g_K^2\}(W_L/W_K)^2 + (g_{MI}^2/g_K^2)(W_M/W_K)^2]^{-1}$$

where  $W_K = W_0 - E_\gamma + S_K$ ,  $S_K$  represents the total energy of an electron in the  $K$ -shell, and  $W_0$  the nuclear energy difference between the ground states of the parent and daughter nuclei.  $W_L$  and  $W_M$ , and  $S_L$  and  $S_M$ , are similarly defined. The ratio  $(g_{LI}/g_K)^2$  has been evaluated by Rose and Jackson (1949) to be 0.14 for  $Z = 75$ . The value of  $(g_{LII}/g_K)^2$  is about 0.01 (Robinson and Fink 1955). It is reasonable to assume that  $(g_{MI}/g_K)^2$  will not be more than 0.03. With this choice of constants and with  $W_0 = 0.95 m_0 c^2$ , the value of  $P_K$  for transitions to the 0.646 Mev. level is 0.79. Using this value and the experimental ratio of the last paragraph, the value of  $P_K$  for transitions to the  $0.872 + 0.879$  Mev. levels is  $0.49 \pm 0.01$ . This value takes into account a

small correction for the effect of the 0.163 and 0.233 Mev. gamma-rays. The  $L/K$  capture ratio for transitions to the doublet levels is  $1.04 \pm 0.04$ . Since this ratio is only shifted by 9% when the value of  $(g_{L1}/g_K)^2$  is shifted by 40%, it is clear that this ratio is quite insensitive to the theoretical parameters chosen.

Fig. 5 presents the results of the  $\gamma$ - $\gamma$  coincidence experiments using the equipment already described. Curve A presents the single-channel pulse spec-

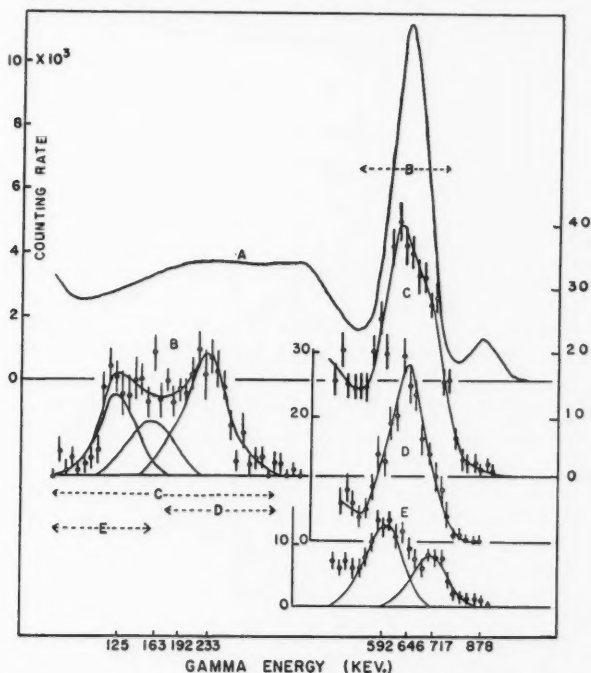


FIG. 5. Gamma-gamma coincidence spectra. Curve A. Single-channel spectrum above 75 kev. with the X-rays removed by means of a tin absorber. Curve B. Coincidences with fixed channel gated on the region shown by the horizontal line labelled B. Curves C, D, and E. Coincidences with fixed channel gated on regions marked C, D, and E, respectively.

trum in either detector for the region above 75 kev. The X-rays have been prevented from reaching either detector by means of tin absorbers. The strong peak at 0.646 Mev. completely masks the 0.592 and 0.717 Mev. photo-peaks, although their presence can be noted in the width of this distribution which always appeared slightly broader than the 0.661 Mev.  $\text{Cs}^{137}$  calibration peak.

Curve B presents the coincidence spectrum obtained by setting the fixed channel to take in all of the 0.646 Mev. peak and scanning across the region from 0.100 Mev. to 0.4 Mev. This spectrum can be reasonably resolved into

components at 0.125, 0.163, and 0.233 Mev., corresponding to gamma-rays found with the beta spectrometer. The  $\text{In}^{114}$  radiation at 0.192 Mev. was used to provide an energy calibration and peak profile for this analysis. It can be seen from an inspection of the decay scheme of Fig. 6 that the relative intensities of these three peaks, after slight corrections for absorption and counter

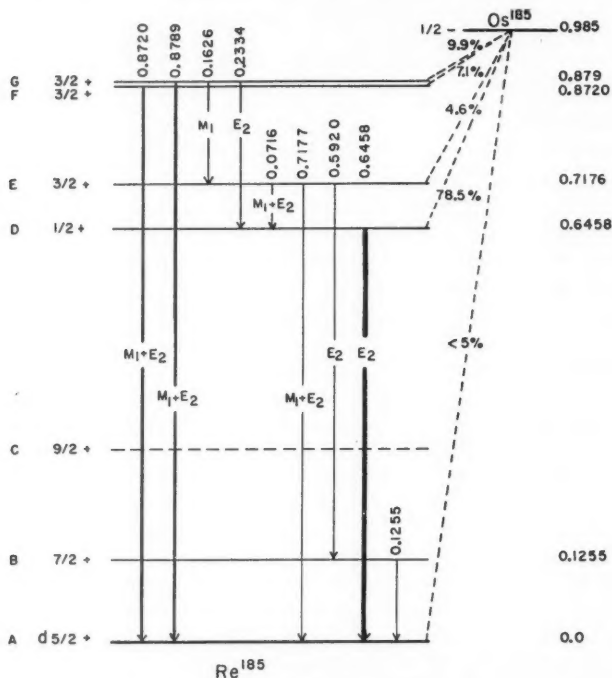


FIG. 6. Decay scheme for  $\text{Os}^{185}$ .

efficiencies, should be the same as the relative intensities of the 0.125, 0.163, and 0.233 Mev. gamma-rays. This conclusion involves the assumption that there is essentially no electron capture to the 0.125 Mev. level. The intensity estimates quoted for the 0.125 and 0.163 Mev. radiations have been based on curve B with support from curves C, D, and E of the same figure.

Curve C presents the coincidence spectrum obtained when the fixed channel was set to include the broad distribution of curve B and the movable channel scanned over the 0.6 Mev. region. It is evident that the 0.592 and 0.717 Mev. radiations play a far more important role in the coincidence spectrum than they do in the single-channel spectrum.

Curve D was obtained in the same manner as C with the fixed channel set to include only the 0.233 Mev. peak and a small fraction of the 0.163 Mev. distribution. The sharp peak obtained is typical of that for a single gamma-

ray of energy 0.646 Mev. and shows conclusively that the 0.233 Mev. gamma-ray is in coincidence with the 0.646 Mev. radiation and no other.

Curve E was obtained by setting the fixed channel to include the 0.125 and about half of the 0.163 Mev. peak. The spectrum shows coincidences with both the 0.592 and 0.717 Mev. radiations and very few with the 0.646 Mev. gamma-ray.

The data presented in curves B to E are completely accounted for if one assumes that the 0.125 Mev. radiation is in cascade with the 0.592 Mev. gamma-ray, the 0.163 Mev. radiation is in coincidence with both the 0.592 and 0.717 Mev. radiations, and the 0.233 Mev. gamma-ray is in coincidence only with the 0.646 Mev. transition.

#### DISCUSSION

The decay scheme of Fig. 6 is consistent with the energy and coincidence measurements presented above. An equally good energy fit can be obtained by reversing the order of the 0.1626–0.0716 Mev. cascade and locating a level at 0.808 Mev. This choice, which was made by Pruett and Wilkinson (1955), is ruled out conclusively by the coincidence data, which show that the 0.163 Mev. radiation is in coincidence with the 0.7177 Mev. gamma-ray.

The ground state of  $\text{Re}^{185}$  has been measured to be  $5/2$  (Mach 1950) and shell structure predicts that it is a  $d\ 5/2$  level. Shell structure theory also suggests that the ground state of  $\text{Os}^{185}$  is determined by a  $p\ 1/2$  proton so that this state should be described as  $1/2^-$ . If this prediction is correct, one would expect very little capture to the ground state of  $\text{Re}^{185}$  and it becomes a simple process to calculate the absolute transition probabilities of Table I. It is possible, from the intensities presented in the last section, to set an upper limit on the intensity of transitions to the ground state. The branching ratios of Fig. 6 have been normalized to 100 on the assumption that no transitions proceed to the ground or first excited states of  $\text{Re}^{185}$ . If we let the number of transitions to these levels be  $\delta$ , we have  $100+\delta$  disintegrations altogether. We have already seen that there are  $67\pm 8$   $K$ -shell vacancies created by  $K$ -capture. Thus, the total percentage of  $K$ -capture occurring is  $(67\pm 8)-0.67\delta$ .

The probability of  $K$ -capture can also be found independently using the split-crystal data. The total number of  $K+L+M$  vacancies created is  $(102.9+\delta)$  if we assume the number of  $M+N$  vacancies created by internal conversion to be 0.2 of the number of  $L$  vacancies. Using the measured split-crystal  $L/K$  ratio, we obtain a value of  $(71\pm 4)+0.69\delta$  for the probability of  $K$ -capture. By comparing these two results for the number of  $K$ -shell vacancies created, one can see that the best agreement is obtained for  $\delta = 0$  and that the limits of error restrict the choice of  $\delta$  to a value less than 5%. Thus we conclude that the transitions to the 0 and 0.1254 levels of  $\text{Re}^{185}$  together represent less than 5% of the disintegrations.

Since all the transitions of Table I have even parity, all the levels of  $\text{Re}^{185}$  identified in Fig. 5 must have the even parity characteristic of the ground state. Coulomb excitation experiments (McLelland *et al.* 1955; Davis *et al.* 1956) have identified rotational levels of spin  $5/2+$  and  $7/2+$  at excitation

energies of 0.130 and 0.300 Mev. Presumably, the first of these is level B; the second shown as C in Fig. 6 will not be populated in electron capture.

The strongly populated level D at 0.646 Mev. is almost certainly  $1/2+$ . This choice accounts in the simplest way for the  $E2$  nature of the strong 0.646 Mev. transition and the absence of the competing transition to level B. A search made for this transition set an upper limit on its intensity of 1% of the 0.646 Mev. radiation.

Level E is probably  $3/2+$ . This choice is the only one consistent with the observed transitions to and from this level. By similar reasoning we conclude that level G has a spin of  $3/2$ . This choice is the only one that satisfies the  $E2$  character of the 0.233 Mev. radiation, the intensity of the electron capture transition to this level, and the mixed character of the ground state transition. This choice predicts that an  $E2$  transition of energy 0.754 Mev. should occur between levels G and B. The  $K$ -shell conversion peak in uranium for such a radiation falls among the  $L$  and  $M$  peaks of the 0.646 Mev. transition and could not be detected. The absence of the internal conversion lines could be used to set an upper limit of about 0.5% on its intensity.

Level F at 0.872 Mev. is placed in the decay scheme purely on the basis of the single  $M1+E2$  transition to the ground state. This level must, therefore, also have a spin of  $3/2+$ . The absence of transitions to D and E is not surprising when one realizes that the transitions to these levels from G are just detectable.

Recent work of Pruett and Wilkinson (1955) locates levels as follows:  $0(5/2+, A)$ ,  $0.125(7/2+, B)$ ,  $0.645(1/2+, D)$ ,  $0.808(1/2+, \dots)$ , and  $0.875(3/2+, F, G)$ . Their proposed decay scheme is in good agreement with ours, except for the high-lying levels. Their failure to detect the 0.592 and 0.7177 Mev. radiations and the doublet character of the 0.875 Mev. radiation accounts for most of the differences. From the information published in their abstract, it would seem that the present decay scheme provides an extension of theirs without doing violence to any of their experimental measurements.

The total  $L/K$  capture ratio as determined in these experiments is in rough agreement with the values obtained by Miller and Wilkinson (1951), who compared the  $L$  and  $K$  X-ray intensities with a source external to the crystal. On the basis of these measurements, Robinson and Fink (1955) deduced that all transitions to the 0.875 Mev. level proceed by  $L$ -capture. The  $\gamma$ -X coincidence measurements reported here show clearly that this conclusion is incorrect.

The  $\log f_0 t$  values for transitions in electron capture cannot be calculated unless the decay energy is known. However, the atomic mass difference between  $\text{Os}^{185}$  and  $\text{Re}^{185}$  must be very close to 0.99 Mev. for reasons to be outlined in the next paragraph. For this energy release, the values of  $\log f_0 t$  for transitions to levels D, E, F and G are, respectively, 7.2, 8.1, 6.9, and 6.6. In calculating the values for levels F and G, allowance was made for  $LII$  and  $MI$  capture. For the other levels only  $K$  and  $LI$  capture offer a significant contribution. The  $\log f_0 t$  values for these four levels are characteristic

of first-forbidden transitions and support the spin assignments of Fig. 6. If one sets a 5% upper limit for transitions to the ground state of  $\text{Re}^{185}$ , a lower limit of 9.3 is placed on its  $\log f_0 t$  value. This limit is characteristic of a unique first-forbidden transition. For level *B*, a lower limit of 10 is obtained if one sets an upper limit of 1% on the transitions to this state.

These experiments provide three independent methods of estimating the energy release in the decay of  $\text{Os}^{185}$ . Curves *F* and *G* of Fig. 7 show the  $\log f_0 t$  values for transitions to levels *F* and *G* as a function of decay energy. Since both transitions are known to be first forbidden, the energy release cannot reasonably be less than 0.95 Mev.

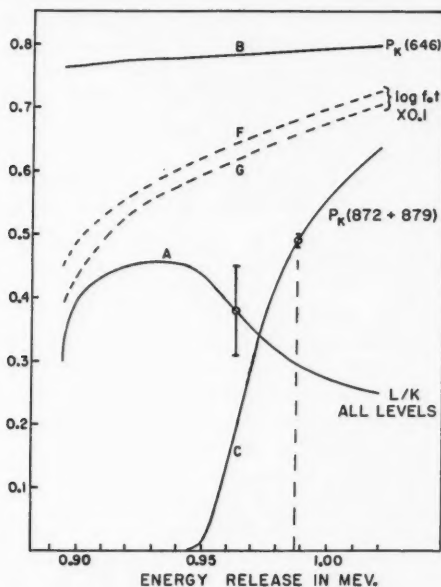


FIG. 7. Curve A. The ratio of *L*-capture to *K*-capture for transitions to all levels computed as a function of energy release; the experimental point shown represents the measured *L/K* ratio obtained with the split crystal. Curve B. The fraction of transitions to level *D* which proceed by *K*-capture calculated as a function of energy release. Curve C. The same as curve B computed for the levels *F* and *G*. The experimental point represents the result of the  $\gamma$ - $X$  coincidence measurements. Curves *F* and *G*.  $\log f_0 t$  values as a function of energy computed for levels *F* and *G*.

Curve A of Fig. 7 shows the energy dependence of the ratio of *L*-capture to *K*-capture on the energy release when all levels are considered. This curve was computed using the intensities of Table I and the decay scheme of Fig. 6 and includes the effects of *LII* and *M* capture. The shape of this curve is essentially correct but uncertainties in the measured intensities, the failure to detect some of the possible transitions from levels *F* and *G*, and errors in the theoretical parameters introduce uncertainties of the order of 0.02 in the



ordinate scale of this curve. The measured ratio is  $0.38 \pm 0.07$ . As can be seen from Fig. 7, this ratio leads to an energy release of  $0.963 \pm 0.030$  Mev.

Curves B and C of Fig. 7 show values of  $P_K$  as a function of the energy release for level *D* and levels *F* and *G* computed in the manner already described. The  $\gamma$ -X coincidence data lead to the point shown on curve C and define the energy release as  $0.987 \pm 0.004$  Mev. The limits of error quoted are those associated with the experimental measurements and do not include the effect of errors in the theoretical parameters involved in calculating curves B and C. However, the method is very insensitive to the choice of these parameters; for example, a change in  $(g_{L1}/g_K)^2$  of 40% causes a shift of only 7 kev. in the predicted energy release.

Although all three methods of estimating the energy are consistent, the third method must be taken most seriously. It is concluded that the energy release in the decay of  $\text{Os}^{185}$  is  $0.985 \pm 0.007$  Mev.

Recent studies (Bisi *et al.* 1955) of the decay of  $\text{W}^{185}$  locate a  $7/2+$  level in  $\text{Re}^{185}$  at 0.0556 Mev. above the ground state. The decay scheme of Fig. 6 suggests that such a level would be appreciably populated in the decay of  $\text{Os}^{185}$ . A search for the predicted transitions was unsuccessful. Recent work in this laboratory (Williams and Johns 1957) and elsewhere (Dubey 1957) indicates that the decay of  $\text{W}^{185}$  is simple and that no 0.0556 Mev. level exists.

#### ACKNOWLEDGMENTS

The sources for these experiments were obtained through the courtesy of the United States Atomic Energy Commission and Brookhaven National Laboratories. We are indebted to Dr. L. G. Elliott of Atomic Energy of Canada Ltd. for supplying us with Professor Sliv's excellent tables of internal conversion coefficients, and to Dr. G. T. Ewan of the same organization for constructive criticisms of the manuscript. Thanks are also due to Miss Agda Artna who assisted greatly in the analysis of the experimental data.

This work was supported by grants from the National Research Council of Canada and the Ontario Research Foundation, and through a scholarship awarded by the Imperial Oil Company of Canada to one of the authors (W.J.K.).

*Note added in proof.*—The authors would like to draw attention to a careful study of  $\text{Os}^{185}$  by Marty and Vergnes (1957) which has recently been published. The results of their energy and coincidence measurements are in excellent agreement with ours. They did not have available sufficient resolution to separate the 0.872–0.879 Mev. doublet nor did they determine the internal conversion coefficients of the weaker radiations. Although they were therefore unable to locate the 0.872 Mev. level in  $\text{Re}^{185}$ , they arrive at the same conclusions as we do concerning the location of the remaining excited states of Fig. 6. Our failure to agree on spin assignments is at least partially due to the paucity of their internal conversion data.



## REFERENCES

- BELL, P. R. 1955. Beta and gamma ray spectroscopy, *edited by* K. Siegbahn (Interscience Publishers Inc., New York), p. 161.
- BELL, R. E., GRAHAM, R. L., and PETCH, H. E. 1952. *Can. J. Phys.* **30**, 35.
- BENDEL, W. L., SHORE, F. J., BROWN, H. N., and BECKER, R. A. 1952. *Phys. Rev.* **87**, 195A.
- BERGSTROM, L. 1955. Beta and gamma ray spectroscopy, *edited by* K. Siegbahn (Interscience Publishers Inc., New York), p. 630.
- BISI, A., TERRANI, S., and ZAPPA, L. 1955. *Nuovo cimento*, **1**, 291.
- BUNKER, M., CANADA, R., and MITCHELL, A. C. G. 1950. *Phys. Rev.* **79**, 610.
- CORK, J. M., LE BLANC, J. M., NESTER, W. H., MARTIN, D. W., and BRICE, M. K. 1953. *Phys. Rev.* **90**, 444.
- DAVIS, R. H., DIVATIA, A. S., LIND, D. A., and MOFFATT, R. D. 1956. *Phys. Rev.* **103**, 1801.
- DUBEY, V. S. *et al.* 1957. *Bull. Am. Phys. Soc.* **2**, 24A.
- GOODMAN, L. J. and POOL, M. L. 1947. *Phys. Rev.* **71**, 288.
- HEATH, R. L. and BELL, P. R. 1952. *Phys. Rev.* **87**, 176A.
- JOHNS, M. W. and NABLO, S. V. 1954. *Phys. Rev.* **96**, 1599.
- KATZIN, L. I. and POBERSKIN, M. 1948. *Phys. Rev.* **74**, 264.
- MACH, J. E. 1950. *Revs. Modern Phys.* **22**, 64.
- MCLELLAND, C., MARK, H., and GOODMAN, G. 1955. *Phys. Rev.* **97**, 1191.
- MARTY, M. and VERGNES, M. 1957. *J. phys. radium*, **18**, 233.
- MEINKE, W. W. 1949. University of California Radiation Laboratory Report No. 432, p. 211.
- MILLER, M. and WILKINSON, R. G. 1951. *Phys. Rev.* **82**, 981L; **83**, 1050L.
- PRUETT, C. H. and WILKINSON, R. G. 1955. *Phys. Rev.* **100**, 1237A.
- RIETJENS, L. H., ARKENBOUT, G. J., WALTERS, G. F., and KLUYVER, J. C. 1955. *Physica*, **21**, 110.
- ROBINSON, B. L. and FINK, R. W. 1955. *Revs. Modern Phys.* **27**, 424.
- ROSE, M. E. 1955. Beta and gamma ray spectroscopy, *edited by* K. Siegbahn (Interscience Publishers, Inc., New York), Appendix IV.
- 1956. Private communication.
- ROSE, M. E. and JACKSON, J. L. 1949. *Phys. Rev.* **76**, 1540.
- SLIV, L. A. 1956. Private communication from Professor Sliv of Leningrad to Dr. L. G. Elliott of Atomic Energy of Canada Ltd., Chalk River.
- SWAN, J. B. and HILL, R. D. 1952. *Phys. Rev.* **88**, 831.
- WILLIAMS, I. R. and JOHNS, M. W. 1957. *Nuovo cimento* (In press).

# METEOR SIGNAL RATES OBSERVED IN FORWARD-SCATTER<sup>1</sup>

E. L. VOGAN AND L. L. CAMPBELL

## ABSTRACT

Diurnal and seasonal variations in meteor signal rate observed during a 15 month period over a forward-scatter path situated in eastern Canada are discussed. Measurements were made at a frequency of 49.98 Mc./s. The data show a large spread from hour to hour and day to day with the greatest signal rate being observed during the summer months. The influence of ionospheric absorption on the signal rate observed during the morning hours is considered and it is concluded that the presence of a small amount of attenuation can modify appreciably the form of the diurnal variation.

## INTRODUCTION

For many years, professional and amateur astronomers have observed and studied meteors as they streaked across the sky. Although visual observations are confined necessarily to clear, dark nights, a great quantity of data has been compiled during shower and non-shower periods. The data have been used to estimate the mass distribution and the flux density of meteoric particles incident on the earth at any time of the year as well as the total mass of meteoric matter striking the earth in the course of a day (Watson 1941).

Not until the end of World War II, when radar techniques were introduced by research teams at the University of Manchester and the National Research Council of Canada, was it possible to investigate the daytime meteor activity. The first group announced the discovery of a number of annually-recurring showers which exhibited strongest activity during the daytime hours and which were most prevalent during the months of May, June, and July. The meteor rates associated with some of these daytime showers appear to be as great as those produced by the major nighttime showers (Lovell 1954). Both groups have made extensive studies of the ionizing height, velocity, and radiant parameters of meteors (Lovell 1954; McKinley 1951, 1954; McKinley and Millman 1949).

More recently, it has been shown that meteors can be observed by forward-scatter techniques using continuous wave transmission with relatively small radiated power (Allen 1948; Forsyth and Vogan 1955). The method is important since the duration and the amplitude of a meteoric signal observed in forward-scatter may be appreciably larger than in the backscatter case. With low-power transmitters, the method lends itself readily to continuous unattended operation using moving-chart recording ammeters to record the received signal. Meteoric forward-scatter has been treated theoretically by Eshleman (1952) and Eshleman and Manning (1954), who started with Lovell's expression for backscatter and extended it for the forward-scatter case. Geometrical aspects of forward-scatter have been studied at Stanford University and the Radio Physics Laboratory, Ottawa (Eshleman and Manning

<sup>1</sup>Manuscript received March 4, 1957.

Contribution from the Radio Physics Laboratory of the Defence Research Board, Ottawa, Canada. Work carried out under Project No. PCC D48-28-35-05.

1954; Hines 1955; Hines and Pugh 1956; Pugh 1956; Villard, Eshleman, Manning, and Peterson 1955).

The University of Manchester has accumulated a considerable amount of information concerning meteor signal rates observed on backscatter (see Lovell 1954). Hawkins (1956) has surveyed the data to obtain the seasonal variation in signal rate by determining the average rate for each month of the year. No similar results have been reported for forward-scatter. Such information is of particular interest in the development of communication systems utilizing either individual meteor signals or the continuous background produced by the overlapping of many signals.

Since 1952, the Radio Physics Laboratory has been investigating meteoric effects using forward-scatter equipment operating in the frequency range 30 to 50 Mc./s. over path lengths of 800 to 1000 km. Some results of this experimental program have been reported recently in the literature (Forsyth, Hines, and Vogan 1955; Forsyth and Vogan 1955, 1956). In the present paper, the results of an analysis of continuous recordings made on a forward-scatter circuit over a period of 15 months are reported. These illustrate the variations in meteor signal rate observed on an hourly, daily, or monthly time scale. A possible explanation, based on the assumption that the radio waves suffer a small attenuation in the E region of the ionosphere while being propagated to and from a meteor trail, is presented to account for two features of the diurnal variation in meteor signal rate: the early hour (about 4 A.M.) at which the signal rate is a maximum and the apparent enhancement of the rate near noon.

#### EQUIPMENT

The unmodulated transmission on a frequency of 49.98 Mc./s. originated at Greenwood, N.S. The radiated power was 100 watts. The resulting signal was received and recorded at Ottawa, a distance of 860 km. approximately due west of Greenwood. Five-element yagi antennas, arranged to illuminate the mid-region of the part at a height of approximately 100 km., were used for transmission and reception. The transmitter was shut down for approximately 3 minutes each hour to facilitate identification of the transmission and to provide a measure of the noise background.

The Ottawa equipment consisted of a low noise preamplifier and a crystal-controlled receiver. The receiver had an I.F. bandwidth of 1.3 kc./s. and its response was linear. The I.F. output of the receiver was amplified further and was demodulated in an external detector circuit. The fluctuating signal from this detector was passed through a peak-reading d-c. amplifier before being applied to the input of an Esterline-Angus recorder operated at a chart speed of 12 inches per hour. The peak-reading amplifier maintained the maximum amplitude of an individual signal for approximately 3 seconds in order to overcome the inherent time constant of the recording meter (Forsyth and Rolfe 1955). Signal duration, of course, was not preserved. The resulting improvement in recorder response is illustrated in Fig. 1 for square wave pulses of constant amplitude and durations varying from 0.1 to 10.0 seconds. Using the peak-reading amplifier, the amplitude response of the system is maintained for signal durations as short as 0.1 second.

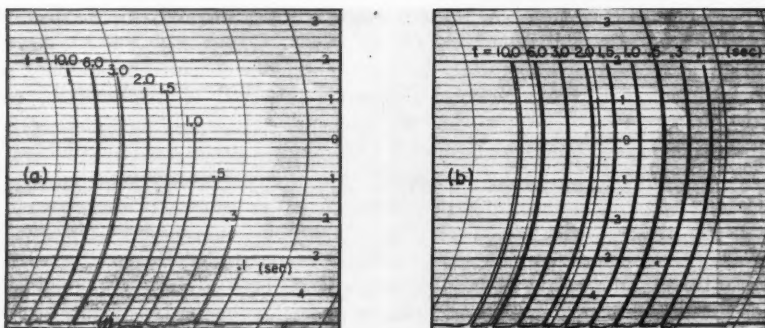


FIG. 1. Response of an Esterline-Angus recording milliammeter to square wave pulses of equal amplitudes but different durations: (a) normal response and (b) response using a peak-reading amplifier to drive the recorder.

A sample of a record of approximately 1 hour duration which contains one shut-down period is shown in Fig. 2. Records were calibrated once each working day by inserting a signal into the preamplifier and then noting the deflection on the meter. The microvolt scale shown at the right-hand side of the figure demonstrates the linearity of the recording. Each spike on the record represents a signal reflected or scattered from a meteor trail.

#### ANALYSIS

In backscatter experiments, the meteor rate is generally obtained by counting the number of signals perceptible above the noise threshold of a radar receiver. In the experimental arrangement described above, the amplitude of each individual signal is recorded. A measure of the meteor signal rate is obtained by determining the number of signals having amplitudes exceeding some arbitrarily-chosen threshold level. The level selected was that corresponding to an antenna e.m.f. of  $0.5 \mu\text{v}$ . and representing, on the average, a signal-to-noise ratio of about 20 db. Signals were counted for each hourly interval. Any section of record of questionable reliability was excluded from the analysis.

Two correction factors have been applied to the observed data. The first of these corrections compensates for the recording time lost as a result of the hourly transmitter shutdown and is a constant fraction (about 5%) of the observed signal rate. The second correction is intended to compensate for 'dead time' in the record and has the form

$$(1) \quad N_c = \frac{1}{T} \ln \left( \frac{1}{1 - N_0 T} \right),$$

in which  $N_0$  is the number of signals observed per unit time,  $N_c$  is the corrected number of signals per unit time, and  $T$  is the 'dead time' for one signal on the record caused by the finite delay of the peak-reading amplifier and the width of an ink line on the chart. Equation (1), which is derived in the appendix, is

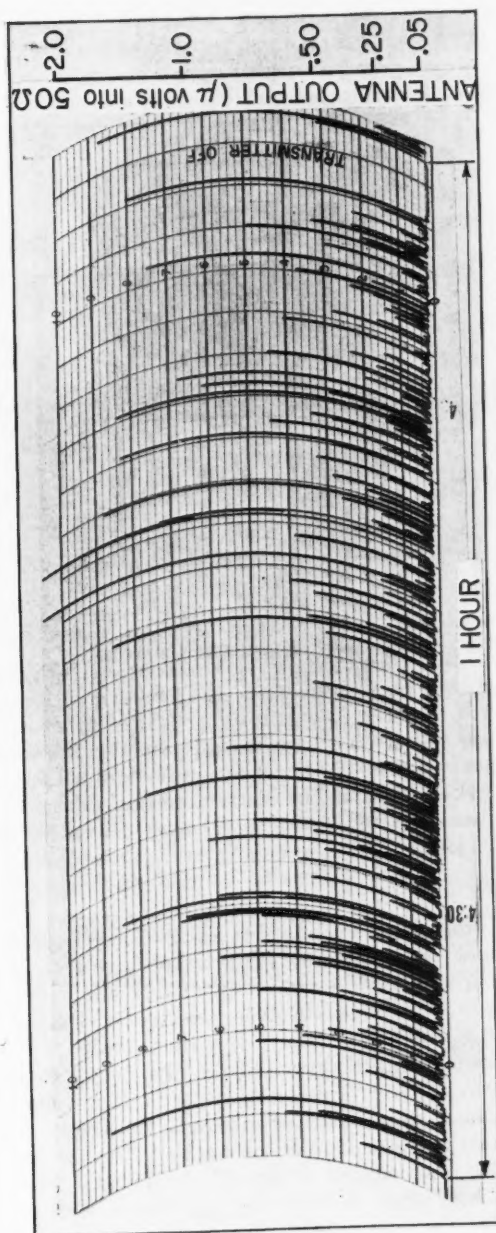


FIG. 2. Example of a typical recording of a meteor-propagated signal at 50 Mc./s.

the Geiger correction modified to account for the fact that a signal of any given amplitude may mask other signals which are of lesser amplitude. In the present paper, the data are expressed as meteor signals per hour and  $T$  is equal to  $1/450$  hour. The relationship between the observed and corrected rate is shown in Fig. 3.

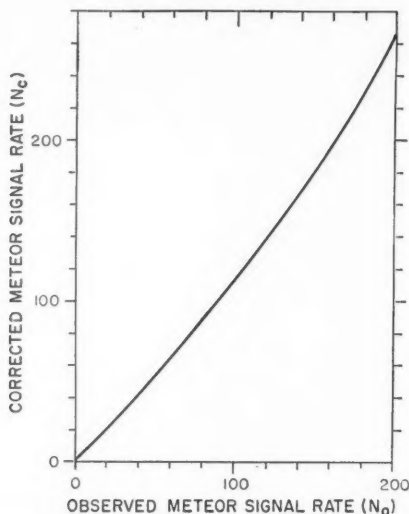


FIG. 3. Meteor signal rate, corrected for 'dead time', as a function of the observed signal rate.

In this paper, no attempt has been made to separate shower effects from the sporadic meteor background. All meteor signals recorded during the scaled periods are included in the data. The effects of certain showers on the meteor signal rate have been reported elsewhere (Forsyth, Hines, and Vogan 1955; Hines and Vogan 1957).

#### OBSERVATIONS

The recording program was continuous, except for periods of equipment failure, from the middle of June, 1955, to the end of August, 1956. The records were scaled for hourly intervals and the accumulated data have been grouped in various ways in order to present an over-all picture of the time variation of meteor signal rate as observed on a forward-scatter circuit.

Fig. 4 shows monthly scatter plots of all data for the period July, 1955, to June, 1956, inclusive. The vertical scale gives the rate in meteor signals per hour, and local time is shown on the horizontal axis. The large variation in signal rate from hour to hour and from one day to the next as well as the seasonal variation is clearly indicated. In general, the spread in the data is greater in the summer months when the rates are high than it is in the winter and spring months when the rates are low. The data for each month have been

averaged hourly and the resulting curves of average diurnal variation in meteor signal rate are superimposed on the scatter plots. The total number of signals counted for a given month is indicated in the appropriate frame. More than 210,000 signals are included in Fig. 4.

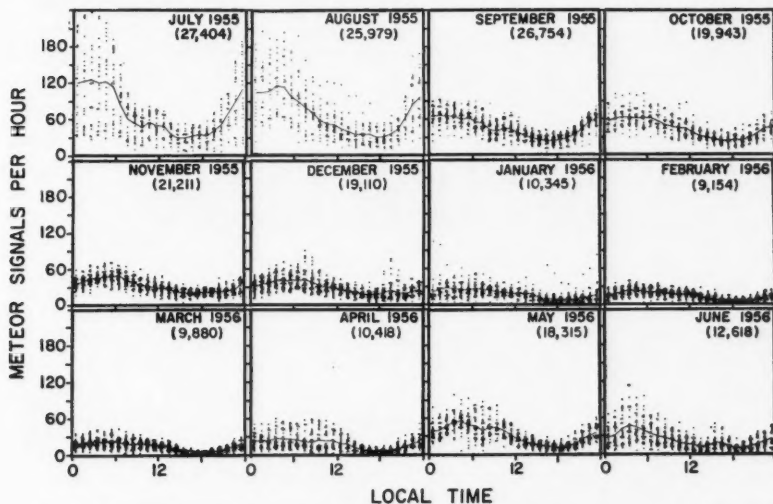


FIG. 4. Monthly scatter plots of the number of meteor signals per hour for a 12 month period commencing July, 1955. The solid curves are obtained by averaging each hour's data. The number of signals counted for each month is given in parentheses.

The data presented in the scatter diagrams of Fig. 4 have been averaged for each hour to obtain the diurnal variation curve shown in Fig. 5. This curve indicates a maximum meteor signal rate at 04 hours and a minimum rate at 18 hours. In addition, a small enhancement in the rate is suggested a little before noon. Most of the monthly curves tend to show the late morning enhancement, some more markedly than others. For certain months the early morning maximum is broad and extends back to midnight.

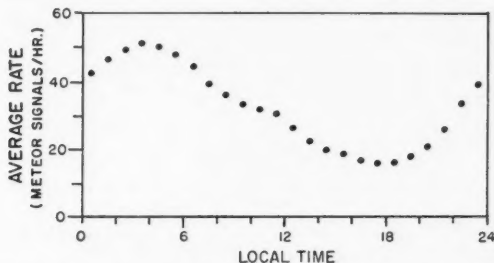


FIG. 5. Graph illustrating the average diurnal variation in meteor signal rate for the 12 month period July, 1955, to June, 1956.



The average number of meteor signals per hour for each day for which recordings were reasonably complete is shown in Fig. 6. The data covered the period commencing June 15, 1955, and terminating August 31, 1956. The increased rates caused by certain showers, in particular the Geminids (December 12) and the Quadrantids (January 3), are evident in the figure.

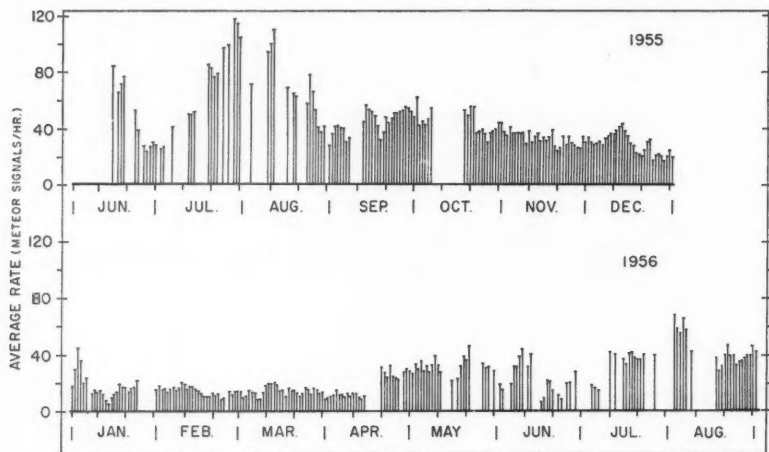


FIG. 6. Day-to-day values of meteor signal rate for the period June 15, 1955, to August 31, 1956.

All the experimental data have been averaged by monthly intervals to give the results shown in the histograms of Fig. 7. The average signal rate for each month is shown in (a). These results have been broken down further into forenoon and afternoon periods in (b), where the shaded histogram refers to the afternoon hours. The average signal rates observed during the first half of the day are roughly twice those observed during the latter half. Of some interest, particularly to communication engineers, is the degree of diurnal variation to be expected in the signal rate. A measure of this variation is  $Q_D$ , defined as the ratio of the maximum rate to the minimum rate over a 24 hour period. In practice,  $Q_D$  is found to vary over wide limits from day to day, particularly during periods of strong shower activity. The day-to-day variations have been removed by evaluating  $Q_D$  for each month from the curve of average diurnal variation in signal rate for the month. The values obtained by this means are shown in (c) and lie in the range 2.5 to 6.

#### DISCUSSION

The scatter plots of Fig. 4 illustrate the wide range of values of the meteor signal rate experienced for a specified hour on successive days. Some scatter is expected, of course, as a result of the statistical nature of the sporadic meteor background. However, the scatter is most pronounced during June, July, and



August when a considerable number of daytime and some nighttime showers are known to be active. The increased rates caused by isolated showers are apparent in the scatter plots for December and January when the Geminids and the Quadrantids are active.

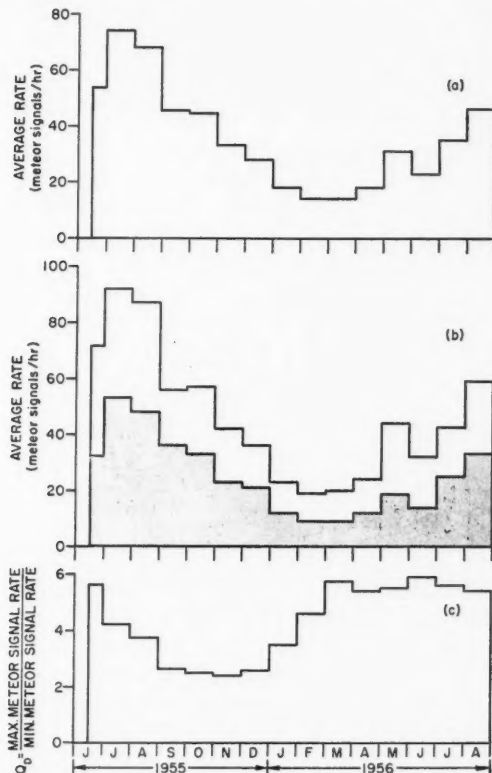


FIG. 7. Monthly values of: (a) average meteor signal rate (all data), (b) average meteor signal rate for forenoon hours (unshaded histogram) and for afternoon hours (shaded histogram), and (c) the ratio of maximum signal rate to minimum signal rate as determined from average diurnal variation curves for each month.

The seasonal variation in signal rate is illustrated by Figs. 6 and 7. In general, the signal rate is low in the spring, then builds up to a maximum during the summer months, and gradually drops off again toward the end of the year. The observed rates obtained during the latter part of the year are roughly twice those obtained in the spring. This seasonal variation is in qualitative agreement with the results obtained from backscatter data by Hawkins (1956).

There appears to be some discrepancy between the rates for July and August, 1955, and those for the same months of 1956. While every possible

precaution was taken to ensure a constant transmitter power output and accurate calibrations, the possibility of a small, gradual change in the over-all sensitivity of the equipment cannot be discounted entirely. It is known from experiment that a decrease in sensitivity of the order of 2 db. can produce a 40% decrease in the observed signal rate. A gradual reduction in sensitivity of this order would not be noticeable on the meteor records from one day to the next but would become apparent over a period of months. Although there may be some doubt concerning the accuracy of the numerical values of the signal rate, particularly during the summer months of 1956, the seasonal trend of the results is not altered.

From theoretical considerations one would expect the degree of diurnal variation in meteor signal rate ( $Q_D$ ), due to sporadic meteors alone, to vary with season. Hines (1956) presents a theoretical curve of the diurnal variation during the solstitial periods for an east-west path at a latitude of about  $45^\circ$  N. assuming a distribution of sporadic meteor radiants which is isotropic in a heliocentric system. The corresponding curves for September and March are similar to, but lie respectively above and below, the given curve. As a result,  $Q_D$  should have its largest value in March and its least value in September, with intermediate values at other times of the year. Fig. 7(c) shows such a variation from September to March, but a high value of  $Q_D$  is maintained throughout the spring and summer months, presumably as a result of the additional activity attributable to the summer daytime showers.

According to theory, the signal rate observed on an east-west path due to sporadic meteors should vary diurnally in a smooth manner and show a maximum rate at 06 hours and a minimum rate at 18 hours. The experimental results of Figs. 4 and 5 indicate that, while the signal rate does become a minimum at 18 hours, it tends to be a maximum somewhat earlier than 06 hours and, for certain months, the rate remains more or less constant between midnight and 06 hours. In addition, the rate tends to be slightly enhanced around noon. The early morning maximum has been found also by Hawkins (1956) in an analysis of the backscatter data from Manchester. Certain showers with suitable radiant positions can produce an early morning maximum in the forward-scatter data, but this maximum is apparent also during periods when little or no shower activity occurs.

There would appear to be two possible ways of interpreting these results. The meteor incidence rate may actually reach a maximum sometime before 06 hours, in which case the experimental results possibly give a reasonable description of the actual diurnal variation in the meteor incidence rate. Hawkins interprets such a variation, for certain months, on the basis of a non-isotropic distribution of sporadic meteor radiants. Alternatively, the early morning maximum and the late morning enhancement may be attributable to the experimental procedure employed to detect the meteors. Specifically, it is suggested that the appearance of the morning portion of the diurnal curve may be modified by absorption of the radio waves during their passage through the E region of the ionosphere.

## EFFECT OF ABSORPTION ON METEOR SIGNAL RATE

Very little is known about the amount of absorption normally encountered by a 50 Mc./s. radio wave during its passage through the lower ionosphere. Most workers in the field conclude that, if absorption is present, it is of negligible amount (Little, Rayton, and Roof 1956). Certainly it is so small as to be difficult to measure with any accuracy. There is evidence of the presence of very strong absorption, as much as 20 db. at 40 Mc./s., during periods of intense auroral activity, and the observed meteor signal rate is known to be reduced drastically during some such periods (Forsyth and Vogan 1957). However, only absorption by the normal ionosphere would have any pronounced influence on data obtained over a long period. For oblique transmission, the amount of absorption will be larger than that observed for vertical transmission one way through the E region by a factor equal to twice the secant of the angle of incidence of the radio waves. The absorption would be increased by a factor of 7 or 8 for an oblique path 860 km. in length.

The problem of determining the effect of absorption is complicated by the fact that the height at which a meteor trail forms is proportional to the velocity of the meteoric particle, which, in turn, varies with time of day and is greatest in the morning and least in the afternoon. The maximum height of formation (about 105 km.) occurs at 06 hours and the minimum height (about 90 km.) occurs at 18 hours. The mechanism producing absorption in the normal E region will be present during the daylight hours only and will have a maximum influence around noon. As a result of these two effects, the amount of absorption suffered by the radio wave should be a maximum sometime before noon and fall off to zero sometime in the afternoon.

The effect of absorption on the observed meteor signal rate can be determined from the expression

$$(2) \quad N = KA^{-m},$$

in which  $N$  is the number of signals having amplitudes greater than  $A$ ,  $K$  is a constant, and  $m$  is found to have a value between 1 and 4. Using the subscript 0 to indicate observed values in the presence of absorption and the subscript  $T$  to refer to true values when no absorption is present, equation (2) can be rewritten in the form of a ratio

$$(3) \quad N_T/N_0 = [A_T/A_0]^{-m}.$$

The amplitude ratio,  $A_0/A_T$ , corresponds to a decibel difference of

$$n = 20 \log[A_0/A_T] \text{ db.},$$

whence

$$(4) \quad N_T/N_0 = \text{antilog}[mn/20].$$

Equation (4) is plotted in Fig. 8 for values of  $m$  ranging from 1 to 2. Examination of the forward-scatter records suggests that  $m$  has a value of about 1.6 at the amplitude level (0.5  $\mu\text{v.}$ ) employed in this study.

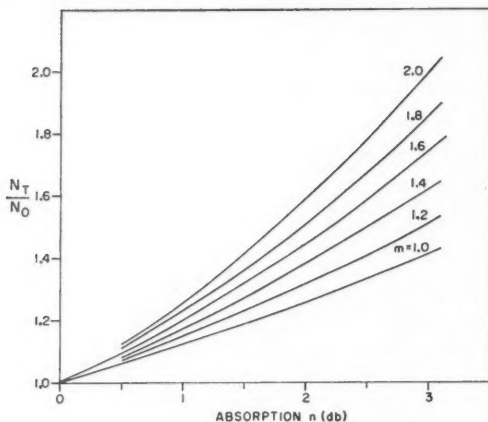


FIG. 8. Variation of the ratio of the true meteor signal rate ( $N_T$ ) to the observed rate ( $N_0$ ) with absorption for different values of the rate-amplitude exponent  $m$ .

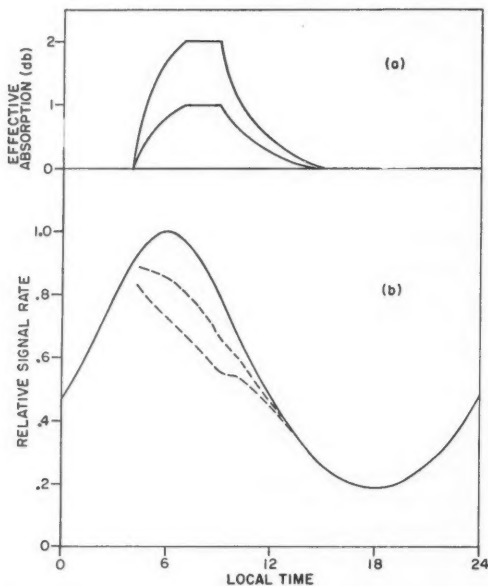


FIG. 9. Graph illustrating the possible effects of absorption on forward-scatter meteor signal rates: (a) two hypothetical absorption functions; (b) modified diurnal variation curves (broken lines) derived from the functions in (a), the curve for  $m = 1.6$  in Fig. 8, and the theoretical (solid) curve.

In order to demonstrate the possible influence of absorption on the meteor observations, absorption functions of the form shown in Fig. 9(a) are assumed. The absorption increases from zero in the early morning to a maximum value near 09 hours and then decays to zero in the early afternoon. Two curves are shown representing maximum attenuations of 1 and 2 db. The solid curve in Fig. 9(b) shows a theoretical diurnal variation. The two broken curves are obtained by applying the two absorption functions of (a) and then making the appropriate corrections to the signal rate indicated in Fig. 8 ( $m = 1.6$ ).

It is evident that an absorption function of the form assumed modifies the theoretical diurnal variation curve to a form comparable to that obtained experimentally. The morning maximum is shifted to an earlier hour. A late morning enhancement is suggested, but its size and time of occurrence is dependent upon the manner in which the absorption function decays. The amount of absorption required is not great; 2 db. on an oblique path (about 0.25 db. one way vertically through the absorbing layer) is probably of the right order.

### CONCLUSION

The meteor signal rate observed at 50 Mc./s. on a forward-scatter path was found to vary over a wide range of values during the 15 month period for which results are reported. Considerable spread was present in the data obtained for a given hourly interval on successive days and the spread was greatest during the summer months when the over-all signal rate was highest. The average signal rate varied from a minimum in the spring to a maximum during the summer, followed by a steady decrease in the latter part of the year when the rate was roughly twice that observed in the spring. Twice as many signals were observed in the forenoon as in the afternoon hours.

The diurnal variation in the observed meteor signal rate was found to differ appreciably from that expected from theoretical considerations. In particular, the observed signal rate reached a maximum value sometime before 06 hours and was enhanced, at times, near noon. A possible explanation of this anomaly is given, based upon the assumption that the radio waves suffer some absorption during their passage through the E region of the ionosphere. Although it is generally agreed that absorption at 50 Mc./s. is negligible for propagation vertically through the E region, it may not be entirely negligible when propagation is along an oblique path. A maximum attenuation of the order of 2 db. over an oblique path appears to be sufficient to explain some features of the observational results.

### ACKNOWLEDGMENT

The authors are indebted to Drs. P. A. Forsyth and C. O. Hines for many helpful discussions on various aspects of the meteor program. At one time or another, many individuals have been associated with the long-term recording program. In particular, Mr. J. W. Brown maintained the receiving equipment and made most of the recordings. Personnel at the R.C.A.F. Station, Greenwood, N.S., maintained the transmitter installation.

## APPENDIX

The actions of both the peak-reader and the pen-recorder are such that any signal which is observed will mask all smaller signals which arrive within some time,  $T/2$ , on either side of the larger signal. Thus, the number of signals which are observed must be corrected to account for the number of signals which would have been observed had they not been masked by larger signals. The correction is similar to the well-known correction which must be applied to Geiger-counter observations (see, for example, Hull and Wolfe (1954) and further references quoted there). The essential distinction between the two corrections is that in the present case an observed signal can have masked only signals with smaller amplitudes, whereas, in the case of the Geiger counter, any observed event prevents the counter from registering all subsequent events for some given time.

The derivation of the correction given here is a simplified one and is valid only when the duration of the observation period is large compared with the time between successive signals. Let  $n_0(x)dx$  and  $n_c(x)dx$  be, respectively, the observed and true number of signals per unit time with amplitudes in the range  $x$  to  $x+dx$ . It will be assumed that  $n_0(x)$  and  $n_c(x)$  are continuous functions for the range of the variable  $x$  which is under consideration. Then, the number of signals with amplitudes greater than  $A$  which are masked by one observed signal of amplitude  $x$  ( $> A$ ) is, on the average,

$$T \int_A^x n_c(u) du,$$

since an observed signal of amplitude  $x$  masks all signals of lesser amplitude for a time  $T$ . Then the true number of signals of amplitude greater than  $A$  is

$$(A.1) \quad \int_A^\infty n_c(x) dx = \int_A^\infty n_0(x) \left[ 1 + T \int_A^x n_c(u) du \right] dx.$$

If equation (A.1) is differentiated with respect to  $A$ , and then solved for  $n_c(A)$ , the result is

$$(A.2) \quad n_c(A) = n_0(A) / \left( 1 - T \int_A^\infty n_0(x) dx \right).$$

Let  $N_0$  and  $N_c$  represent the total number of observed and actual signals, respectively, per unit time, the amplitudes of which exceed some given level,  $A_c$ . That is,

$$(A.3) \quad N_0 = \int_{A_c}^\infty n_0(x) dx$$

and

$$(A.4) \quad N_c = \int_{A_c}^\infty n_c(x) dx.$$

Then, from equation (A.2),

$$(A.5) \quad N_c = \int_{A_c}^\infty \left[ n_0(A) / \left( 1 - T \int_A^\infty n_0(x) dx \right) \right] dA,$$

or, with the change of variables

$$u = 1 - T \int_A^\infty n_0(x) dx,$$

$$(A.6) \quad N_c = -T^{-1} \ln(1 - N_0 T).$$

Equation (A.6) is identical with equation (1). It will be noted that equation (A.6) is independent of the particular amplitude distribution  $n_0(x)$  which is used. At first this may appear contradictory, since one would expect that when  $n_0(x)$  is replaced by an appropriate delta function the resulting correction would be the ordinary Geiger-counter correction,

$$(A.7) \quad N_c = N_0 / (1 - N_0 T).$$

However, the derivation of equation (A.6) assumes that  $n_0(x)$  is a continuous function. The differentiation which leads to equation (A.2) could not be performed if  $n_0(x)$  were singular. In fact, if  $n_0(x)$  and  $n_c(x)$  are replaced by suitably interpreted delta functions in equation (A.1), equation (A.7) results.

#### REFERENCES

- ALLEN, E. W. 1948. *Proc. Inst. Radio Engrs.* **36**, 346.  
 ESHLEMAN, V. R. 1952. *Tech. Rept. No. 49*, Electronics Research Lab., Stanford University, Stanford, Calif.  
 ESHLEMAN, V. R. and MANNING, L. A. 1954. *Proc. Inst. Radio Engrs.* **42**, 530.  
 FORSYTH, P. A., HINES, C. O., and VOGAN, E. L. 1955. *Can. J. Phys.* **33**, 600.  
 FORSYTH, P. A. and ROLFE, W. 1955. *Radio Physics Laboratory, Defence Research Board, Ottawa, Canada, Project Report 12-1-8.*  
 FORSYTH, P. A. and VOGAN, E. L. 1955. *Can. J. Phys.* **33**, 176.  
 ——— 1956. *Can. J. Phys.* **34**, 535.  
 ——— 1957. *J. Atmospheric and Terrest. Phys.* (In press).  
 HAWKINS, G. S. 1956. *Private communication.*  
 HINES, C. O. 1955. *Can. J. Phys.* **33**, 493.  
 ——— 1956. *J. Atmospheric and Terrest. Phys.* **9**, 229.  
 HINES, C. O. and PUGH, R. E. 1956. *Can. J. Phys.* **34**, 1005.  
 HINES, C. O. and VOGAN, E. L. 1957. *Can. J. Phys.* **35**, 703.  
 HULL, T. E. and WOLFE, W. A. 1954. *Can. J. Phys.* **32**, 72.  
 LITTLE, C. G., RAYTON, W. M., and ROOF, R. B. 1956. *Proc. Inst. Radio Engrs.* **44**, 992.  
 LOVELL, A. C. B. 1954. *Meteor astronomy* (Oxford University Press, London).  
 MCKINLEY, D. W. R. 1951. *Astrophys. J.* **113**, 225.  
 ——— 1954. *Astrophys. J.* **119**, 519.  
 MCKINLEY, D. W. R. and MILLMAN, P. M. 1949. *Can. J. Research, A*, **27**, 53.  
 PUGH, R. E. 1956. *Can. J. Phys.* **34**, 997.  
 VILLARD, O. G. JR., ESHLEMAN, V. R., MANNING, L. A., and PETERSON, A. M. 1955. *Proc. Inst. Radio Engrs.* **43**, 1473.  
 WATSON, F. 1941. *Between the planets* (The Blakiston Co., New York).

## SCANDIUM ISOTOPE OF MASS 42<sup>1</sup>

J. A. R. CLOUTIER<sup>2</sup> AND A. HENRIKSON<sup>3</sup>

### ABSTRACT

A member of the odd-odd  $Z = N$  family,  $\text{Sc}^{42}$ , has been produced by proton bombardment of a calcium target greatly enriched in  $\text{Ca}^{42}$ . The positron emission, which alone is observed, has a measured half-life of 0.68 second, end point 4.8 Mev., and threshold 6.8 Mev. The superallowed transition is between ground states ( $J, T$ ) tentatively described as  $\text{Sc}^{42}(0^+, 1)$  and  $\text{Ca}^{42}(0^+, 1)$ .

### INTRODUCTION

In the course of the notable extension to the known members of the odd-odd  $Z = N$  family ( $\text{V}^{46}$ ,  $\text{Mn}^{50}$ ,  $\text{Co}^{54}$ ) made by Martin and Breckon (1952) through ( $p, n$ ) reactions, it was of course realized that  $\text{Sc}^{42}$  had been skipped. Although a smooth Dickson and Konopinski (1940) plot of log half-life against atomic number indicated for this isotope a half-life of the order of one-half of a second, Fig. 1, it seemed that the relatively low natural abundance of target material ( $\text{Ca}^{42}$ ; 0.64%) might account for the yield being below detection.

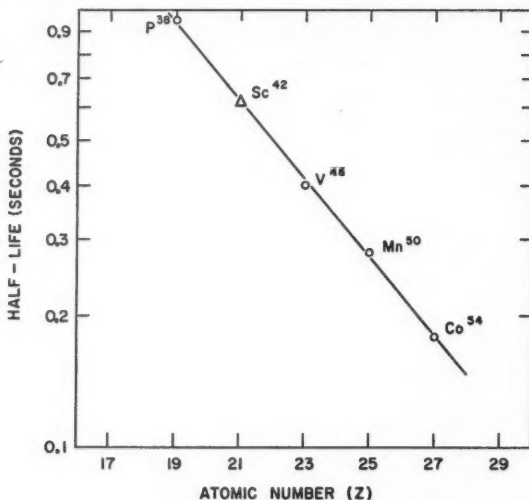


FIG. 1. Dickson and Konopinski plot; odd-odd,  $Z = N$  family.

That under comparable target conditions  $\text{Sc}^{42}$  is as readily detected as succeeding members of the family has been demonstrated in the present

<sup>1</sup>Manuscript received April 18, 1957.

Contribution from the Radiation Laboratory, McGill University, Montreal, Quebec.

The principal results of this work were presented as paper No. 28, Section III, Royal Society of Canada, June Meeting, 1955.

<sup>2</sup>Now at Department of National Health and Welfare, Ottawa.

<sup>3</sup>Now at the Defence Research Chemical Laboratory, Defence Research Board, Ottawa.



experiments with a target enriched to 28.3% in  $\text{Ca}^{42}$ . For this 40-fold increase in yield, the authors are indebted to the good offices of Oak Ridge National Laboratory and Dr. L. Yaffe of the Chemistry Department, McGill University. Following publication of our main results (Cloutier *et al.* 1955), the half-life has been confirmed by Morinaga (1955), who produced  $\text{Sc}^{42}$  by bombardment of potassium with 18 Mev. alphas.

The aim of this paper is to present the evidence for an accurate half-life, a good estimate of the positron end point, the absence of gamma rays, and a discussion of the resulting implications.

#### EXPERIMENTAL METHODS

The general arrangements at the cyclotron were similar to those used in earlier experiments (Martin and Breckon 1952; Breckon, Henrikson, Martin, and Foster 1954). With the aid of an air cylinder, the target was slowly inserted to a position selected for the proton bombardment, the cyclotron oscillator was triggered for a suitable short period of operation, and the target was immediately withdrawn rapidly to a magnetically screened position in front of a scintillation counter. The output from a counting-rate meter was displayed on an oscilloscope and half-lives were obtained from photographs. Beta and gamma energies were obtained from an analysis of pulses from calibrated stilbene and sodium iodide counters respectively. The 28-channel kicksorter designed by Bell (1954) is well suited to this work.

The target of pure calcium oxide powder was packed into a container of pure cobalt constructed by bending a sheet of cobalt 1 in. by  $\frac{1}{2}$  in. by 0.0028 in. thick in half and forming a cylinder at the fold. This cylinder was eventually closed at both ends by spot welding with cobalt electrodes. To fix the target to the aluminum carrier of the fast extractor unit, a cobalt clamp  $1\frac{1}{2}$  in. long with two cobalt guard wings was used. In bombardment position, these wings prevented protons scattered by the target from reaching the aluminum carrier and producing other short activities.

It was obvious that the beta spectrum as observed would be greatly distorted by the relatively thick source wrapped in cobalt foil and, in counting position, partially surrounded by the fast extractor unit steel walls. In order to prove that a good estimate of the end point energy may nevertheless be obtained, two known positron emitters,  $\text{Ne}^{19}$  and  $\text{P}^{30}$ , were examined under identical experimental conditions. Corrections were applied for beta energy absorption in the cobalt foil (Heitler 1947) and approximate corrections for the finite resolution of the detection system (Boley and Zaffarano 1950). The end points thus determined are plotted on the calibration curve of Fig. 2 and, as may be seen, they lie on a straight line passing through the normal zero of the kicksorter. As a further check on the reliability of the method, the  $\text{Cs}^{137}$  internal  $K$ -conversion line was also measured and is plotted on the same graph. It was thus concluded, after a number of similar trials, that this method could safely be used to determine the energy of the highest energy beta component with an accuracy of the order of 15%. For beta end point energy determination, the 28-channel kicksorter was used in conjunction with the fast extractor unit

and the thick stilbene crystal beta counter. The counter resolution was found to be 24% at 625 kev., which gives 8.6% at the observed 4.8 Mev. end point, assuming the  $E^{-1/2}$  law (Hopkins 1951) to be valid for positrons in stilbene.

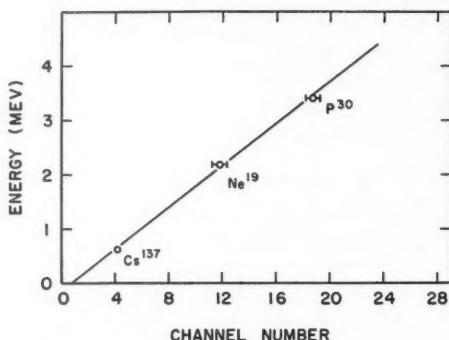


FIG. 2. Calibration curve for the beta scintillation spectrometer.

Known  $Q$  values and the mass formula indicate that no unwanted short activities will be produced in the calcium target provided the energy of bombardment is kept below 15 Mev.

#### EXPERIMENTAL DETAILS AND RESULTS

The wrapped target of pure calcium oxide, enriched to 28.3% in  $\text{Ca}^{42}$ , was bombarded for 0.3 second at a nominal proton energy of 13.1 Mev. A strong activity of short period was observed. Several other runs under selected experimental conditions were made and 38 decay curves were analyzed. They gave, for the observed half-life, a weighted average of  $0.68 \pm 0.01$  second, the surprisingly small error being the standard deviation from the mean.

Table I summarizes the experimental data for a few typical runs. In this table, the word initial at the head of the fifth column does not refer to the extrapolated initial counting rate value but rather to the first dot registered

TABLE I  
Ca<sup>42</sup>-ENRICHED CALCIUM TARGET DATA

Run No.	Detector	Bombardment energy, Mev.	Bombardment time, sec.	Initial counting rate, counts/sec.	Background counting rate, counts/sec.	Half-life, sec.
Ca-3r-1	Beta	15.1	0.3	72600	2600	0.690
Ca-3r-5	Beta	14.1	0.3	50300	3100	0.683
Ca-3r-10	Beta	13.1	0.3	28800	2700	0.665
Ca-3r-12	Beta	12.1	0.3	14800	2700	0.680
Ca-3r-15	Beta	11.1	0.3	7350	2430	0.667
Ca-3r-18	Beta	10.2	0.3	3940	2210	0.675
Ca-3r-18	Gamma	15.1	0.3	49500	3200	0.700
Ca-2r-12	Gamma	13.1	0.3	3400	620	0.675
Ca-2r-35	Gamma	13.1	0.3	13000	3000	0.676

on the decay curve photographs. The initial counting rates reported above are thus the counting rates at about two-fifths of a second after the end of the bombardment. The first six cases reported in Table I are related. They form part of a sequence of runs to determine the threshold energy of the reaction, using the beta counter and keeping all factors constant, except proton energy. They show that the measured half-life and the background counting rate were effectively constant over the necessarily restricted range of bombardment energies. The next two runs were made using the gamma counter with different bias settings on the discriminator unit. In the last run, a 10 Mev. beta absorber was placed in front of the gamma counter; hence essentially gamma rays were counted. Table I thus shows that the detected beta and gamma rays had the same decay period.

An example of the observed  $\beta^+$  decay, together with the corresponding corrected semilogarithmic plot, is shown in Fig. 3. After corrections for lost counts and background, the single half-life which remains is the same whether beta or gamma counting technique is employed within the limited range of bombardment energies.

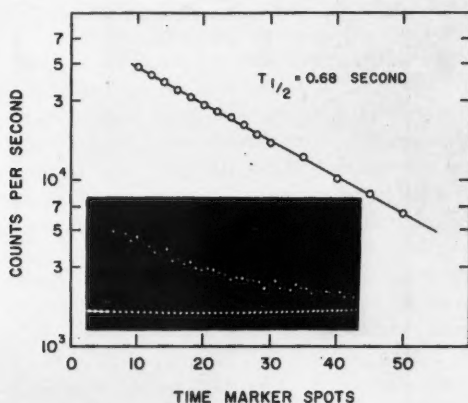


FIG. 3. Decay of Ca-39. Bombardment energy: 14 Mev.; bombardment time: 0.3 sec; 20.19 spots/sec.; beta counter.

The sodium iodide counter and kicksorter revealed only the annihilation radiation with the above half-life. The evidence indicates only positron transitions, probably between ground states.

The end point energy of the detected positrons was next measured. Five different runs were made, and each time the scintillation spectrometer was thoroughly calibrated. The data as plotted in Fig. 4 indicate that the Fermi plot would not be linear. This non-linearity at the lower energy is mainly due to the experimental conditions already described. The observations gave a weighted average of  $4.8 \pm 0.9$  Mev. for the positron end point energy.

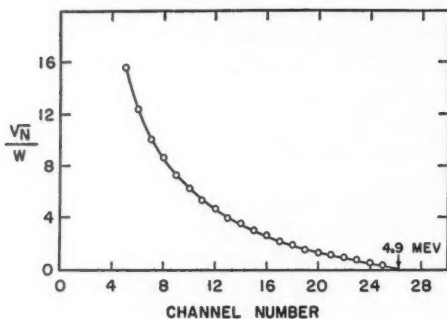
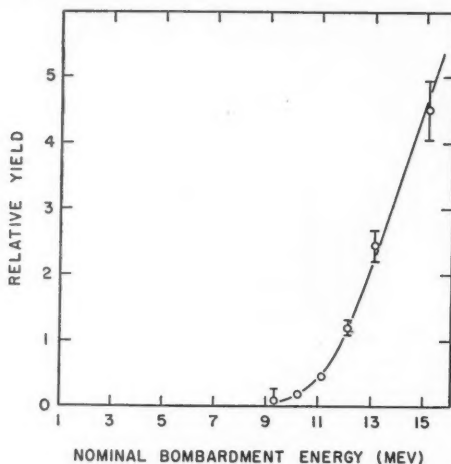


FIG. 4. Positron spectrum: approximate Fermi analysis.

The reaction threshold energy of this activity was then determined and Fig. 5 gives the observed excitation curve. The experimental points represent the instantaneous counting rates at a fixed time (dot No. 10) after the end of the bombardment at selected energies. The counting rates were taken from the

FIG. 5. Excitation curve of the 0.68 second activity from  $\text{Ca}^{42}$ -enriched calcium.

semilogarithmic plots of the decay and have been corrected for counting losses and background. As seen in Fig. 5, the reaction threshold energy is  $9.0 \pm 0.7$  Mev., which, when corrected for the incident proton energy absorbed in the cobalt envelope, becomes  $6.8 \pm 0.7$  Mev.

#### DISCUSSION OF THE RESULTS

To summarize the experimental results, a  $0.68 \pm 0.01$  second activity has been observed from bombardment of a  $\text{Ca}^{42}$ -enriched calcium sample with

protons of nominal energies ranging from 9 Mev. to 15 Mev. This activity was shown to be associated with positrons of  $4.8 \pm 0.9$  Mev. end point energy. The gamma spectrum revealed no  $\gamma$  rays other than the annihilation radiation. The threshold energy of the reaction involved was observed to be  $6.8 \pm 0.7$  Mev.

It is now possible to assign this activity to  $\text{Sc}^{42}$ . In Table II, all possible  $(p, xn)$  and  $(p, pxn)$  reactions at moderate energies starting from  $\text{Ca}^{40}$  and

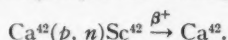
TABLE II  
ISOTOPE DATA (KING 1954; METROPOLIS AND REITWIESNER 1950)

Reactions	Resulting half-life, sec.	Particle	Energy, Mev.	Gamma energy, Mev.	Threshold, calculated, Mev.	Threshold, experimental, Mev.
$\text{Ca}^{42}(p, n)\text{Sc}^{42}$	?	—	—	—	9.6	—
$\text{Ca}^{42}(p, pn)\text{Ca}^{41}$	$10^{14}$	—	—	$K_z$	12.7	—
$\text{Ca}^{40}(p, n)\text{Sc}^{40}$	0.22	$\beta^+$	9.0	3.75	13.7	$15.5 \pm 1.0$
$\text{Ca}^{40}(p, pn)\text{Ca}^{39}$	0.9	$\beta^+$	6.10	—	14.7	$15.9 \pm 0.4$
$\text{Ca}^{42}(p, 2n)\text{Sc}^{41}$	0.87	$\beta^+$	4.94	—	20.2	—
$\text{Ca}^{42}(p, p2n)\text{Ca}^{40}$	Stable	—	—	—	22.2	—
$\text{Ca}^{40}(p, 2n)\text{Sc}^{39}$	?	—	—	—	26.2	—

$\text{Ca}^{42}$  have been listed in order of calculated threshold energy values up to 26.2 Mev. Below 15.5 Mev. bombardment energy, it is seen that no reaction starting from  $\text{Ca}^{40}$  can take place, but that two reactions starting from  $\text{Ca}^{42}$  are energetically permitted: a  $(p, pn)$  ending on  $\text{Ca}^{41}$ , which is a long-lived isotope, and a  $(p, n)$  reaction ending on  $\text{Sc}^{42}$ . Above 15.5 Mev. proton bombardment, however, it is possible to produce short-lived activities from  $\text{Ca}^{40}$  and  $\text{Ca}^{42}$ .

These expectations were realized when the normal and  $\text{Ca}^{42}$ -enriched calcium samples were bombarded at the same selected series of proton energies, same bombardment time, and identical amplification and discriminator bias settings. A photographic record of the results is reproduced in Fig. 6. It may be seen that below 15.1 Mev., a strong short activity yield is obtained only when the  $\text{Ca}^{42}$ -enriched sample is used. At 25.0 Mev., however, two additional components of 0.9 second and 0.2 second, presumably due to  $\text{Sc}^{41}$  and  $\text{Sc}^{40}$  respectively, appear in both targets. This is the expected result according to Table II. Considering now the two possible reactions on  $\text{Ca}^{42}$  at the lower energies, it is clear that  $\text{Ca}^{42}(p, pn)\text{Ca}^{41}$  may be ruled out of the present observations since  $\text{Ca}^{41}$  emits no positrons (Richards, Smith, and Browne 1950; Brown, Hanna, and Yaffe 1953). Thus only the reaction  $\text{Ca}^{42}(p, n)\text{Sc}^{42}$  remains and  $\text{Sc}^{42}$  is therefore the nucleus with the properties revealed in these experiments.

We have then the following sequence, forming a closed cycle:



Using the experimental threshold energy value  $E_0$  for the  $(p, n)$  reaction, and the experimental maximum energy of the emitted positrons, energy conservation in this cycle is now checked:

$$\text{Sc}^{42} = \text{Ca}^{42} + p - n + E_0 = \text{Ca}^{42} + E_\beta + 1.02 \text{ Mev.}$$

$$E_\beta = E_0 - (n - p) - 1.02 \text{ Mev.}$$

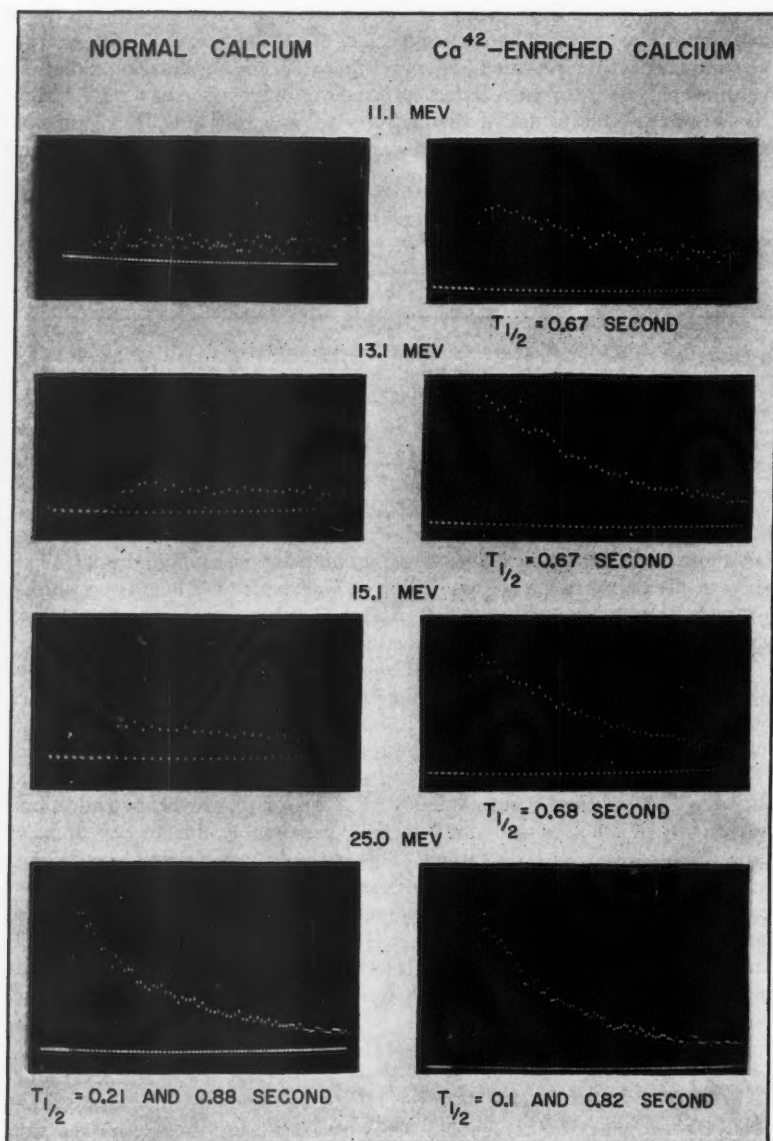


FIG. 6. Comparative study of normal  $\text{Ca}^{42}$ -enriched calcium at different bombardment energies. Amplification and discriminator bias settings are kept constant. Bombardment time: 0.3 sec.; detector: beta counter; 20 spots/sec.

Putting in values:

$$\begin{aligned} 4.8 \pm 0.9 \text{ Mev.} &= (6.8 \pm 0.7) - 1.29 - 1.02 \text{ Mev.} \\ &= 4.5 \pm 0.7 \text{ Mev.} \end{aligned}$$

The closing of the cycle to within  $(0.3 \pm 0.9)$  Mev. is strong support for the assignment of this activity to  $\text{Sc}^{42}$ .

In the light of our experimental evidence, the possibility that the positrons may be emitted by states other than the ground state of  $\text{Sc}^{42}$  cannot be eliminated and therefore it has to be assumed that they arise from transitions between ground states,  $\text{Sc}^{42} \rightarrow \text{Ca}^{42}$ . No appreciable competition from electron capture is expected, the calculated  $K/\beta^+$  branching ratio being  $1.8 \times 10^{-3}$  for  $Z = 20$  (Rose 1955) and an energy difference of 4.8 Mev.

Using the observed half-life and end point energy, the  $\log ft$  value for this  $\beta^+$  transition is found to be  $3.0 \pm 0.4$  (Rose 1955) and this places the transition in the superallowed group. This result is not surprising since  $\text{Sc}^{42}$  and  $\text{Ca}^{42}$  form an isobaric pair in which  $N = Z$  for  $\text{Sc}^{42}$  and  $N - Z = 2$  for  $\text{Ca}^{42}$ . The beta transition between them therefore may be expected to be superallowed. However, as remarked earlier, experimental conditions unfortunately prevented the observation of the true spectral distribution and the formal Fermi plot does in fact show marked departure from the straight line characteristic of superallowed transitions.

From published data on other members of the odd-odd,  $Z = N$  family (Moszkowski and Peaslee 1954; Sherr *et al.* 1955; Green and Richardson 1956), a  $\log ft$  value of  $3.0 \pm 0.4$  would correspond to a transition from a  $T = 1$  state, which, according to the Moszkowski-Peaslee rule (1954), has an even  $J$  value. Since  $\text{Ca}^{42}$  has a ground state with  $J = 0^+$  and  $T = 1$  and this  $\beta^+$  transition is a superallowed one, the even  $J$  value of the  $\text{Sc}^{42}$  ground state is  $0^+$ . The decay scheme of Fig. 7 is therefore proposed.

Morinaga (1955), using similar arguments, came to the same conclusions.

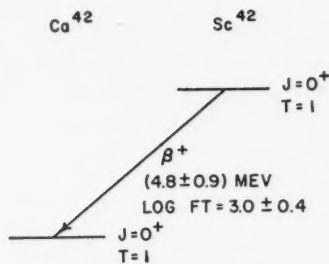


FIG. 7. Tentative decay scheme.

#### ACKNOWLEDGMENTS

One of the authors (J.A.R.C.) acknowledges a three-year fellowship from the National Cancer Institute of Canada. The authors wish to thank Dr. L. Yaffe for reminding them of the possibility of observing  $\text{Sc}^{42}$  and for making

available the  $\text{Ca}^{42}$ -enriched material. The authors wish also to thank Dr. J. S. Foster, Director of the Radiation Laboratory, for his interest and encouragement during the course of the investigation and Drs. R. E. Bell and J. D. Jackson for helpful discussions.

## REFERENCES

- BELL, R. E. 1954. Unpublished.  
BOLEY, F. I. and ZAFFARANO, D. J. 1950. Atomic Energy Commission Document A.E.C.-I.S.C. 154.  
BRECKON, S. W., HENRIKSON, A., MARTIN, W. M., and FOSTER, J. S. 1954. *Can. J. Phys.* **32**, 223.  
BROWN, F., HANNA, G. C., and YAFFE, L. 1953. *Proc. Roy. Soc. (London)*, A, **220**, 203.  
CLOUTIER, J. A. R., HENRIKSON, A., YAFFE, L., and FOSTER, J. S. 1955. Royal Society of Canada, June Meeting, Section III, paper No. 28.  
DICKSON, G. R. and KONOPINSKI, E. J. 1940. *Phys. Rev.* **58**, 949.  
GREEN, D. and RICHARDSON, J. R. 1956. *Phys. Rev.* **101**, 776.  
HEITLER, W. 1947. *The quantum theory of radiation*, 2nd ed. (Oxford University Press, London), p. 218.  
HOPKINS, J. L. 1951. *Revs. Sci. Instr.* **22**, 29.  
KING, R. W. 1954. *Revs. Mod. Phys.* **26**, 327.  
MARTIN, W. M. and BRECKON, S. W. 1952. *Can. J. Phys.* **30**, 643.  
METROPOLIS, N. and REITWIESNER, G. G. 1950. *Table of atomic masses*, Los Alamos N.P. 1980.  
MORINAGA, H. 1955. *Phys. Rev.* **100**, 431.  
MOSZKOWSKI, S. A. and PEASLEE, D. C. 1954. *Phys. Rev.* **93**, 455.  
RICHARDS, H. T., SMITH, R. V., and BROWNE, C. P. 1950. *Phys. Rev.* **80**, 524.  
ROSE, M. E. 1955. *Beta and gamma spectroscopy*, 1st ed. (North-Holland Publishing Co., Amsterdam), pp. 285-291.  
SHERR, R., KAVANAGH, R. W., and MILLS, W. R. 1955. *Phys. Rev.* **98**, 1185A.



# TIME REVERSAL EFFECTS IN MUON DECAY<sup>1</sup>

ROBERT T. SHARP AND GLEN BACH

## ABSTRACT

Expressions are given for the distribution of electrons emitted in the decay of aligned muons as a function of their energy, direction, and spin. The two-component neutrino theory of Yang and Lee is used, and two cases are considered: (i) neutrino and antineutrino emitted; (ii) two neutrinos emitted. Various correlation terms arise as a result of the inclusion of electron spin. Among these is a time reversal dependent term whose presence would be evinced by asymmetry in a transverse polarization of electrons emitted at right angles to the muon spin.

## 1. INTRODUCTION

Since the recent demonstrations that parity is not conserved in weak interactions (Wu, Ambler, Hayward, Hoppes, and Hudson 1957, and Garwin, Lederman, and Weinrich 1957) it has become of interest to determine whether or not these interactions also violate time reversal invariance. Time reversal effects have been considered in beta decay of nuclei by Jackson, Treiman, and Wyld (1957). The decay of the muon provides another such test. Dependence of the distribution function on the sign of the triple scalar product formed from muon spin, electron spin, and electron momentum would indicate non-invariance.

Our calculations are based on the two processes proposed by Lee and Yang (1957). The interaction Hamiltonians are given explicitly by Friedman (1957). They are

$$(1) \quad H'_{\text{int}} = (\bar{\psi}_\nu \gamma_4 \psi_\nu)(\bar{\psi}_e \gamma_4 (C_V + C_A \gamma_5) \psi_\mu) + \text{C.C.}$$

and

$$(2) \quad H''_{\text{int}} = (\bar{\psi}_\nu C \bar{\psi}_\nu^T)(\bar{\psi}_e (C_S + C_P \gamma_5) \psi_\mu) + \text{C.C.}$$

The  $\psi_\nu$  in the above are Yang-Lee two-component neutrino fields satisfying  $\gamma_5 \psi_\nu = -\psi_\nu$ . The Dirac operator  $C$  is chosen so that  $\gamma_\mu C = -C \gamma_\mu^T$ ; it is  $\alpha_2$  in the usual representation. Equation (1) describes muon decay with emission of a Yang-Lee neutrino and antineutrino; equation (2) corresponds to emission of two Yang-Lee neutrinos. The couplings included in (1) and (2) are the only ones which survive with Yang-Lee neutrino fields. Lee and Yang (1957) proposed that (1) only be considered since it gives a better fit to the experimental energy spectrum of the electron than (2). Friedman (1957) finds that a mixture of (1) and (2) gives the best fit to the spectrum and also to the angular correlation between electron momentum and muon spin at low electron energy. Since there are no interference terms between (1) and (2) they can be considered separately.

## 2. CALCULATION OF THE DISTRIBUTION FUNCTION

For the distribution function we find

$$(3) \quad \omega(\mathbf{n}_e, \mathbf{n}_\mu; E_e, \Omega_e) dE_e d\Omega_e = 2^{-8} \pi^{-4} \mu^3 p_e dE_e d\Omega_e \eta [1 \pm a \mathbf{n}_\mu \cdot \mathbf{k} \pm b \mathbf{n}_e \cdot \mathbf{k} + c \mathbf{n}_\mu \cdot \mathbf{n}_e + f(\mathbf{n}_\mu \cdot \mathbf{k})(\mathbf{n}_e \cdot \mathbf{k}) + g(\mathbf{n}_\mu \cdot \mathbf{n}_e \times \mathbf{k})].$$

<sup>1</sup>Manuscript received June 13, 1957.

Contribution from the Department of Mathematics, McGill University, Montreal, Quebec.

It is the probability per unit time that a muon at rest with spin in the direction of the unit vector  $\mathbf{n}_\mu$  will emit an electron with energy in  $dE_e$  in the solid angle  $d\Omega_e$  with spin, measured in its own rest frame, in the direction  $\mathbf{n}_e$ ; the coefficients  $\eta$ ,  $a$ ,  $b$ ,  $c$ ,  $f$ , and  $g$ , which are dependent on the coupling constants and the electron energy, are given in the appendix for the interactions (1) and (2);  $\mathbf{k}$  is a unit vector in the direction  $\Omega_e$ ; the electron momentum is  $\mathbf{p}_e$ ; the muon rest mass is  $\mu$ ; the upper sign refers to  $\mu^+$  decay, the lower sign to  $\mu^-$ . We use natural units ( $\hbar = c = 1$ ).

The calculation of the distribution function (3) is largely an exercise in working out spurs. Two points, perhaps, deserve amplification here. One is the method of integrating over directions of emission of the neutrino; the other is the assumed measurement of the spin of the electron in its own rest frame.

The integration over neutrino momenta is greatly facilitated if the momentum magnitudes are independent of their directions; this is the case if one works in a coordinate system in which the muon and electron momenta are equal, so that the neutrinos are emitted with equal and opposite momenta. This frame, the "calculation frame", moves relatively to the laboratory frame (in which the muon is at rest) with velocity  $-\mathbf{v}$ , where

$$(4) \quad \mathbf{v} = \mathbf{p}_e/(\mu - E_e).$$

In transforming back to the laboratory frame the distribution function must be multiplied by a factor  $(\mu - E_e)/y$  to allow for time dilatation in the transition rate. Here  $y = (\mu^2 + m^2 - 2\mu E_e)^{1/2}$ . This device so simplifies the calculation that there is no need to set  $m = 0$ , as is usually done.

It is well known that for a moving electron with definite momentum, the transverse components of spin do not commute with the sign of the energy. This is why the spin of the electron is measured in its own rest frame. In the matrix element squared the spinor  $\Gamma_e$  for the electron is replaced by  $(m/E_e')^{1/2} \exp(\frac{1}{2}\alpha \cdot \mathbf{k} \xi_e) \Gamma_e^R$ ; here  $\xi_e = \tanh^{-1}(p_e'/E_e')$ ; the momentum and energy of the electron in the calculation frame are  $p_e'$  and  $E_e'$ . Then  $\Gamma_e^R$  is the normalized spinor for the electron in its own rest frame. Projection operators  $\frac{1}{2}(1 + \sigma \cdot \mathbf{n}_e)$  and  $\frac{1}{2}(1 + \beta)$  can then be applied to  $\Gamma_e^R$  to pick out the correct spin state and energy sign. The muon spin must be treated in the same way. Jackson, Treiman, and Wyld (1957) must have done something similar to this, for they show their distribution function for beta decay as depending on the "rest spin" of the electron.

Since the electron is extremely relativistic over most of the spectrum, we get a useful approximation by setting  $m = 0$ . Equation (3) then simplifies to

$$(5) \quad \omega(\mathbf{n}_e, \mathbf{n}_\mu; x, \Omega_e) dx d\Omega_e = 3^{-1/2} \pi^{-4} \mu^5 x^2 dx d\Omega_e [A'(3-2x) \\ \mp B'(1-2x)\mathbf{n}_\mu \cdot \mathbf{k} \pm B'(3-2x)\mathbf{n}_e \cdot \mathbf{k} + D'\mathbf{n}_\mu \cdot \mathbf{n}_e \\ - \{A'(1-2x) + D'\}(\mathbf{n}_\mu \cdot \mathbf{k})(\mathbf{n}_e \cdot \mathbf{k}) + F'\mathbf{n}_\mu \cdot \mathbf{n}_e \times \mathbf{k}]$$

for the case of interaction (1), and for interaction (2) we have

$$(6) \quad \omega(\mathbf{n}_e, \mathbf{n}_\mu; x, \Omega_e) dx d\Omega_e = 2^{-11} \pi^{-4} \mu^5 x^2 (1-x) dx d\Omega_e [A'' \mp B''(\mathbf{n}_\mu \cdot \mathbf{k} + \mathbf{n}_e \cdot \mathbf{k}) \\ + D''\mathbf{n}_e \cdot \mathbf{n}_\mu + (A'' - D'')(\mathbf{n}_e \cdot \mathbf{k})(\mathbf{n}_\mu \cdot \mathbf{k}) - F''(\mathbf{n}_\mu \cdot \mathbf{n}_e \times \mathbf{k})].$$

Here

$$(7) \quad x = p_e/(p_e)_{\max} = 2p_e/\mu.$$

Our results can be compared with those of Lee and Yang (1957) and Bouchiat and Michel (1957). These authors have summed over electron spins and the former (Lee and Yang) have neglected the electron mass. The results all agree when  $m = 0$  but we find that equation (1) of Bouchiat and Michel contains an error in the angular distribution when  $m \neq 0$ .

### 3. DISCUSSION

The time reversal effect, if present, should be capable of detection experimentally. Transverse polarization of electrons emitted at right angles to the muon spin can be detected by scattering with a thin foil of high- $Z$  material (Frauenfelder *et al.* 1957). If one accepts the original suggestion of Yang and Lee that only the interaction (1) is present, the parity measurements on muon decay give evidence that the time reversal term is small. Its coefficient  $g$  is proportional to  $2 \operatorname{Im} C_A C_V^* (|C_A|^2 + |C_V|^2)^{-1}$ . If one sums (6) over electron spins and integrates over energies, the angular distribution of the electrons relative to muon spin is given by  $1 - \frac{1}{3} p \cos \theta$  where  $p = 2 \operatorname{Re} C_A C_V^* (|C_A|^2 + |C_V|^2)^{-1}$ . The experiments of Garwin *et al.* (1957) show that  $p = 1$  within 10%, indicating that  $C_A = \pm C_V$  in magnitude and phase. This implies that  $g = 0$ . Because of the large experimental error, however,  $2 \operatorname{Im} C_A C_V^* (|C_A|^2 + |C_V|^2)^{-1}$  could be as large as 0.4, not at all insignificant. For interaction (2), also, a large reflection effect implies a small time reversal effect.

There can be a strong longitudinal polarization of the electrons even with unoriented muons. Apart from the terms of order  $m/E_e$  this is independent of energy and is equal to  $2 \operatorname{Re} C_A C_V^* (|C_A|^2 + |C_V|^2)^{-1}$  and  $2 \operatorname{Re} C_S C_P^* (|C_S|^2 + |C_P|^2)^{-1}$  respectively for interactions (1) and (2). If there is no time reversal effect, this polarization could be nearly complete.

There is a process which should be considered as a possible alternative to (2) considered in this paper. It involves the emission of a Yang-Lee neutrino and an anti-Yang-Lee antineutrino instead of two Yang-Lee neutrinos. Here an anti-Yang-Lee neutrino means one for which  $\gamma_5 \psi_\nu = \psi_\nu$ . As long as the scalar and pseudoscalar couplings only are considered, the distribution functions for these two processes are identical. However for the interaction suggested here the tensor interaction must also be included. It vanishes for process (2) only because it leads to a final state wave function symmetrical in interchange of the two neutrinos, in violation of the Pauli principle. This alternative interaction would have the advantage of conserving light particles. It necessitates the use of two kinds of neutrinos, but perhaps this is not objectionable. In beta decay of nuclei there are indications that Yang-Lee neutrinos are involved in the tensor interaction, anti-Yang-Lee neutrinos in the scalar interaction (Preston 1957).

### ACKNOWLEDGMENTS

We wish to thank the National Research Council for financial support. One of us (R.T.S.) is the recipient of a Summer Associateship and the other (G.B.) holds a Studentship.

## APPENDIX

For interaction (1) we find

$$\eta = \frac{2}{\mu^3} \{A'[(\mu E_e - m^2)(\mu - E_e) - \frac{1}{3}\mu p_e^2] - D'my^2\}$$

$$a\eta = \frac{2B'p_e}{3\mu^3} (-\mu^2 + 4\mu E_e - 3m^2)$$

$$b\eta = \frac{2B'p_e}{3\mu^3} (3\mu^2 - 4\mu E_e + m^2)$$

$$c\eta = \frac{2}{3\mu^3} \{D'(\mu^2 E_e + E_e m^2 - 2\mu m^2) - A'my^2\}$$

$$f\eta = -\frac{2}{\mu^3} \left\{ \frac{1}{3}D'(\mu^2 E_e - 2\mu m^2 + E_e m^2 - my^2) - A'[\mu p_e^2 - \frac{1}{3}(\mu E_e - m^2)(\mu - E_e) + my^2] \right\}$$

$$g\eta = \frac{2F'p_e}{3\mu} \left( 1 - \frac{m^2}{\mu^2} \right)$$

where

$$A' = |C_v|^2 + |C_A|^2$$

$$B' = C_v C_A^* + C_A C_v^*$$

$$D' = |C_v|^2 - |C_A|^2$$

$$F' = 2 \operatorname{Im} C_A C_v^*$$

For interaction (2) we find

$$\eta = \frac{y^2}{\mu^3} (A''E_e + mD'')$$

$$a\eta = -\frac{p_e B'' y^2}{\mu^3}$$

$$b\eta = -\frac{p_e B'' y^2}{\mu^3}$$

$$c\eta = \frac{y^2}{\mu^3} (A''m + D''E_e)$$

$$f\eta = \frac{(A'' - D'')(E_e - m)y^2}{\mu^3}$$

$$g\eta = -\frac{p_e y^2 F''}{\mu^3}$$

where

$$A'' = |C_S|^2 + |C_P|^2$$

$$B'' = C_S C_P^* + C_P C_S^*$$

$$D'' = |C_S|^2 - |C_P|^2$$

$$F'' = 2 \operatorname{Im} C_P C_S^*$$

## REFERENCES

- BOUCHIAT, C. and MICHEL, L. 1957. Phys. Rev. **106**, 170L.  
FRAUENFELDER, H. *et al.* 1957. Phys. Rev. **106**, 386.  
FRIEDMAN, M. H. 1957. Phys. Rev. **106**, 387.  
GARWIN, R. L., LEDERMAN, L. M., and WEINRICH, M. 1957. Phys. Rev. **105**, 1415.  
JACKSON, J. D., TREIMAN, S. B., and WYLD, H. W., Jr. 1957. Phys. Rev. **106**, 517.  
LEE, T. D. and YANG, C. N. 1957. Phys. Rev. **105**, 1671.  
PRESTON, M. A. 1957. Can. J. Phys. **35**, 1017.  
WU, C. S., AMBLER, E., HAYWARD, R. W., HOPPES, D. D., and HUDSON, R. P. 1957. Phys. Rev. **105**, 1413.

# ULTRAVIOLET SPECTRA OF LiH AND LiD<sup>1</sup>

R. VELASCO<sup>2</sup>

## ABSTRACT

The absorption spectra of LiH and LiD have been observed in the near ultraviolet with high dispersion and absorbing path lengths up to 16 meters. A new band system has been found in each molecule involving the ground state and a  ${}^1\Pi$  excited state. Rotational and vibrational analyses of this system have been carried out and rotational and vibrational constants for the upper state have been determined. The observed breaking off of the rotational structure of the bands of this  $B\ {}^1\Pi-X\ {}^1\Sigma^+$  system has been interpreted as due to predissociation by rotation. With this assumption very accurate dissociation limits of the  $B\ {}^1\Pi$  state have been obtained. From these dissociation limits the dissociation energies of the three known electronic states of LiH and LiD have been calculated. In particular the dissociation energies ( $D_0$ ) of the ground states of LiH and LiD have been found to be  $2.4288 \pm 0.0002$  ev. and  $2.4509 \pm 0.0010$  ev., respectively.

## INTRODUCTION

The  $A\ {}^1\Sigma^+-X\ {}^1\Sigma^+$  band systems of LiH and LiD have been known for many years, and detailed analyses have been given by Nakamura (1930) and Crawford and Jorgensen (1935). The latter authors were able to use their excellent experimental data to test fine details of the theory of molecular spectra (Crawford and Jorgensen 1936) and to estimate the dissociation energies of the ground states of LiH and LiD. The error in the  $D_0$  values was quite large ( $\pm 0.2$  ev.) because only a few vibrational levels had been observed and the extrapolation from these observed levels to the dissociation limit was rather uncertain.

Since the LiH molecule is a relatively simple one (four electrons) and has been the subject of many theoretical calculations, it would be interesting to have a detailed experimental knowledge to compare with the theory. However, up till now, the  $A\ {}^1\Sigma^+$  state, which lies 3.3 ev. above the ground state, was the only known excited state of LiH. Since the ionization energy of LiH is presumed to be about 8 ev., many more excited states of LiH are to be expected. If a number of these excited states could be observed experimentally they would yield much interesting information about the electronic structure of this molecule. The present experimental work is an attempt to study some of these higher electronic states of LiH and LiD.

## EXPERIMENTAL

The observations were made in absorption. To attain long absorbing paths, an absorption cell equipped with a multiple reflection system of mirrors, of the type first described by White (1942) and modified by Bernstein and Herzberg (1948), was used. Absorption path lengths up to 16 meters were attained.

<sup>1</sup>Manuscript received June 24, 1957.

Contribution from the Division of Pure Physics, National Research Council, Ottawa, Canada.

Issued as N.R.C. No. 4482.

<sup>2</sup>National Research Laboratories Postdoctorate Fellow; present address: Instituto de Optica, Madrid, Spain.

The absorption cell consisted of a steel tube, 180 cm. long and 5 cm. in diameter, whose ends were attached to short pyrex cylinders in which concave mirrors of 2 meter radius of curvature were mounted. A central section of the tube, 1 meter long, was thermally insulated. This central part was electrically heated by connecting it directly across the secondary of a large step-down transformer whose primary voltage could be controlled by means of a variac. In this way, operating temperatures between 800° and 1000° C. could be easily obtained by altering the voltage in the primary, and could be maintained to within  $\pm 25^\circ$  C. The rest of the tube was cooled by means of water jackets at both sides of the hot section.

Pure lithium metal was placed in the center of the tube and the system was evacuated for several hours with the central part heated to about 300° C. The tube was then heated to a higher temperature and  $H_2$  or  $D_2$  was admitted into the tube until the reaction between the gas and the metal stopped. An excess of several cm. Hg pressure of hydrogen was maintained in the tube to prevent a too rapid diffusion of the hydride to the cooler parts of the system. A high pressure Xe-lamp was used as the source for the continuous radiation.

The region between 2000 and 3200 Å was investigated. The final plates were obtained in the third order of a 21 ft. grating spectrograph giving a dispersion of 0.85 Å/mm. The spectra were photographed on 103a-0 Eastman Kodak plates. In order to eliminate overlapping orders in the regions where the bands appear, a Corning-glass filter No. 7-54 was used, sometimes in combination with a nickel sulphate filter (Kasha 1948). Exposure times of about 2 hours were required with the mirrors set to give a path length of 16 meters.

The measurements were made against a Fe-arc comparison spectrum, using as standards the Fe wave lengths given by Harrison (1939) and Edlén (1955). Each band was measured on two different plates with a Gaertner comparator, and the wave lengths in air obtained in this way were reduced to wave numbers by means of Edlén's vacuum correction tables (Edlén 1952).

#### RESULTS AND ANALYSIS

A new band system, observed both in LiH and in LiD, was identified in the region 2880–3080 Å. The new system consists of two groups of bands degraded to the red and separated by about  $1500\text{ cm}^{-1}$  in LiH and  $1000\text{ cm}^{-1}$  in LiD. The individual bands in each group do not stand out very clearly because the rotational structure is very open and the vibrational intervals in the upper state turn out to be rather small. All bands show a clear breaking off of the rotational structure. As will be discussed more fully below, this breaking off can be attributed to rotational predissociation of the upper state.

Plates taken with a low dispersion instrument also show a very strong continuum on the short wave length side of these new bands with maxima of absorption at about 2720 Å (LiH) and 2690 Å (LiD). From the results of our analysis, both the position and the intensity distribution of this continuum agree well with what could be expected if the continuum corresponds to transitions from the ground state to the steep part of the potential curve of the new excited state above the dissociation limit.

Contrary to our expectations no Rydberg series of band systems have been found in the region investigated. The observation of discrete bands below 2800 Å becomes difficult owing to the presence of the strong molecular continuum just mentioned and the still stronger ionization continuum of atomic lithium which begins at 2300 Å. Experiments in the region 1500–2000 Å might be more successful in this respect.

In Tables I and II the wave numbers of the observed lines belonging to the new systems have been listed. Since the mean difference between the wave numbers of the same line obtained from two different plates is  $\pm 0.04 \text{ cm}^{-1}$  we estimate that the wave numbers presented in these tables are probably correct within these limits.

The observed differences between the two groups of bands in each system roughly correspond to the known vibrational frequencies of the ground states of LiH and LiD and the bands in each group may therefore be assigned to  $v'$  progressions. Each band consists of an intense  $Q$  branch, a less intense  $R$  branch, and a still weaker  $P$  branch, thus indicating that the band system arises from a transition in which  $\Delta\Lambda = \pm 1$ . The fact that the lower state of the transition is, as expected, the well-known ground  $^1\Sigma$  state of the molecule is confirmed by the agreement of the combination differences  $\Delta_2 F''(J)$  with the

TABLE I  
WAVE NUMBERS OF THE LINES IN THE  $B^1\Pi - X^1\Sigma^+$  SYSTEM OF LiH

$J$	0-0 band			1-0 band			2-0 band		
	$P(J)$	$Q(J)$	$R(J)$	$P(J)$	$Q(J)$	$R(J)$	$P(J)$	$Q(J)$	$R(J)$
0			34318.03 (4)			34446.58 (4)			34490.12 (1h)
1		34303.21 (6)	314.68 (5)		34431.76 (5)	438.86 (5)		34475.33 (1h)	477.87 (1)
2	34273.67 (2h) <sup>a</sup>	285.05 (8)	302.06 (5)	34402.21 (2)	409.24 (6)	419.42 (4)	—	448.25 (2h)	
3	240.71 (3)	257.62 (8)	279.95 (5)	364.88 (3)	375.07 (8)	387.91 (4)	34403.89 (0)		
4	198.66 (5)	220.86 (8)	248.06 (5)	316.05 (3)	328.89 (5)	343.48 (2)			
5	147.26 (5)	174.36 (8)	205.98 (6)	255.28 (2)	269.77 (4)				
6	086.24 (4)	117.73 (8)	152.98 (3)	181.63 (2)					
7	34015.32 (5)	34050.34 (6)	088.01 (2)						
8	33933.65 (3h)	33971.10 (4)							
9	840.46 (1h)								

$J$	0-1 band			1-1 band			2-1 band		
	$P(J)$	$Q(J)$	$R(J)$	$P(J)$	$Q(J)$	$R(J)$	$P(J)$	$Q(J)$	$R(J)$
0			32958.31 (2)			33086.96 (2h)			33130.7 <sup>c</sup> (0)
1		32943.75 <sup>b</sup> (10)	955.37 (3)		33072.50 (4)	079.62 (3)		33116.0 <sup>c</sup> (0)	118.7 <sup>c</sup> (0)
2	32915.26 (1)	926.64 (5)	943.75 <sup>b</sup> (10)	33043.93 (1)	050.85 (5)	061.03 (3)	—	089.93 (1)	
3	883.60 (3)	900.53 (5)	922.84 (4)	33007.73 (2)	33017.98 (5)	33030.81 (4)	—		
4	843.27 (4)	865.47 (5)	892.61 (4)	32960.63 (2)	32973.39 (5)	32988.13 (3)			
5	793.84 (2)	821.06 (6)	852.66 (4)	901.95 (2)	916.43 (2)				
6	735.38 (1)	766.86 (5)	802.08 (3)	830.87 (1h)					
7	667.25 (2)	702.50 (2)	740.18 (1h)						
8	589.02 (1)	626.60 (3)							
9	499.29 (1)								

<sup>a</sup>Eye-estimate relative intensities. h: diffuse?

<sup>b</sup>Line common to two bands or branches.

<sup>c</sup>It is doubtful if these lines belong to the system. They have not been used in the calculation of constants.



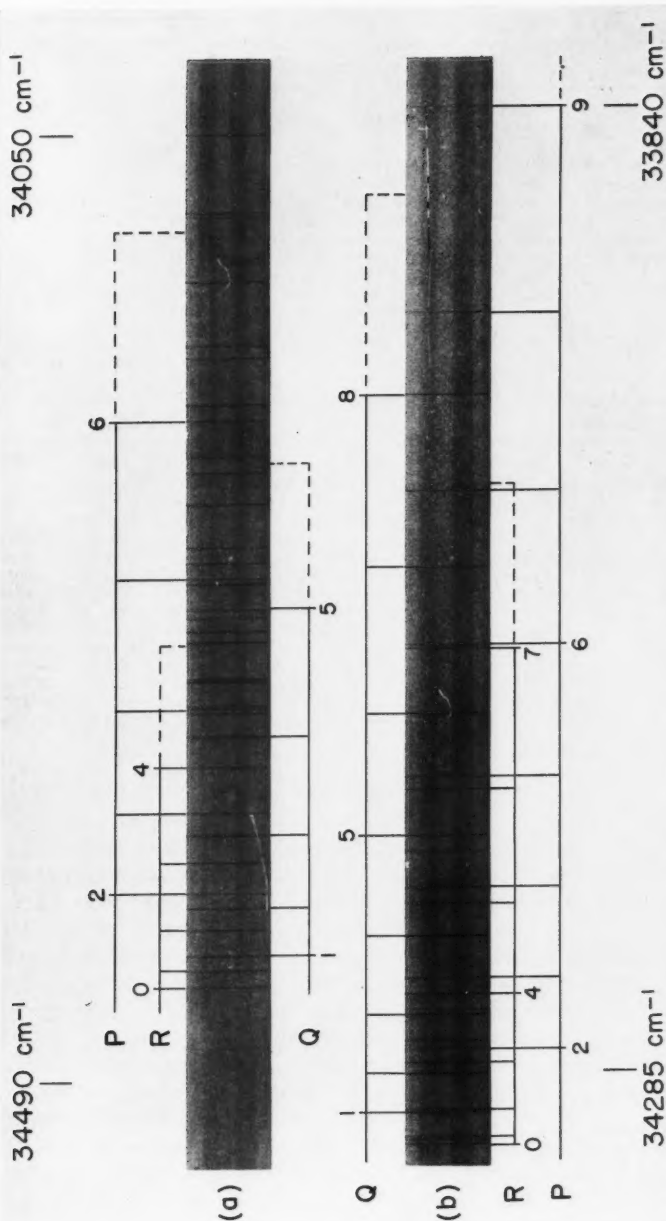


FIG. 1. The  $v'' = 0$  progression of the  $\text{LiH}-X^1\Sigma^+$  system of  $\text{LiH}$ . (a) Rotational structure of the 1-0 band. (b) Rotational structure of the 2-0 band. A few very weak lines on the left-hand side of the 1-0 band belong to the 2-0 band. The broken lines indicate the position of the first missing line in the corresponding branch.

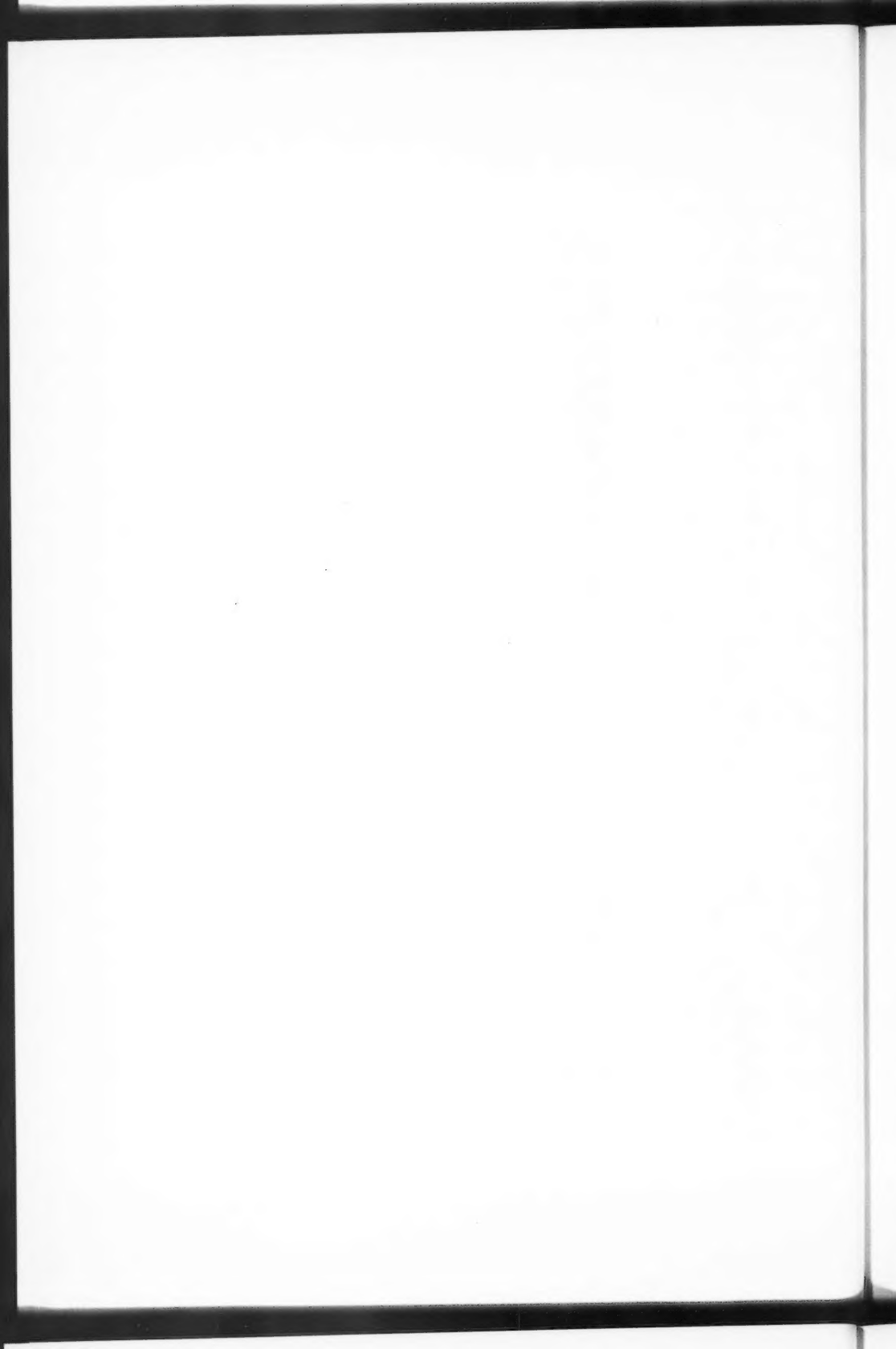


TABLE II  
WAVE NUMBERS OF THE LINES IN THE  $B\ ^1\Pi-X\ ^1\Sigma^+$  SYSTEM OF LiD

J	0-0 band			1-0 band			2-0 band		
	P(J)	Q(J)	R(J)	P(J)	Q(J)	R(J)	P(J)	Q(J)	R(J)
0			34469.59 (1)			34587.86 (1)			34647.59 (0)
1		34461.27 <sup>b</sup> (4)	467.98 (2)		34579.39 (2)	584.31 (3h)		34639.30 (1h)	642.46 (0h)
2	—	451.24 (2h)	461.27 <sup>b</sup> (4)	34562.56 (0)	567.58 (3)	575.00 (2)	—	625.68 (2h)	630.36 (0h)
3	34426.22 (3)	436.23 (3)	449.57 (2)	542.42 <sup>b</sup> (4)	549.87 <sup>b</sup> (5)	559.55 (4)	—	605.12 (3h)	611.01 (1h)
4	402.91 (1)	416.11 <sup>d</sup> (5)	432.70 (3)	516.50 (2h)	526.02 (5)	537.83 (3)	34571.95 (0)	577.37 (2)	584.31 (3h)
5	374.47 (2h)	390.88 (5)	410.46 (1)	484.33 (2h)	496.07 (5)	509.68 (2h)	535.74 (0)	542.42 <sup>b</sup> (4)	549.87 <sup>b</sup> (5)
6	340.95 (3)	360.35 (3)	382.86 (2)	446.04 (2)	459.61 (4)	474.97 (2h)	492.71 (1)	499.52 (2h)	
7	302.10 (2h)	324.45 (4)	349.70 (1)	401.51 (1)	416.54 <sup>d</sup> (5)	432.70 (3)	—		
8	257.94 (3h)	283.05 (3)	310.63 (2h)	350.19 (1)	366.39 (3)	382.86 (2)			
9	208.56 (2)	235.89 (3)	265.41 (0h)	291.93 (1)	308.21 (3)				
10	153.20 (2)	182.58 (3)	213.77 (0)	225.62 (0)					
11	091.90 (0h)	122.84 (2h)	154.41 (1)						
12	024.50 (1)	055.71 (0)							
13	—								

J	0-1 band			1-1 band			2-1 band		
	P(J)	Q(J)	R(J)	P(J)	Q(J)	R(J)	P(J)	Q(J)	R(J)
0			33440.50 (2h)			33558.79 (2)			33618.65 (1)
1		33432.51 (2)	439.21 (2)		33550.60 (5)	555.54 (3)		33610.43 (2)	613.59 (2)
2	33416.06 (0)	422.78 (3)	432.87 (2)	33534.26 (1h)	539.20 (6)	546.53 (3)	33594.19 (0h)	597.19 (4)	601.69 (3)
3	398.23 (1)	408.24 (4)	421.61 (3)	514.71 (2h)	522.01 (3)	531.59 (3)	572.52 (1h)	577.14 (4)	582.97 (3)
4	375.62 (2)	388.89 (5)	405.41 (4)	489.27 (3)	498.88 (5)	510.59 (4)	544.46 (1)	550.32 (5)	556.97 (2)
5	348.08 (3)	364.53 (5)	384.07 (4)	458.10 (4)	469.77 (5)	483.41 (4)	509.46 (1)	516.12 (3)	523.31 (1)
6	315.63 (3)	335.09 (5)	357.51 (3)	420.85 (3)	434.43 (6)	449.60 (4)	467.24 (1)	474.19 (1)	
7	278.16 (3)	300.48 (5)	325.54 (3)	377.39 (4)	392.61 (5)	408.86 (1)	417.38 (1)		
8	235.50 (3)	260.48 (5)	287.97 (2)	327.62 (3)	343.81 (4)	360.31 (1h)			
9	187.55 (3)	214.96 (5)	244.45 (2)	270.88 (1)	287.29 (2)				
10	134.12 (4)	163.44 (3)	194.61 (1)	206.48 (1)					
11	074.74 (2)	105.62 (3)	137.35 (0)						
12	33009.19 (1)	040.87 (3)							
13	32936.82 (1)								

<sup>a, b, c</sup> All symbols as in Table I.

<sup>d</sup>Line blended with another one and difficult to measure.

values given by Crawford and Jorgensen (1935) for the  $v'' = 0$  and  $v'' = 1$  levels of the ground state. Since the lower state is a  $^1\Sigma$  state it follows that the upper state must be a  $^1\Pi$  state. A reproduction of the  $v'' = 0$  progression of this  $B\ ^1\Pi-X\ ^1\Sigma^+$  system of LiH is given in Fig. 1.

The consistency of our measurements and a comparison of our results with those of Crawford and Jorgensen can be seen in Tables III and IV, which contain sets of  $\Delta_2 F(J)$  values for the ground and excited states of LiH and LiD.

Because of the agreement of our combination differences  $\Delta_2 F''(J)$  with those of Crawford and Jorgensen, the accurate rotational constants given by these authors for the ground state were adopted and used in our calculations. Rotational constants for the  $B\ ^1\Pi$  level were obtained in two ways:

(i) *Bands with eight or more lines in each branch.*—From our observed lines and the  $F''(J)$  values obtained by Crawford and Jorgensen for the  $v'' = 0$  and  $v'' = 1$  levels of the ground state,  $F'(J)$  values were calculated, both for the

TABLE III  
COMBINATION DIFFERENCES  $\Delta_2 F_0''(J)$  IN THE GROUND STATE OF LiH AND LiD

<i>J</i>	LiH		LiD	
	0-0 band $^1\Pi-^1\Sigma$ system	Average $^1\Sigma-^1\Sigma$ system*	0-0 band $^1\Pi-^1\Sigma$ system	Average $^1\Sigma-^1\Sigma$ system*
1	44.36	44.43	—	25.14
2	73.97	73.94	41.76	41.87
3	103.40	103.39	58.36	58.52
4	132.69	132.66	75.10	75.18
5	161.82	161.78	91.75	91.79
6	190.66	190.68	108.36	108.29
7	219.33	219.27	124.92	124.71
8	247.55	247.65	141.14	141.05
9			157.43	157.26
10			173.51	173.39
11			186.27	186.36
Mean diff.	$\pm 0.05 \text{ cm}^{-1}$		$\pm 0.12 \text{ cm}^{-1}$	

\*Data from Crawford and Jorgensen (1935).

TABLE IV  
COMBINATION DIFFERENCES  $\Delta_2 F_0(J)$  IN THE  $B\ ^1\Pi$  STATE OF LiH AND LiD

<i>J</i>	LiH		LiD	
	0-0 band	0-1 band	0-0 band	0-1 band
2	28.39	28.49	—	16.61
3	39.24	39.24	23.35	23.38
4	49.40	49.34	29.79	29.79
5	58.72	58.82	35.99	35.99
6	66.74	66.70	41.91	41.88
7	72.69	72.83	47.60	47.38
8			52.69	52.47
9			56.85	56.90
10			60.57	60.49
11			62.51	62.61
Mean diff.	$\pm 0.07 \text{ cm}^{-1}$		$\pm 0.08 \text{ cm}^{-1}$	

series of rotational levels obtained from the *Q* branches, and for those obtained from the *P* and *R* branches, to obtain two sets of constants. The first differences,  $\Delta_1 F'(J+\frac{1}{2})$ , obey the following relation:

$$(1) \quad \Delta_1 F'(J+\frac{1}{2})/2(J+1) = B_e - (2D_e - H_e)(J+1)^2 + 3H_e(J+1)^4$$

and therefore, by plotting the left-hand side of this formula versus  $(J+1)^2$ ,  $B_e$  was found as the intercept on the ordinate axis. Using the value  $B_e$  obtained in this manner,  $([\Delta_1 F'(J+\frac{1}{2})/2(J+1)] - B_e)/(J+1)^2$  was calculated and plotted in turn versus  $(J+1)^2$ . In each case a straight line could be drawn whose intercept gave  $-(2D_e - H_e)$  and whose slope gave  $3H_e$ .

(ii) *Bands with less than eight lines in each branch.*—A similar method was followed, but this time

$$F'(J)/J(J+1) = B_e - D_e J(J+1) + H_e J^2(J+1)^2$$

was used as starting formula instead of (1) and  $F'(J)/J(J+1)$  was plotted versus  $J(J+1)$ .

In each case the constants were checked by recalculating the  $F'(J)$  values and comparing them with the observed ones.

There is evidence of some  $\Lambda$  splitting in the  $B^1\Pi$  state, both in LiH and in LiD, with the  $Q$  branches arising from the  $a$  levels and the  $P$  and  $R$  branches from the  $b$  levels, but for such short bands the observed combination defects are of the order of magnitude of the experimental errors and no good analysis of this doubling could be made.

The constants obtained as a result of the rotational analysis are given in Tables V and VI.

TABLE V  
ROTATIONAL CONSTANTS FOR THE UPPER STATE OF THE  $B^1\Pi-X^1\Sigma$  BANDS OF LiH and LiD

Band	$B'_e$		$D_e \times 10^3$		$-H'_e \times 10^6$	
	$B^a$	$B^b$	$D^a$	$D^b$	$-H^a$	$-H^b$
LiH						
0-0	2.880	2.880	2.7	2.7	1.5	1.5
0-1	2.875	2.880	2.4	2.3	1.8	2.0
1-0	1.800	1.807	4.3	5.2	7.0	4.0
1-1	1.800	1.809	4.3	5.2	7.0	4.5
2-0	0.64	0.64	—	—	—	—
LiD						
0-0	1.691	1.696	0.74	0.78	0.25	0.25
0-1	1.691	1.692	0.76	0.76	0.24	0.24
1-0	1.252	1.255	1.35	1.35	0.54	0.53
1-1	1.254	1.253	1.40	1.40	0.54	0.50
2-0	0.799	0.804	2.01	1.98	1.54	1.58
2-1	0.801	0.807	1.91	2.16	1.99	1.47

<sup>a</sup>From  $Q$  branches.

<sup>b</sup>From  $P$  and  $R$  branches.

TABLE VI  
MEAN ROTATIONAL CONSTANTS FOR THE VIBRATIONAL LEVELS OF THE  
 $B^1\Pi$  STATE OF LiH AND LiD

Constant	Molecule	$v = 0$	$v = 1$	$v = 2$
$B_e$	LiH	2.879	1.804	0.64
	LiD	1.693	1.254	0.803
$D_e \times 10^3$	LiH	2.6	4.8	—
	LiD	0.76	1.38	2.02
$-H_e \times 10^6$	LiH	1.7	5.6	—
	LiD	0.25	0.53	1.65

The observed  $B_e$ ,  $D_e$ , and  $H_e$  values of the  $B^1\Pi$  state can be represented by the following formulae:

$$\begin{array}{l}
 \text{LiH} \quad \left[ \begin{array}{l} B_v = 3.383 - 0.986(v + \frac{1}{2}) - 0.045(v + \frac{1}{2})^2 \\ 10^3 \times D_v = 1.5 + 2.2(v + \frac{1}{2}) \\ 10^5 \times H_v = 0.3 - 3.9(v + \frac{1}{2}) \end{array} \right. \\
 \\
 \text{LiD} \quad \left[ \begin{array}{l} B_v = 1.908 - 0.427(v + \frac{1}{2}) - 0.006(v + \frac{1}{2})^2 \\ 10^3 \times D_v = 0.44 + 0.63(v + \frac{1}{2}) \\ 10^5 \times H_v = 0.13 - 0.56(v + \frac{1}{2}) - 0.42(v + \frac{1}{2})^2 \end{array} \right.
 \end{array}$$

Not enough information has been obtained for the  $B \ ^1\Pi$  state of LiH and LiD to attempt a correction of these constants in the same way that was done by Crawford and Jorgensen for the ground state and the  $A \ ^1\Sigma^+$  state.

The results of the vibrational analysis are presented in Table VII, which contains Deslandres arrays of the band origins of the observed bands of LiH and LiD. The vibrational numbering for the ground state follows immediately

TABLE VII  
DESLANDRES TABLES OF THE  $B \ ^1\Pi-X \ ^1\Sigma^+$  BANDS OF LiH AND LiD

$v'$	LiH		LiD		
	$v'' = 0$		$v'' = 0$		$v'' = 1$
0	34312.26 130.73	(1359.64)	32952.62 130.72	34466.27 119.00	(1029.03) 33437.24 119.05
1	34442.99 45.9	(1359.65)	33083.34 46.0	34585.27 60.82	(1028.98) 33556.29 60.73
2	34488.9	(1359.6)	33129.3	34646.09	(1029.07) 33617.02

from the rotational analysis, but for the upper state the numbering is not so obvious. The numbering proposed has been adopted because it is the only one for which the isotopic relations for the rotational and vibrational constants are fulfilled. With this numbering the observed vibrational levels of the  $B \ ^1\Pi$  states can be represented by the following expressions:

$$\text{LiH: } G_v = 215.5(v + \frac{1}{2}) - 42.4(v + \frac{1}{2})^2$$

$$\text{LiD: } G_v = 177.28(v + \frac{1}{2}) - 29.13(v + \frac{1}{2})^2$$

The rotational and vibrational constants of LiH and LiD in the  $B \ ^1\Pi$  state, which have been determined in the present investigation, are summarized in Table VIII. For comparison, the constants of LiD calculated from those of LiH by means of the isotopic conversion factors  $\rho^n$  (where  $\rho = (\mu_{\text{LiH}}/\mu_{\text{LiD}})^{\frac{1}{2}}$ ) given by the elementary isotope theory (Herzberg 1950) are given in the last column. From the values in this table it can be seen that in spite of the large amount of anharmonicity the isotopic relations hold fairly well, especially for those constants that have been most accurately determined ( $B_e$  and  $\alpha_e$ ).

#### DISCUSSION

The observed breaking off of the rotational structure of the  $B \ ^1\Pi-X \ ^1\Sigma^+$  bands of LiH and LiD occurs at values of  $J'$  which are the same for all the branches of a particular band and decrease with increasing  $v'$ , thus proving that the perturbed state must be the upper state. That this perturbation can be

TABLE VIII  
 MOLECULAR CONSTANTS OF THE  $B^1\Pi$  STATE OF LiH AND LiD ( $\text{cm}^{-1}$ )

Constant	LiH obs.	LiD obs.	$\rho^a$ *	LiD calc. = LiH $\times \rho^a$
$B_e$	3.383	1.908	$\rho^2 = 0.563135$	1.905
$D_e \times 10^3$	1.5	0.44	$\rho^4 = 0.317121$	0.48
$H_e \times 10^5$	0.3	0.13	$\rho^6 = 0.178582$	0.05
$\alpha_e$	0.986	0.427	$\rho^3 = 0.422589$	0.417
$\gamma_e$	0.045	0.006	$\rho^4 = 0.317121$	0.014
$\beta_e \times 10^3$	2.2	0.63	$\rho^5 = 0.237975$	0.52
$\delta_e \times 10^5$	3.9	0.56	$\rho^7 = 0.134012$	0.52
$\omega_e$	215.5	177.28	$\rho = 0.750423$	161.7
$\omega_e x_e$	42.4	29.13	$\rho^2 = 0.563135$	23.9
$T_e$	34912	34909	—	—
$r_e$ (Å)	2.378	2.376	—	—

\*Atomic masses used:  $H^1 = 1.008131$ ,  $H^2 = 2.014725$ ,  $Li^7 = 7.018163$  (Mattauch 1946).

attributed to predissociation by rotation<sup>3</sup> is deduced by plotting the energies of the last observed and the first missing rotational levels of the upper state as a function of  $J'(J'+1)$ . Assuming that for each vibrational level the real breaking off points lie between the last observed and the first missing rotational level, the limiting curve of dissociation (Fig. 2) was drawn. The shape of this curve, with horizontal tangent at  $J'(J'+1) = 0$ , corresponds to that which

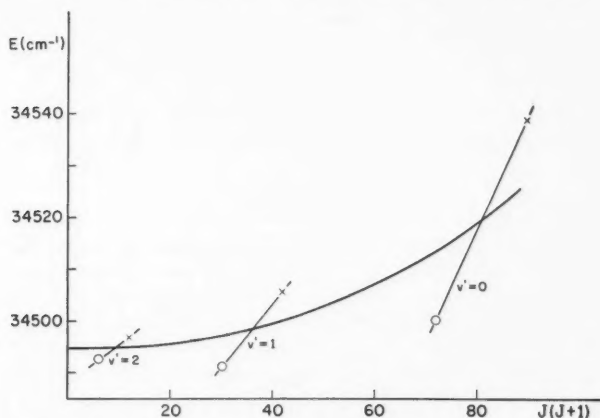


FIG. 2. Limiting curve of dissociation for the  $B^1\Pi$  state of LiH.  
 ○ = Last observed rotational levels.  
 × = First missing rotational levels.

would be expected from a rotational predissociation in which the potential curve of the rotationless state has no maximum (or if any maximum exists it could only be at a very large internuclear distance and therefore extremely small). Furthermore this appears to be the only possible explanation for the

<sup>3</sup>Case III of predissociation (Herzberg 1950).

observed predissociation. If it were due to overlapping with the continuum of either of the two lower  $^1\Sigma^+$  states the breaking off would be present only in the  $P$  and  $R$  branches, which is contrary to observation. The remote possibility that the perturbation was due to interaction with the  $^3\Sigma$  state, arising from normal Li and H atoms, is excluded by the absence of a maximum in the potential curve of the rotationless state.

A breaking off of the rotational structure of a band system observed in absorption is expected if predissociation occurs in the ground state. What is normally observed when the predissociated state is the upper state is a gradual increase in diffuseness of those lines involving rotational levels above the dissociation limit. The apparent breaking off observed in this particular example could be explained by the fast onset of predissociation (due to the extreme shallowness of the  $B\ ^1\Pi$  state), which in some cases does not even allow the observation of levels above the dissociation limit (Fig. 3).

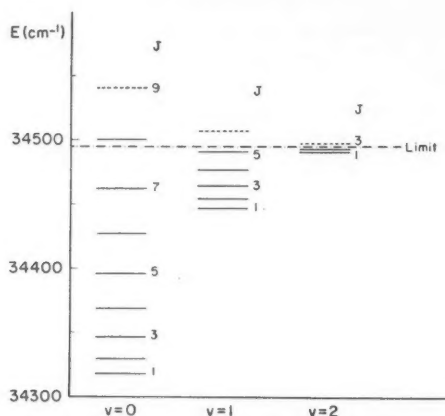


FIG. 3. Rotational levels of the  $B\ ^1\Pi$  state of LiH. The broken lines indicate the calculated position of the first missing levels.

The intensity distribution in the rotational structure of the bands  $B\ ^1\Pi-X\ ^1\Sigma^+$ , especially in bands involving levels with  $v' = 1$  and  $v' = 2$ , does not follow the usual pattern deduced from simple considerations about the thermal distribution of rotational levels in the ground state. This effect is not clearly understood but perhaps it might also be related to the fact that the upper electronic state is extremely shallow. It is believed that it does not affect our interpretation of the observed breaking off.

Accepting that the breaking off is due to predissociation by rotation, and that the rotationless potential curves of the  $B\ ^1\Pi$  state of LiH and LiD have no maximum, the extrapolation of the limiting curve of dissociation will intersect the ordinate axis at a point giving the dissociation limit. In this particular example the extrapolation is very short and accurate. In the last observed vibrational levels the rotational constant  $B_v$  is rather small and



in these levels very few stable rotational levels exist below the breaking off point, thus producing very little uncertainty in the extrapolation. The dissociation limits obtained for the  $B\ ^1\Pi$  state of LiH and LiD are  $34495 \pm 2\text{ cm}^{-1}$  and  $34673 \pm 8\text{ cm}^{-1}$ , respectively.

Because of the simplicity of the electronic structure of the Li-atom it is clear that the only possible dissociation products of this  $B\ ^1\Pi$  electronic state of lithium hydride are one hydrogen atom in its ground state and one lithium atom in the  $2p$  excited state. With regard to the other two known electronic states we assume that  $A\ ^1\Sigma^+$  also dissociates into  $H(1s^2S)$  and  $Li(2p^2P)$  (Mulliken 1936; Rosenbaum 1938), and that the  $X\ ^1\Sigma^+$  state dissociates into normal atoms as is generally admitted. Therefore, from the observed dissociation limits of the  $B\ ^1\Pi$  states the following values for the dissociation energies of the three observed electronic states of LiH and LiD are obtained:

$$\begin{aligned} D_0(B\ ^1\Pi) \quad & \left[ \begin{array}{l} \text{LiH: } 183\text{ cm}^{-1} = 0.0227\text{ ev. } (\pm 0.0002\text{ ev.})^4 \\ \text{LiD: } 207\text{ cm}^{-1} = 0.0257\text{ ev. } (\pm 0.0010\text{ ev.}) \end{array} \right. \\ D_0(A\ ^1\Sigma^+) \quad & \left[ \begin{array}{l} \text{LiH: } 8552\text{ cm}^{-1} = 1.0602\text{ ev. } (\pm 0.0002\text{ ev.}) \\ \text{LiD: } 8590\text{ cm}^{-1} = 1.0650\text{ ev. } (\pm 0.0010\text{ ev.}) \end{array} \right. \\ D_0(X\ ^1\Sigma^+) \quad & \left[ \begin{array}{l} \text{LiH: } 19591\text{ cm}^{-1} = 2.4288\text{ ev. } (\pm 0.0002\text{ ev.})^5 \\ \text{LiD: } 19769\text{ cm}^{-1} = 2.4509\text{ ev. } (\pm 0.0010\text{ ev.})^5 \end{array} \right. \end{aligned}$$

To obtain the corresponding dissociation energies,  $D_e$ , referred to the equilibrium position, the zero point energy of the electronic level must be added to each  $D_0$  value. The expression for the zero point energy is

$$E_0 = E_0^* + Y_{00} = \frac{1}{2}\omega_e - \frac{1}{4}\omega_e x_e + \frac{1}{8}\omega_e y_e + \dots + Y_{00},$$

where  $Y_{00}$  is the finer correction due to anharmonicity (Dunham 1932). In terms of the observed constants this correction can be expressed as follows:<sup>6</sup>

$$Y_{00} = \frac{B_e}{4} + \frac{\alpha_e \omega_e}{12B_e} + \frac{\alpha_e^2 \omega_e^2}{144B_e^3} - \frac{\omega_e x_e}{4}.$$

In this way the dissociation energies for the vibrationless states were computed and the results are given in Table IX.

The agreement between the values of  $D_e$  for the two isotopic molecules is very good, and supports the interpretation of the breaking off as given above. A systematic shift of 4 or 5  $\text{cm}^{-1}$  can be explained by the errors in the determination of the dissociation limits. The remaining differences are mainly due to the uncertainties in the zero point energy calculations. If any real electronic isotope shift of the energy differences  $B\ ^1\Pi - X\ ^1\Sigma^+$  and  $A\ ^1\Sigma^+ - X\ ^1\Sigma^+$  is present it must be rather small.

<sup>4</sup>The conversion factor  $1.239767 \times 10^{-4}$  has been used to convert  $\text{cm}^{-1}$  into ev.

<sup>5</sup>In computing these dissociation energies the value  $\Delta\nu = 14904\text{ cm}^{-1}$  for the difference between the  $2p$  and  $2s$  atomic states of Li has been used (Moore 1949).

<sup>6</sup>This expression is obtained directly from Dunham's formulae. In Herzberg's book (Herzberg 1950) the factor  $\frac{1}{4}$  in the last term is inadvertently omitted.

<sup>7</sup>Owing to a numerical error in the calculation of  $Y_{00}$ , Crawford and Jorgensen (1936) did not apply this correction to their calculation of the term values of the  $A\ ^1\Sigma^+$  state of LiH and LiD. Applying it, the values obtained are:  $A\ ^1\Sigma^+$  (LiH) = 26509.6 and  $A\ ^1\Sigma^+$  (LiD) = 26510.4.

TABLE IX  
DISSOCIATION ENERGIES OF THE THREE KNOWN ELECTRONIC STATES OF LiH and LiD

State	Molecule	$D_0$	$E_0^*$	$Y_{00}$	$D_e^\dagger$	$D_e$ (ev.)	Limit of error $^\ddagger$ (ev.)
$B\ ^1\Pi$	LiH	183	97.2	3.6	284	0.035	$\pm 0.001$
	LiD	207	81.4	2.2	291	0.036	$\pm 0.002$
$A\ ^1\Sigma^+$	LiH	8552	123.9	7.5	8683	1.0765	$\pm 0.0002$
	LiD	8590	93.7	3.8	8687	1.0770	$\pm 0.0010$
$X\ ^1\Sigma^+$	LiH	19591	697.1	0.8	20289	2.5154	$\pm 0.0002$
	LiD	19769	524.3	0.4	20294	2.5160	$\pm 0.0010$

$^\dagger$ The values in columns 3, 4, 5, and 6 are in  $\text{cm}^{-1}$ .

$^\ddagger$ Taking into account the uncertainties due to the zero point energy calculation.

#### ACKNOWLEDGMENTS

The author is deeply indebted to Dr. G. Herzberg for suggesting the problem and for his kind interest during the course of it. Special thanks are due to Dr. A. E. Douglas for his constant advice and encouragement, and to Dr. B. Kleman and Dr. S. R. Polo for many helpful discussions.

#### REFERENCES

- BERNSTEIN, H. J. and HERZBERG, G. 1948. *J. Chem. Phys.* **16**, 30.  
 CRAWFORD, F. H. and JORGENSEN, T., JR. 1935. *Phys. Rev.* **47**, 358, 932.  
 ——— 1936. *Phys. Rev.* **49**, 745.  
 DUNHAM, J. L. 1932. *Phys. Rev.* **41**, 721.  
 EDLÉN, B. 1952. Vacuum corrections for wave lengths from 2000 to 13500 Å (Lund University, Sweden).  
 ——— 1955. Wave lengths in the iron arc in air (Lund University, Sweden).  
 HARRISON, G. R. 1939. M.I.T. wavelength tables (John Wiley & Sons, Inc., New York).  
 HERZBERG, G. 1950. Spectra of diatomic molecules (D. Van Nostrand Co. Inc., Princeton, N.J.).  
 KASHA, M. 1948. *J. Opt. Soc. Am.* **38**, 929.  
 MATTAUCH, J. 1946. Nuclear physics tables (Interscience Publ. Inc., New York).  
 MOORE, C. E. 1949. Atomic energy levels, N.B.S. Circular 467 (Washington, D.C.).  
 MULLIKEN, R. S. 1936. *Phys. Rev.* **50**, 1028.  
 NAKAMURA, G. 1930. *Z. Physik*, **59**, 218.  
 ROSENBAUM, E. J. 1938. *J. Chem. Phys.* **6**, 16.  
 WHITE, J. U. 1942. *J. Opt. Soc. Am.* **32**, 285.

# REACTOR NEUTRON CAPTURE CROSS SECTION OF 51-DAY $\text{Sr}^{89}$ <sup>1</sup>

L. P. ROY AND J. C. ROY

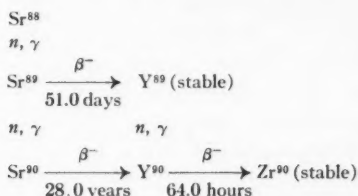
## ABSTRACT

The neutron capture cross section of  $\text{Sr}^{89}$  has been measured by an activation method. Naturally occurring strontium was irradiated in different high flux positions in the NRX reactor at Chalk River and the amount of  $\text{Sr}^{90}$  formed by successive neutron capture in  $\text{Sr}^{88}$  was determined by separating and measuring its daughter  $\text{Y}^{90}$ . Using values of 36.6 and 0.005 barns for the respective neutron capture cross sections of  $\text{Co}^{59}$  and  $\text{Sr}^{88}$ , the capture cross section of  $\text{Sr}^{89}$  for reactor spectrum neutrons was found to be  $0.49 \pm 0.10$  barn.

## A. INTRODUCTION

The 51.0-day  $\text{Sr}^{89}$  is a fission product of fairly high yield and can be a potential reactor poison if its neutron capture cross section to form  $\text{Sr}^{90}$  is large enough. Radiostrontium is biologically important and  $\text{Sr}^{90}$  is more important than  $\text{Sr}^{89}$  because of its longer half-life. The precise estimation of the amount of  $\text{Sr}^{90}$  present in spent fuel from high flux, high burn-up reactors is required in planning fission product disposal. It is of some interest therefore to obtain a better value than the upper limit of 108 barns given by Katcoff (1951a) for the neutron capture cross section of  $\text{Sr}^{89}$ .

The reactor neutron capture cross section of  $\text{Sr}^{89}$  has been measured by an activation method. Naturally occurring strontium (82.7%  $\text{Sr}^{88}$ ) was irradiated in the NRX reactor at Chalk River, and  $\text{Y}^{90}$ , the daughter of  $\text{Sr}^{90}$ , (formed by successive neutron capture) was measured. The nuclear reactions involved are:



The  $\text{Y}^{90}$  formed is easily identified by its 64.0-hour half-life and 2.26 Mev.  $\beta$ -ray (Johnson *et al.* 1955).

The mathematical relation used to compute the cross section of  $\text{Sr}^{89}$  has been derived by Katcoff (1951b) and is

$$(1) \quad A_B = \frac{N_{SS} \sigma_A \phi^2 T_A}{0.693(T_A - T_B)} [T_A(1 - e^{-\lambda_A t}) - T_B(1 - e^{-\lambda_B t})].$$

$A_B$  is the disintegration rate of  $\text{Sr}^{90}$  at the end of the irradiation, which is equal at equilibrium to  $\text{Y}^{90}$  activity.

<sup>1</sup>Manuscript received July 18, 1957.

Contribution from the Research Chemistry Branch, Atomic Energy of Canada Limited, Chalk River, Ontario.

Issued as A.E.C.L. No. 489.

$N_S$  is the number of  $\text{Sr}^{88}$  atoms initially present.

$\sigma_S$  is the neutron capture cross section of  $\text{Sr}^{88}$  equal to  $0.005 \pm 0.001$  barn (Hughes and Harvey 1955).

$\sigma_A$  is the neutron capture cross section of  $\text{Sr}^{89}$  to be determined.

$t$  is the time of irradiation.

$\phi$  is the neutron flux.

$T_A$  is the half-life of  $\text{Sr}^{89}$ ; taken to be 51.0 days (Kjelberg and Pappas 1956).

$T_B$  is the half-life of  $\text{Sr}^{90}$ ; taken to be 28.0 years (Flynn *et al.* 1955; Wiles and Tomlinson 1955).

$\lambda_A$  is the decay constant of  $\text{Sr}^{89}$ .

$\lambda_B$  is the decay constant of  $\text{Sr}^{90}$ .

## B. EXPERIMENTAL

Three samples of spectroscopically pure strontium carbonate (obtained from Johnson, Matthey and Co. Limited) were irradiated in aluminum capsules in the NRX reactor at Chalk River at different neutron fluxes for different times. The chemical separations were started about four months after the end of the irradiation. Thus  $\text{Y}^{90}$  produced by the  $(n, \gamma)$  reaction on  $\text{Y}^{89}$  formed by the decay of  $\text{Sr}^{89}$  or by  $(n, p)$  and  $(n, \alpha)$  reactions on zirconium and niobium impurities will have decayed. The strontium carbonate samples were dissolved in 1 *M* hydrochloric acid. Then several ferric and yttrium hydroxide scavengings were made by addition of gaseous ammonia and the precipitates were discarded. The solution was made slightly acid after the excess ammonia was boiled off and a known amount of yttrium carrier was added. After a delay period of 1 week to allow for  $\text{Y}^{90}$  growth, the yttrium was precipitated with gaseous ammonia. The precipitate was centrifuged and washed once with distilled water. The supernatant and the washing were kept for the subsequent separations. The yttrium precipitate was dissolved in dilute hydrochloric acid and about 20 mg. of strontium holdback carrier was added. The yttrium was precipitated again as hydroxide, centrifuged, and washed. This purification step was repeated four times. Finally the yttrium hydroxide was dissolved in dilute hydrochloric acid and precipitated as oxalate with 4 ml. saturated oxalic acid. The precipitate was centrifuged, washed twice with boiling distilled water, twice with ethanol, and twice with ether, deposited on an aluminum tray, dried for 1 minute under an infrared lamp, and weighed as  $\text{Y}_2(\text{C}_2\text{O}_4)_3 \cdot 7\text{H}_2\text{O}$ , according to the method described by Milton and Grummitt (1957). The chemical yields were between 60 and 85%.

The disintegration rate of yttrium fractions was determined with an anthracene  $\beta$ -counter having a window thickness of 2.16 mg./cm.<sup>2</sup>; its background was 10 c.p.m. The counter was calibrated with a standardized source of  $\text{P}^{32}$ , obtained from the National Bureau of Standards in Washington, and the geometry used in the measurements was 32%. In a separate experiment using pure  $\text{Y}^{90}$  it was found that for the particular way in which the yttrium oxalate samples were mounted, self-absorption and back-scattering effects cancelled each other so that no corrections for these factors were required.

## C. RESULTS

Yttrium-90 was identified mainly by its decay period measured over four

or five half-lives. After a small residual activity due to the 51-day  $\text{Sr}^{89}$  was subtracted, the measured values of the half-lives for the different fractions of  $\text{Y}^{90}$  were between 61 and 65 hours. Fig. 1 shows a decay curve for one of the  $\text{Y}^{90}$  samples. The absorption of the beta radiations by aluminum showed

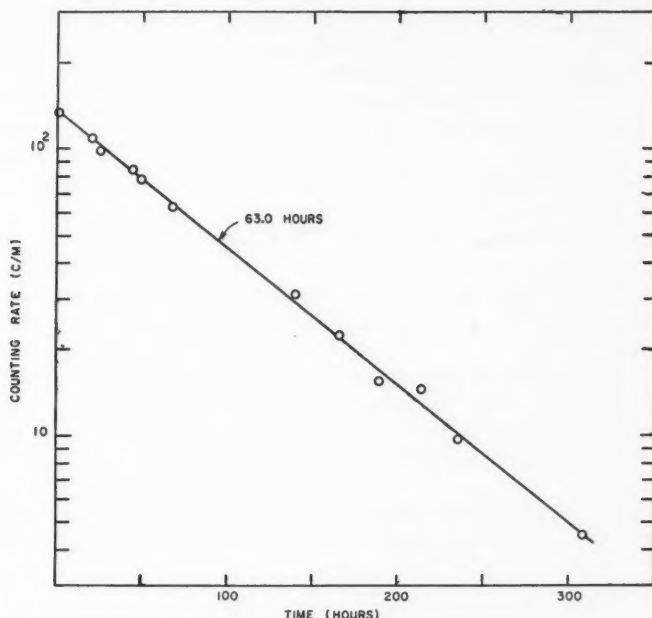


FIG. 1. Decay curve of  $\text{Y}^{90}$ . A long-lived background of 15 c.p.m. has been subtracted from the original data to obtain this curve.

TABLE I

NEUTRON CAPTURE CROSS SECTION OF  $\text{Sr}^{89}$  OBTAINED BY IRRADIATION OF  $\text{Sr}^{88}$  AT DIFFERENT NEUTRON FLUXES AND AT TWO DIFFERENT IRRADIATION TIMES

Sample No.	Amount of $\text{SrCO}_3$ irradiated, g.	Irradiation time in NRX reactor, days	Neutron flux, n./cm. <sup>2</sup> /sec.	$\text{Y}^{90}$ in equilibrium with $\text{Sr}^{90}$ , dis./min.	$\sigma_A$ ( $\text{Sr}^{89}$ ) barn
A-Y-1	0.16805	35.63	$3.73 \times 10^{13}$	343	0.48
A-Y-2				297	0.41
A-Y-3				353	0.49
A-Y-4				347	0.48
A-Y-5				335	0.47
B-Y-1	0.17073	35.63	$4.91 \times 10^{13}$	629	0.50
B-Y-2				617	0.49
B-Y-3				576	0.46
C-Y-1	0.15425	16.41	$7.08 \times 10^{13}$	286	0.50
C-Y-2				310	0.55
C-Y-3				282	0.50
C-Y-4				299	0.53
Average					0.49

that their maximum energy was at least 2 Mev. The low activity of  $Y^{90}$  fractions prevented any better determination of the end point.

The results are summarized in Table I. The observed counting rates were extrapolated to the time of separation and the absolute disintegration rates were obtained after correction for chemical yield, time of growth of  $Y^{90}$ , decay of  $Sr^{90}$  from the end of the irradiation to the time of separation, and counting efficiency of the  $\beta$ -detector. The letters A, B, and C refer to the three samples of strontium irradiated at different fluxes; Y-1, Y-2, and so on refer to the repeated parent-daughter separations made a week apart for a given sample of strontium.

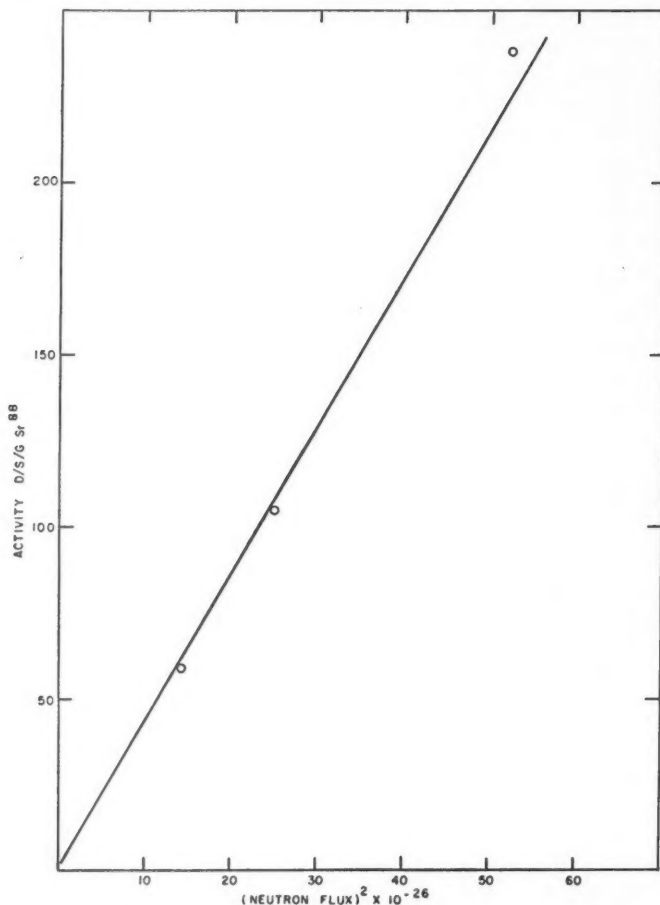


FIG. 2. Variation of  $Y^{90}$  activity per gram of  $Sr^{88}$  irradiated as the square of the neutron flux.

The neutron fluxes quoted are average values obtained in the same experiment using pure cobalt wire 0.005 inch in diameter and 0.4 inch in length as flux monitor. The activity in cobalt was measured with an ionization chamber calibrated with standardized  $\text{Co}^{60}$  sources. A correction of 2.1% was applied to take into account the self-shielding of the cobalt wire (Jervis 1957). The reactor cross section of  $\text{Co}^{59}$  was calculated to be 36.6 barns, taking 36.0 barns (Hughes and Harvey 1955) for its thermal neutron capture cross section and 5.20 years (Lockett and Thomas 1956) for the half-life of  $\text{Co}^{60}$ .

The irradiations of the samples were interrupted a number of times by reactor shutdowns. The amounts of  $\text{Sr}^{89}$  and  $\text{Sr}^{90}$  formed have been corrected accordingly (correction was about 5%).

Fig. 2 shows the variation of  $\text{Y}^{90}$  activity per gram of irradiated  $\text{Sr}^{88}$  normalized to the same irradiation time as a function of the square of the neutron flux. The linear relationship observed is consistent with a successive neutron capture process.

By solving equation (1), the cross section of  $\text{Sr}^{89}$  was obtained for each separation, the average being  $0.49 \pm 0.10$  barn. The probable error of the mean of the measured values in Table I is 2%, but the deviation quoted is an estimated error which takes into account the uncertainties involved in the values used in the calculations, the main one being the cross section of  $\text{Sr}^{88}$ , which is not known to any better than 20%. The cross section refers to reactor spectrum neutrons, since no experiment was done to determine the epicadmium contribution.

Obviously  $\text{Sr}^{89}$  with a cross section of 0.49 barn cannot be considered as a potential reactor poison, nor can it contribute appreciably to the formation of  $\text{Sr}^{90}$  in nuclear reactor fuels.

#### REFERENCES

- FLYNN, K. F., GLENDENIN, L. E., and STEINBERG, E. P. 1955. *Phys. Rev.* **98**, 1327.  
HUGHES, D. J. and HARVEY, J. A. 1955. Brookhaven National Laboratory Report, BNL-325.  
JERVIS, R. E. 1957. Unpublished results.  
JOHNSON, O. E., JOHNSON, R. G., and LANGER, L. M. 1955. *Phys. Rev.* **98**, 1517.  
KATCOFF, S. 1951a. National Nuclear Energy Series, Div. IV, Vol. 9 (McGraw-Hill Book Co., Inc., New York), Paper 224.  
——— 1951b. National Nuclear Energy Series, Div. IV, Vol. 9 (McGraw-Hill Book Co., Inc., New York), Paper 220.  
KJELBERG, A. and PAPPAS, A. 1956. *Nuclear Physics*, **1**, 322.  
LOCKETT, E. E. and THOMAS, R. H. 1956. *Nucleonics*, **14** (11), 127.  
MILTON, G. M. and GRUMMITT, W. E. 1957. Atomic Energy of Canada Limited Report, CRC-688.  
WILES, D. M. and TOMLINSON, R. H. 1955. *Can. J. Phys.* **33**, 133.

# ISOTOPE SHIFT IN THE RESONANCE LINES OF Mg I<sup>1</sup>

F. M. KELLY

## ABSTRACT

Measurements of the isotope shift in  $\lambda 2852$  ( $3^1S_0-3^1P_1$ ) and  $\lambda 4571$  ( $3^1S_0-3^3P_1$ ) of Mg I are reported. The new measurements are compared with other results and with theoretical calculations.

## INTRODUCTION

Measurements of the isotope shift in the Mg I singlet resonance line  $\lambda 2852$  ( $3s^2^1S_0-3s3p^1P_1$ ) were first reported by Jackson and Kuhn (1936), who used an atomic beam in absorption. Fisher (1942) employed an atomic beam excited by electron bombardment, while Murakawa (1953) used a hollow cathode in which magnesium appeared as an impurity. The results are summarized in Table I.

The isotope shift in the intercombination resonance line  $\lambda 4571$  ( $3s^2^1S_0-3s3p^3P_1$ ) has been measured using a hollow cathode source by Murakawa (1935 and 1953) and Backer and Sawyer (1935). These results are also summarized in Table I.

TABLE I  
MEASURED ISOTOPE SHIFT ( $\text{cm}^{-1}$ )

	24	25	26
In $\lambda 2852$			
Jackson and Kuhn (1936)	0	—	0.033
Fisher (1942)	0	0.030	0.053
Murakawa (1953)	0	(0.0305)	0.061
Kelly (1957)	0	0.0229	0.0461
In $\lambda 4571$			
Murakawa (1935)	0	0.037	0.102
Backer and Sawyer (1935)	0	—	0.083
Murakawa (1953)	0	—	0.093
Kelly (1957)	0	—	0.0828

The determination of the isotope shift in the resonance lines is of importance because it connects the extensive measurements of shifts in the singlet terms of Mg I by Mundie and Meissner (1944) with the shifts in the triplet levels and also permits a simple comparison with theoretical calculations. Table I shows that discrepancies exist in the previous experimental measurements.

## RESULTS

During a set of experiments with an atomic beam source, reported previously (Crawford *et al.* 1949), long exposures were required to record the structure in the Mg II resonance lines. To check the adjustments of the optical system it was convenient to make exposures of a few minutes' duration on  $\lambda 2852$ . Patterns were recorded with 4 cm. and 5 cm. etalons. A weak

<sup>1</sup>Manuscript received June 24, 1957.

Contribution from the Department of Physics, University of Manitoba, Winnipeg, Manitoba.



component due to  $\text{Mg}^{25}$  and another due to  $\text{Mg}^{26}$  were clearly resolved from a strong component due to  $\text{Mg}^{24}$ . Visual estimates of intensity agreed with the relative abundances of these three isotopes (White and Cameron 1948), which are in the approximate ratio 79:10:11. Four such spectrograms have now been measured and yield the following results:

$$\Delta\nu(24, 25) = 0.0229 \pm .0002 \text{ cm}^{-1},$$

$$\Delta\nu(24, 26) = 0.0461 \pm .0009 \text{ cm}^{-1}.$$

The errors quoted are the average deviation from the mean. In accord with the predictions of the mass effect, the heavier isotopes have the higher frequency and  $\Delta\nu(24, 26)$  is twice  $\Delta\nu(24, 25)$ . The measurements made by Fisher (1942) do not show that the splittings are proportional to the change in mass, and Murakawa (1953) indicates that his measurement of  $\Delta\nu(24, 25)$  is in some doubt.

The discrepancies in the previous isotope shift measurements of the intercombination resonance line ( $\lambda 4571$ ) make a re-examination of this line desirable. This line is very weak in an atomic beam source which uses electron excitation. In the experiments reported here, a magnesium hollow cathode cooled by liquid nitrogen was used, with neon as the carrier gas. When the pressure of the neon was reduced to near the limit where the discharge would not stay in the hollow cathode, the intensities of neon lines close to  $\lambda 4571$  were sufficiently reduced so that they did not affect measurements. The Fabry-Perot interferometer with a 3 cm. spacer was mounted in front of the slit of a small Hilger constant deviation spectrograph. Discharge currents of 40, 20, 15, and 10 ma. were employed. With the 40 ma. current the structure was poorly resolved and the plates were not measured. Five spectrograms with about seven orders each for both 20 and 15 ma. currents, and four spectrograms for the 10 ma. current were measured. The results are given in Table II.

TABLE II  
ISOTOPE SHIFT IN  $\lambda 4571$

Discharge current, ma.	24	25	26
20	0	—	$0.0853 \pm 0.0003$
15	0	—	$0.0827 \pm 0.0004$
10	0	—	$0.0830 \pm 0.0009$

The 20 ma. exposures give results which are slightly higher than those obtained with 15 and 10 ma. The 15 and 10 ma. exposures are not significantly different, and the average result of all these exposures,  $\Delta\nu(24, 26) = 0.0828 \pm .0007 \text{ cm}^{-1}$ , is accepted as the best result. The errors given are the average deviation from the mean. This result is in agreement with the measurements of Backer and Sawyer (1935). We find that higher currents lead to a larger apparent isotope shift. Murakawa (1953) used a 40 ma. current and this may explain his larger value. One expects the best source conditions with lowest currents.

On some of the better spectrograms for  $\lambda 4571$  there were indications of components due to  $\text{Mg}^{25}$ . However, the radiation from  $\text{Mg}^{25}$  is expected to be split into three components, due to magnetic hyperfine structure. The calculated Doppler width of the radiation from this source is  $0.03 \text{ cm}^{-1}$  so that the magnetic structure cannot be resolved. In order to see if this unresolved structure would influence the observed position of the component due to  $\text{Mg}^{26}$  relative to  $\text{Mg}^{24}$ , patterns were plotted using theoretical intensities and with the centroid of the  $\text{Mg}^{25}$  components midway between  $\text{Mg}^{24}$  and  $\text{Mg}^{26}$ . It was found that the influence of  $\text{Mg}^{25}$  was small enough to be neglected.

The isotope shifts between  $\text{Mg}^{24}$  and  $\text{Mg}^{26}$  in the singlet and intercombination resonance lines may be analyzed in a manner similar to that used for the Zn I resonance lines (Crawford *et al.* 1950).

TABLE III  
ISOTOPE SHIFT IN Mg I ( $\text{cm}^{-1}$ )

	2852	4571
Observed shift	+0.046	+0.083
Normal shift	+0.061	+0.038
Residual shift	-0.015	+0.045
Calculated specific shift	-0.009	+0.012

Table III shows the observed shifts, the calculated normal mass shift, and the residual shift obtained by subtracting the normal from the observed shift. Since the field effect (Rosenthal and Breit 1932) is negligible for Mg, the residual shifts are due to the specific mass effect. The specific mass shifts have been calculated by Vinti (1939). They agree in sign but not in magnitude with the measured residual shifts. The difference in residual shifts ( $0.060 \text{ cm}^{-1}$ ) has the sign predicted by the specific mass theory. This difference corresponds to the single specific mass integral  $C(3p, 3s)$  in the notation of Bartlett and Gibbons (1933). Vinti (1939) does not report a direct calculation of this single integral but its calculated magnitude is about  $+0.021 \text{ cm}^{-1}$  obtained by subtracting the calculated shifts for the two lines. Again, the theoretical and observed magnitudes do not agree.

#### REFERENCES

- BACKER, R. F. and SAWYER, R. A. 1935. *Phys. Rev.* **47**, 587.  
 BARTLETT, J. H. and GIBBONS, J. J. 1933. *Phys. Rev.* **44**, 538.  
 CRAWFORD, M. F., GRAY, W. M., KELLY, F. M., and SCHAWLOW, A. L. 1950. *Can. J. Research, A*, **28**, 138.  
 CRAWFORD, M. F., KELLY, F. M., SCHAWLOW, A. L., and GRAY, W. M. 1949. *Phys. Rev.* **76**, 1527.  
 FISHER, R. A. 1942. *Revs. Modern Phys.* **14**, 79.  
 JACKSON, D. A. and KUHN, H. 1936. *Proc. Roy. Soc. A*, **154**, 679.  
 MUNDIE, L. G. and MEISSNER, K. W. 1944. *Phys. Rev.* **65**, 265.  
 MURAKAWA, K. 1935. *Proc. Phys.-Math. Soc. Japan*, **17**, 14.  
 ——— 1953. *J. Phys. Soc. Japan*, **8**, 213.  
 ROSENTHAL, J. E. and BREIT, G. 1932. *Phys. Rev.* **41**, 459.  
 VINTI, J. P. 1939. *Phys. Rev.* **56**, 1120.  
 WHITE, J. R. and CAMERON, A. E. 1948. *Phys. Rev.* **74**, 991.

# GROWTH CONDITIONS FOR STABILITY OF A CELLULAR SOLID-LIQUID INTERFACE<sup>1</sup>

E. L. HOLMES, J. W. RUTTER, AND W. C. WINEGARD

## ABSTRACT

Samples of zone-refined lead containing various amounts of silver as solute were solidified under well-controlled conditions to study the transition from cellular to dendritic freezing as a function of composition, speed of freezing, temperature gradient in the melt during freezing, and crystallographic orientation of the solidifying crystal. A comparison of the results of this investigation with those of Tiller and Rutter (1956) on alloys of tin in lead shows that to a first approximation the onset of dendritic freezing under any given growth conditions occurs at a critical value of the average solute concentration in the liquid at the solid-liquid interface, independent of whether the solute present is tin or silver.

## INTRODUCTION

Much effort has been expended in the past few years in investigating the various phenomena observed to occur during the solidification of metals and alloys. The work described in this paper was carried out in an attempt to extend the available knowledge of the conditions under which cellular and dendritic freezing occur in binary alloys.

The work of Rutter and Chalmers (1953), Tiller *et al.* (1953), Walton *et al.* (1955), and Tiller and Rutter (1956) has established the effect of growth conditions such as the rate of solidification  $R$ , the temperature gradient in the liquid  $G$ , and the solute concentration  $C_0$  upon the formation of the cellular substructure during solidification. The effect of these same growth conditions on the formation of dendrites has been discussed by Winegard and Chalmers (1953) and determined experimentally by Morris *et al.* (1955) and Tiller and Rutter (1956). Tiller and Rutter found that the conditions corresponding to the onset of dendritic freezing are dependent upon the crystallographic orientation of the solidifying crystal with respect to the direction of freezing; for a given  $G$  and  $R$ , higher impurity concentrations are necessary to cause dendritic freezing in crystals growing in an orientation close to the dendrite direction than for crystals growing in orientations farther from the dendrite direction. Their results indicate that for alloys of tin as a solute in lead, the upper and lower limits of this orientation range are straight lines when the critical freezing conditions are plotted as concentration vs.  $G/R^{1/2}$  (see Fig. 1).

Tiller and Rutter studied the onset of dendritic freezing in alloys of tin in lead only. It was felt, therefore, that another binary system should be investigated in the hope that a comparison of the results would yield useful information.

## EXPERIMENTAL TECHNIQUES

The "thermal value" technique, as described by Tiller and Rutter (1956),

<sup>1</sup>Manuscript received May 27, 1957.

Contribution from the Department of Metallurgical Engineering, University of Toronto, Toronto, Ont.

was used to grow specimens composed of a small number of crystals under a range of growth rates from 0.2 to 1.2 cm. per minute, and under a range of temperature gradients in the liquid from  $2^{\circ}\text{C.}$  to  $10^{\circ}\text{C.}$  per cm. The alloys were prepared by adding known amounts of electrolytically-refined silver to zone-refined lead. The structure of the solid-liquid interface at any time was obtained by decanting the liquid, as described by Elbaum and Chalmers (1955).

#### EXPERIMENTAL OBSERVATIONS

Microscopic examination of the interfaces produced showed that the transition from cellular to dendritic freezing in alloys of silver in lead occurs in essentially the same way as it does in alloys of tin in lead, but at a much lower solute concentration in the melt. The interfaces obtained appeared very similar to those observed by Tiller and Rutter (1956).

The experimental results obtained are tabulated in Table I and plotted in Fig. 1 in the form  $C_0$  vs.  $G/R^{1/2}$ .

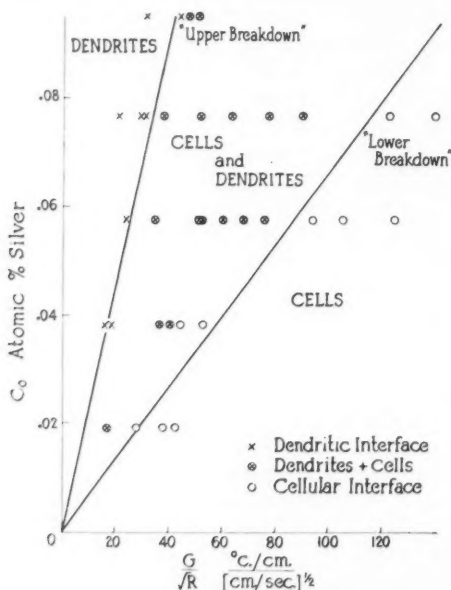


FIG. 1. Cell to dendrite transition—silver as solute in lead.

For any given solute concentration, a lower value of  $G/R^{1/2}$  is required to cause dendritic freezing in a crystal which is growing in a direction close to the dendrite direction [100] than for a crystal growing in a direction farther from the dendrite orientation. The limits of this orientation-dependent range are shown in Fig. 1. They appear as straight lines in the  $C_0$  vs.  $G/R^{1/2}$  plot and

TABLE I

Atomic % silver	Growth rate $R$ , cm./sec. $\times 10^{-3}$	Temperature gradient $G$ , $^{\circ}$ C./cm.	$G/R^{\frac{1}{2}}$ , $^{\circ}$ C./cm. (cm./sec.) $^{\frac{1}{2}}$	Interface appearance
0.019	18.3	3.60	26.50	Cells, but slight beginnings of side branching on one crystal
	23.3	2.55	17.43	Cells, but one region broken down completely
0.038	13.3	4.50	39.18	Cells
	11.6	4.67	43.00	Cells
	9.2	4.90	51.11	Cells
	8.7	3.95	42.60	Cells with a few appearing with bowed sides
	15.0	4.75	39.00	Cells with one region developing side branches
	16.7	4.62	35.80	Cells with one region completely broken down
	18.3	2.60	19.22	Dendrites with one region of unstable cells
	13.7	2.10	18.00	Dendrites with one region of unstable cells
0.057	9.2	4.64	48.64	Cells and dendrites
	15.0	6.00	49.00	Cells and dendrites
	15.0	6.10	49.80	Cells and dendrites
	13.3	4.12	35.78	Dendrites, one region of cells
	8.3	5.52	60.50	Cells, one region completely broken down
	6.5	3.29	68.10	Cells, one region completely broken down
	5.4	5.53	75.20	Cells, one region with side branching
	3.3	6.12	106.5	Cells
	3.7	5.58	93.2	Cells with a few appearing with bowed sides
	15.0	3.60	29.10	Dendrites, one region of unstable cells
0.076	20.0	3.60	25.18	Dendrites, one region of unstable cells
	5.0	9.00	124.0	Cells
	11.7	2.20	20.55	Dendrites
	10.0	3.60	36.00	Dendrites, one region of cells
	11.7	2.20	20.55	Dendrites
	5.0	10.0	139.00	Cells
	13.3	7.30	63.50	Cells, dendrites
	9.2	3.20	33.27	Dendrites, one region of very unstable cells
	8.3	4.68	51.20	Cells, dendrites
	9.2	3.27	34.20	Dendrites, one region of cells with beginnings of side branching
	12.5	3.58	31.95	Dendrites
	13.3	7.30	63.20	Cells, dendrites
0.095	5.0	6.36	89.80	Cells, irregular, some with bowed sides
	5.0	5.45	77.50	Similar to above with side branching
	5.7	9.24	122.0	Cells, irregular, some with bowed sides
	16.7	5.55	43.00	Dendrites, last region of cells breaking down
	16.7	4.00	31.00	Dendrites
	9.7	4.86	49.60	Cells and dendrites
	8.0	4.18	46.90	Cells and dendrites

are marked "upper breakdown" and "lower breakdown" corresponding, respectively, to a crystal growing in the dendrite direction and a crystal growing in a direction far from the dendrite orientation. A sample consisting of several grains will, therefore, generally show some dendritic and some cellular grains when freezing in the orientation-dependent range.

## DISCUSSION

A comparison of the observations made in this investigation with those of Tiller and Rutter shows the following qualitative features:

(1) The microscopic appearance of the solid-liquid interface during the transition from cellular to dendritic freezing for lead-silver alloys is similar to that for lead-tin alloys.

(2) Lead-silver alloys show an orientation dependence of the cell to dendrite transition qualitatively similar to that for lead-tin alloys.

(3) A plot of  $C_0$  vs.  $G/R^{1/2}$  gives straight lines for the upper and lower breakdown limits for both alloys.

A quantitative comparison with the work of Tiller and Rutter can be made by plotting both sets of experimental data on the same scale. While the starting concentrations in the melt were quite different in the two investigations, the liquid in the neighborhood of the solid-liquid interface would be enriched in solute content in proportion to the distribution coefficient,  $k$ , of the solute present, so that the average solute concentration in the liquid at the interface would be  $C_0/k$ . Since it is this enriched liquid from which the solid forms, it was felt that the two sets of experimental results should be compared on the basis of the average solute concentration at the interface. The data are plotted in Fig. 2 as  $C_0/k$  in atomic per cent vs.  $G/R^{1/2}$ . The following distribution coefficients were used to calculate the  $C_0/k$  values:

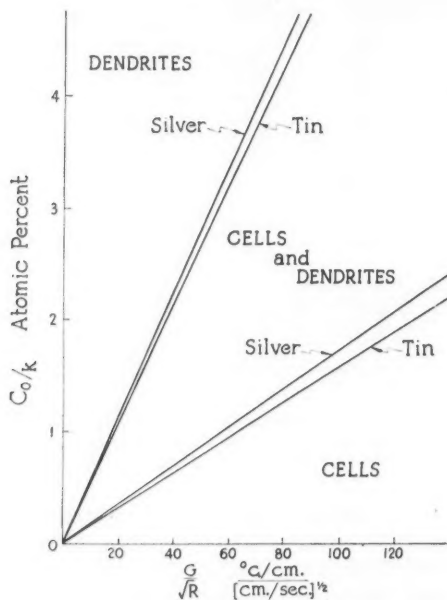


FIG. 2. Comparison of results for tin and silver as solutes in lead.

for silver in lead:  $k_{Ag} = 0.04$ ,

for tin in lead:  $k_{Sn} = 0.57$ .

It will be seen from Fig. 2 that to a good approximation and, in fact, within the experimental error to be anticipated, the two upper breakdown lines coincide and the two lower breakdown lines coincide. Therefore, for any given conditions of freezing as defined by  $G/R^{\frac{1}{2}}$  the melt concentration,  $C_0(\text{Sn})$ , of tin required to produce a given effect is related to the concentration,  $C_0(\text{Ag})$ , of silver required to produce the same effect by the equation:

$$k(\text{Sn}) C_0(\text{Ag}) = k(\text{Ag}) C_0(\text{Sn}),$$

where  $k(\text{Sn})$  and  $k(\text{Ag})$  are the distribution coefficients for tin and silver respectively. In other words, for given growth conditions, as expressed by any selected value of  $G/R^{\frac{1}{2}}$ , the transition from cellular to dendritic freezing occurs to a first approximation for the same critical average solute concentration at the interface, regardless of whether the solute is tin or silver.

It is clear that more experimental work is required before any generalization can be made from these results. It is interesting to speculate, however, that perhaps the average solute concentration at the solid-liquid interface, independent of the particular solute present, is the important factor in determining the onset of dendritic freezing under given growth conditions.

#### REFERENCES

- ELBAUM, C. and CHALMERS, B. 1955. *Can. J. Phys.* **33**, 196.  
MORRIS, W., TILLER, W. A., RUTTER, J. W., and WINEGARD, W. C. 1955. *Trans. Am. Soc. Metals*, **47**, 463.  
RUTTER, J. W. and CHALMERS, B. 1953. *Can. J. Phys.* **31**, 15.  
TILLER, W. A., JACKSON, K. A., RUTTER, J. W., and CHALMERS, B. 1953. *Acta Met.* **1**, 428.  
TILLER, W. A. and RUTTER, J. W. 1956. *Can. J. Phys.* **34**, 96.  
WALTON, D., TILLER, W. A., RUTTER, J. W., and WINEGARD, W. C. 1955. *Trans. Am. Inst. Mining Met. Engrs.* **203**, 1023.  
WINEGARD, W. C. and CHALMERS, B. 1953. *Trans. Am. Soc. Metals*, **46**, 1214.

# THE CONSTITUTION OF NICKEL-GALLIUM ALLOYS IN THE REGION 0-35 ATOMIC % GALLIUM<sup>1</sup>

W. B. PEARSON AND D. M. RIMEK

## ABSTRACT

The equilibrium diagram of nickel-gallium alloys has been revised to include a newly discovered  $\text{Ni}_3\text{Ga}$  superlattice which forms peritectically at  $1210^\circ\text{C}$ . The new work shows that there is a very close resemblance between the Ni-Al and Ni-Ga systems in the nickel-rich region.

## INTRODUCTION

Hellner (1950a) examined Ni-Ga alloys by thermal analysis and microscopical and X-ray methods determining the equilibrium diagram, a part of which is shown in Fig. 1. According to his findings the terminal nickel solid

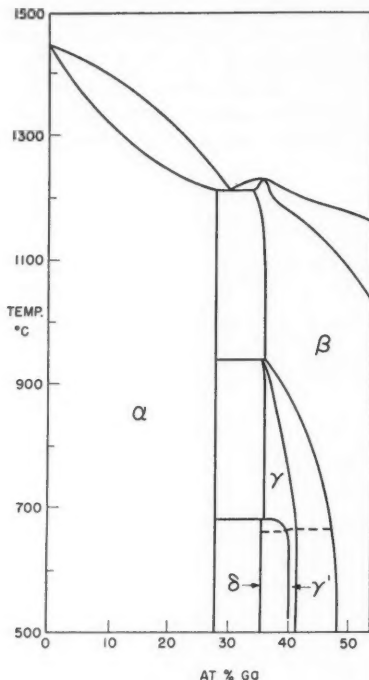


FIG. 1. Part of Ni-Ga equilibrium diagram, after Hellner (1950a).

<sup>1</sup>Manuscript received June 21, 1957.

Contribution from the Division of Pure Physics, National Research Council, Ottawa, Canada.

Issued as N.R.C. No. 4486.



solution extended to 28 at. % Ga; however, Pearson (1954) measuring the lattice spacings of the solid solution found a superlattice of the  $\text{Cu}_3\text{Au}$  type at  $\text{Ni}_3\text{Ga}$ . Further constitutional studies in this region have now been carried out and the results provide an amended equilibrium diagram which includes the  $\text{Ni}_3\text{Ga}$  phase.

#### EXPERIMENTAL METHODS

Alloys were prepared by melting Mond nickel shot (0.02% C, 0.02% Fe) and 99.9+ % Ga together *in vacuo* in alumina crucibles using inductive heating. We are indebted to the International Nickel Co. Inc. for the supply of nickel shot. The gallium was obtained either from Johnson, Matthey & Co. Ltd. or from MacKay Inc., New York. The alloys were homogenized for from 3 to 7 days at 1100° C. For this treatment they were annealed in alumina collars sealed in evacuated silica tubes. The isothermal annealing times for bulk alloys varied from 30 minutes in the vicinity of the solidus to 60 days at 600° C. Powders for X-ray analysis were prepared from annealed lumps, cleaned of iron by means of a magnet,\* washed, dried, and reannealed and quenched from the same temperature at which the lumps were first annealed.

Debye-Scherrer X-ray photographs were taken in a 19 cm. diameter Unicam camera. Lattice spacings, calculated using the Nelson-Riley extrapolation method, have a relative accuracy of 0.0001 kX as regards the X-ray measurements, although other factors such as alloy purity and chemical analysis considerably increase the relative error on a lattice spacing - composition plot.

The phase equilibria have been determined from microscopical examination of quenched alloys at high temperatures up to the solidus, while at lower temperatures increasing reliance has been placed on the results of X-ray measurements. The composition of all of the important alloys in the microscopic work has been obtained by chemical analysis of both components and sometimes of the impurities present also. In the X-ray work the composition of homogeneous samples and some heterogeneous samples has been determined by chemical analysis of the actual X-ray powders for nickel, gallium, and also for iron.

Temperatures were measured with calibrated platinum-platinum/10% rhodium thermocouples and should generally be accurate to  $\pm 3^\circ \text{C}$ .

#### EXPERIMENTAL RESULTS

Fig. 2 shows the amended equilibrium diagram up to 35 at. % Ga as determined from this work and Fig. 3 shows in more detail the high temperature region where  $\text{Ni}_3\text{Ga}$  forms peritectically at 1210° C. The limiting solid solubility of gallium in nickel is 24.3 at. % at the peritectic temperature. The peritectic is followed by a eutectic at 1204° C., the limits of the  $\alpha'$  and  $\beta$  phases being about 25.7% and 30.4 at. % Ga at the eutectic temperature.

\*If the alloys were ferromagnetic at room temperature it was necessary to heat the powder *in vacuo* to a temperature above its Curie point in order to separate the iron magnetically.

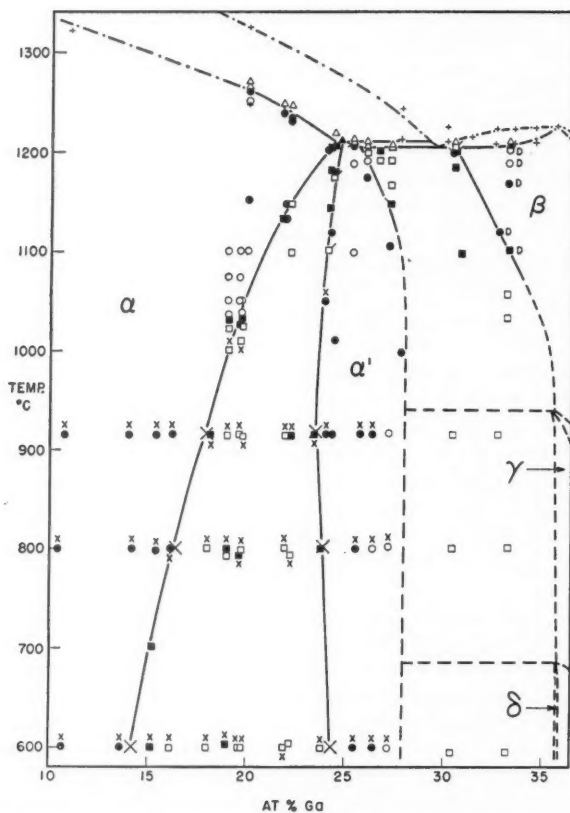


FIG. 2. Revised Ni-Ga equilibrium diagram up to 35 at. % Ga.

- single-phase alloys
  - two-phase alloys
  - ▲ alloys showing partial melting
  - single-phase alloys
  - two-phase alloys
  - △ alloys showing partial melting
- } chemically analyzed
- } not chemically analyzed
- x by the alloy symbol means that the alloy was examined also by means of X-rays.
- D by the alloy symbol means that the alloy was homogeneous at the annealing temperature, but decomposed on quenching.
- x phase boundaries determined from lattice spacing curves.
- + liquidus and solidus points from the work of Hellner (1950a).
- boundaries established in the present work.
- - - boundaries established by Hellner (1950a).
- · - · - boundaries obtained from a combination of the work of Hellner and the present work.

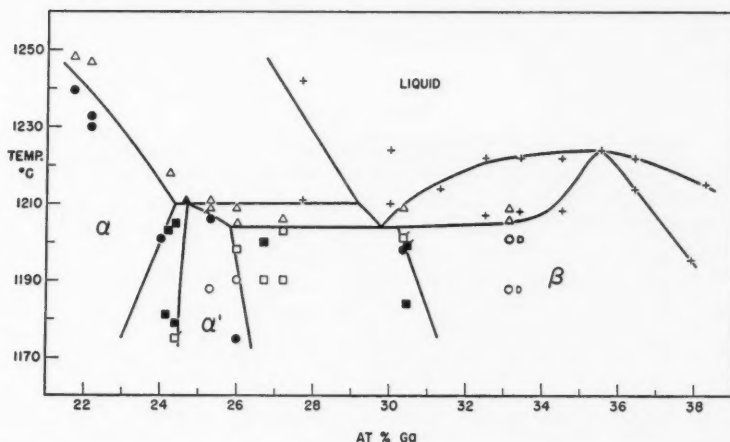


Fig. 3. Detail of Ni-Ga equilibrium diagram at high temperatures. For symbols see caption to Fig. 2.

There is very little doubt that the  $\alpha'$ -Ni<sub>3</sub>Ga phase does actually extend up to the solidus. Alloys 24.2 and 24.4,\* quenched from 1203° and 1205° C. respectively, are very distinctly heterogeneous (Fig. 4), while alloy 25.3 quenched from 1206° C. is homogeneous and alloy 26.0 quenched from 1205° shows partial melting.

Fig. 5 shows the greatly decreased quantity of the  $\alpha$  phase in alloy 24.4 on annealing and quenching from 1178° C. This results from the relative slopes of the boundaries of the  $(\alpha + \alpha')$  field (Fig. 3).

There is nothing remarkable about the microstructure of the quenched homogeneous  $\alpha'$  phase, but nickel-rich samples of the  $\beta$  phase quenched from high temperatures show a characteristic decomposed structure due to the formation of the  $\gamma$  phase on cooling. This leads to striking microstructures of heterogeneous alloys in the  $(\alpha' + \beta)$  field (Fig. 6). In alloys annealed at 915° C. below the  $\beta \rightarrow \gamma$  transformation temperature this decomposition is no longer apparent, and Fig. 7 shows the microstructure developed in alloy 32.7 by homogenizing it in the vicinity of 1100° C. and then annealing it at 915° C. The clear areas represent particles of the  $\alpha'$  phase which were present at 1100° C. In the area showing fine structure the matrix is the  $\gamma$  phase and the precipitate is the  $\alpha'$  phase formed as a result of the sloping  $(\alpha' + \beta)/\beta$  phase boundary between 1100° and 940° C.

Figs. 8 and 9 show the lattice spacing variation in the  $\alpha$  and  $\alpha'$  fields together with parameters of alloys quenched from three temperatures in the  $(\alpha + \alpha')$  field. The  $\alpha$  and  $\alpha'$  phase boundaries obtained from these diagrams agree well with the results of microscopical examinations (Fig. 2). Most of the alloys were also examined by X-rays in order to determine the phases

\*The alloys are described by their composition in at. % Ga.

present after annealing at 915°, 800°, and 600° C. The results of this examination, shown in Fig. 2, were in good agreement with the microstructures of the bulk alloys.

#### DISCUSSION

In the solid state the boundaries which we find for the ( $\alpha' + \beta$ ) field agree well with the observations of Hellner for his ( $\alpha + \beta$ ) field, and the eutectic and solidus temperatures are in fair agreement (his solidus temperature measurements are quite consistent with a maximum solid solubility of 24.3 at. % Ga in Ni).

The liquidus temperatures of Hellner disagree with our findings only in respect of his alloy containing 30 at. % Ga, which was used to locate the eutectic point at 31 at. % Ga. The present work and that of Hellner can best be reconciled by assuming the eutectic point to lie at 29.5 at. % Ga (Figs. 2 and 3).

The one surprising feature in the equilibrium diagram shown in Fig. 2 is the retrograde solubility of nickel in the  $\alpha'$  phase at temperatures below about 1000° C., which suggests the possibility of a transition in the  $\alpha'$  phase in this region. However, normal and differential cooling curves on a homogeneous  $\alpha'$  alloy revealed no very definite evidence for this, although in several experiments there was a suggestion of a thermal effect in the region of 1080° C.\* Similarly, thermoelectric measurements of a Pt/Ni<sub>3</sub>Ga couple gave no obvious evidence for a transition in this temperature region.

The discovery of a Ni<sub>3</sub>Ga superlattice makes a comparison of the Ni-Al and Ni-Ga systems rather interesting. In the Ni-Al system there has been some argument in the past as to whether the ordered Ni<sub>3</sub>Al phase forms by a solid state reaction (Bradley and Taylor 1937) or forms peritectically (Schramm 1941), but it is now accepted that it forms peritectically at 1362° C. (cf. Taylor and Floyd 1952; Smithells 1955). In the Ni-Ga system it is certain that the Ni<sub>3</sub>Ga phase also forms peritectically, so that the arrangement of peritectic and eutectic reactions and also a suggestion of retrograde solubility of Ni in Ni<sub>3</sub>Al at low temperatures makes the two systems very similar to each other in this region.

In the Ni-In system the Ni solid solution is more restricted, extending only to 14 at. % In at high temperatures (Hellner 1950*b*), and the phase found at Ni<sub>3</sub>In has an ordered hexagonal DO<sub>19</sub>† type of structure, which is a superlattice of the close packed hexagonal structure. The change to hexagonal close packing is interesting since the c.p. hexagonal structure is capable of accommodating the relatively large indium atoms merely by an adjustment of the axial ratio, rather than by a loss of crystal symmetry, which would probably occur if the ordered structure was based on cubic close packing.

#### ACKNOWLEDGMENTS

We wish to thank Mr. W. Stockdale for carrying out the chemical analyses

\*The amount of alloy which was available for this examination was unfortunately not as great as we would have liked. The preparation of a 50 or 100 g. ingot was impossible owing to the cost of the gallium.

†Strukturbericht type of structure.

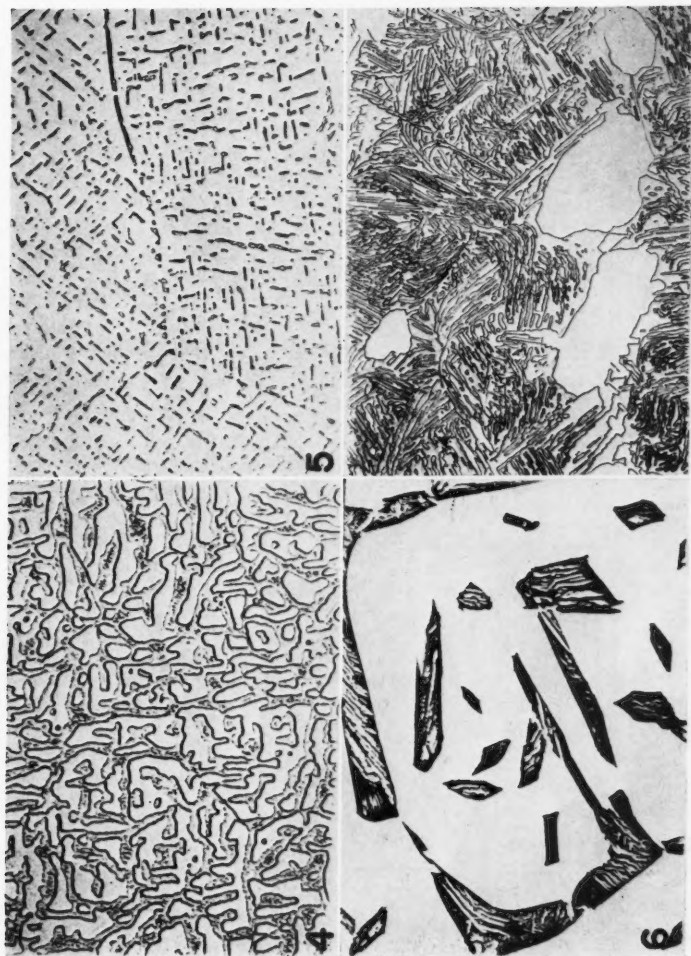


FIG. 4. Alloy 24.4 quenched from 1205° C.  
 FIG. 5. Alloy 24.4 quenched from 1178° C.  
 FIG. 6. Alloy 27.2 quenched from 1190° C.  
 FIG. 7. Alloy 32.7 homogenized at 1100° C. and then annealed at 915° C.  $\alpha$  and  $\gamma$  phases, X95, see text.



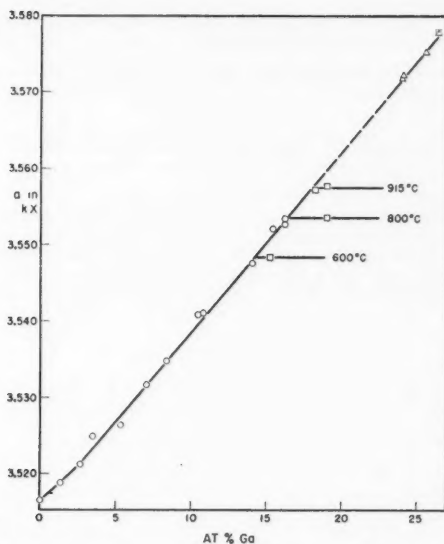


FIG. 8. Lattice spacing variation in the  $\alpha$  nickel solid solution.  
 ○ single-phase alloys.  
 □ two-phase alloys quenched from the temperatures indicated.  
 △ single-phase alloys in the  $\alpha'$  field.

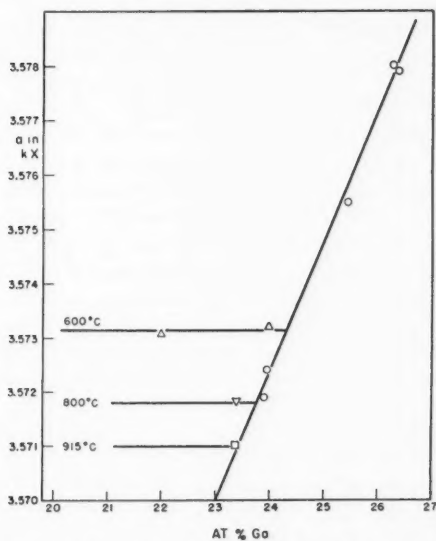


FIG. 9. Lattice spacing variation in the  $\alpha'$ -Ni<sub>3</sub>Ga field.  
 ○ single-phase alloys.  
 △ ▽ □ two-phase alloys quenched from the temperature indicated.

and Mrs. L. T. Thompson for obtaining much of the X-ray data. The lattice spacings of the homogeneous  $\alpha$  solid solution used in the present work have already been published by Pearson and Thompson (1957).

#### REFERENCES

- BRADLEY, A. J. and TAYLOR, A. 1937. Proc. Roy. Soc. A, **159**, 56.  
HELLNER, E. 1950a. Z. Metallk. **41**, 480.  
——— 1950b. Z. Metallk. **41**, 401.  
PEARSON, W. B. 1954. Nature, **173**, 364.  
PEARSON, W. B. and THOMPSON, L. T. 1957. Can. J. Phys. **35**, 349.  
SCHRAMM, J. 1941. Z. Metallk. **33**, 347.  
SMITHELS, C. J. 1955. Metals reference book, 2nd ed. (Butterworth Scientific Publications, London).  
TAYLOR, A. and FLOYD, R. W. 1952. J. Inst. Metals, **81**, 25.



# VIBRATION-ROTATION BANDS OF AMMONIA

## II. THE MOLECULAR DIMENSIONS AND HARMONIC FREQUENCIES OF AMMONIA AND DEUTERATED AMMONIA<sup>1</sup>

W. S. BENEDICT<sup>2</sup> AND EARLE K. PLYLER<sup>3</sup>

### ABSTRACT

A summary is given of molecular constants for  $\text{NH}_3$  and  $\text{ND}_3$ , as derived from high-resolution infrared spectra of a number of fundamental, overtone, and combination bands. Preliminary estimates are given for the equilibrium moments of inertia, the molecular dimensions, and the force constants of the harmonic potential function. The average molecular dimensions in the equilibrium configuration are  $r_e = 1.011_6 \times 10^{-8}$  cm.,  $h_e = 0.381_6 \times 10^{-8}$  cm.

### INTRODUCTION

We have been engaged for some time in a study of rotational fine structure in a number of vibrational bands of  $\text{NH}_3$  and  $\text{ND}_3$ . As described in some detail in the first paper of this series (Benedict, Plyler, and Tidwell 1957) our ultimate aim is to obtain the constants describing the rotation-vibration-inversion interactions in a large number of levels, so that one may extrapolate from the ground level to the equilibrium configuration, and thus obtain definitive values of the equilibrium dimensions and the frequencies of infinitesimal vibration. From these data one may derive, on the conventional theory of the vibration-rotation energies of molecules (cf. Nielsen 1951), the harmonic and anharmonic potential constants.

Our first paper described our general methods of procedure and presented detailed results in one region of the  $\text{NH}_3$  spectrum, that of the combination bands ( $\nu_2 + \nu_1$ ,  $\nu_2 + \nu_3$ ) from 4100 to 4700  $\text{cm}^{-1}$ , where an essentially complete identification of the observed structure was achieved. We have now obtained spectra of both  $\text{NH}_3$  and  $\text{ND}_3$  over the range 1750 to 7100  $\text{cm}^{-1}$  with an effective resolution of 0.1–0.2  $\text{cm}^{-1}$ . In most of the regions of absorption it has been possible to analyze the basic structure, but in many cases there are complicating interactions. It would seem desirable, before presenting the details of the spectra in other specific regions, to give a general resume of the results to date. Although our final goal of a complete understanding of the ammonia spectrum has not been attained, it has been possible to obtain values for the equilibrium dimensions and harmonic potential constants that are a considerable refinement over published results (cf. Dennison 1940, and Herzberg 1945). These are given in the present paper, together with a summary of the more important band constants which lead to them. The present

<sup>1</sup>Manuscript received June 26, 1957.

Contribution from the Laboratory of Astrophysics and Physical Meteorology, The Johns Hopkins University, Baltimore, Maryland, and the National Bureau of Standards, Washington, D.C.

Work supported by The Office of Scientific Research U.S. Air Force under Contract No. AF 18(600)-1557, and by The Atomic Energy Commission. Reproduction in whole or in part for any purpose of the U.S. Government is permitted.

<sup>2</sup>The Laboratory of Astrophysics and Physical Meteorology, The Johns Hopkins University.

<sup>3</sup>The National Bureau of Standards.

results should permit further improvements in the analyses of the observed regions, which in turn may lead to better values for the constants.

#### DESCRIPTION OF SPECTRA AND BAND CONSTANTS

The analyzed regions include both parallel and perpendicular bands. In situations where both types of bands might be expected, for example in the region of the first harmonic of the N-H stretching frequencies, where two parallel ( $2\nu_1$ ,  $2\nu_3^0$ ) and two perpendicular ( $\nu_1 + \nu_3^1$ ,  $2\nu_3^2$ ) components are theoretically possible, it appears to be a general rule that the perpendicular bands predominate in intensity. In the above-mentioned case, the parallel components have not yet been located. There is one exception to this rule: in  $\text{NH}_3$ , in the region  $2400$  to  $2700\text{ cm}^{-1}$ , where previous low-resolution studies showed bands that were interpreted either (Barker 1939) as the perpendicular combination bands  $\nu_2 + \nu_4^1$ , or (Sutherland 1939) as the perpendicular difference bands  $\nu_3^1 - \nu_2$ , we find that the absorption is predominantly due to the  $R$ -branch of the parallel band  $3\nu_2^0$ . Both pairs of perpendicular bands are also present, but with much lower intensity.

In the predominating perpendicular bands, the "normal" structure, as described in our first paper, is considerably more complex than appears at lower resolution. In most interpretations of perpendicular bands, a basic spacing, taken to be that of the  $^RQ$  and  $^PQ$  branches, is picked out. In most bands of ammonia the constants  $B_r - B_0$  are sufficiently large so that, under our resolution, the  $^RQ$  and  $^PQ$  branches break up into lines of different  $J$  and overlap; moreover calculation shows that their lines are less intense than those of the  $^RR$  and  $^PP$  branches. Under these circumstances, the basic spacing which can be most readily picked out is that of lines in the  $^RR$  and  $^PP$  branches, with  $n = J - K$  low. From the average spacing in these series we obtain  $C_0 - C_v\xi$ , and from their convergence,  $C_r - C_0$ .  $B_r - B_0$  is obtained from the convergence in the  $^RQ$  and  $^PQ$  branches. The  $J$ ,  $K$  numbering of the various series, and hence the band origin, may be established both by intensity relations and the recognition of constant ground-state combination differences among the  $^RR$ ,  $^RQ$ , and  $^RP$  and among the  $^PP$ ,  $^PQ$ , and  $^PR$  lines with a common upper level. The ground-state combination differences vary slightly with the inversion state; in doubtful cases this permits identification of the labelling of the inversion doublets. These are usually, but not always, resolved for  $\text{NH}_3$ . For  $\text{ND}_3$ , where the ground-state inversion splitting is very small ( $\sim 0.05\text{ cm}^{-1}$ ), the lines are resolved only in combination bands involving  $\nu_2$ .

The "normal" perpendicular structure, as sketched in the preceding paragraph, is however frequently perturbed, particularly in the combination bands  $\nu_3 + \nu_4$  and other bands with  $l \neq 1$ . The most common perturbation appears to involve both inversion levels, may be described in terms of a variation of the effective  $\xi$  with  $J$ , and presumably arises from Coriolis-type interaction forces between the observed  $E$  level and neighboring levels with  $l \pm 1$ . Other perturbations have been noted which consist of displacements of one of the two inversion levels at a few values of  $K$ ,  $J$ ; these are presumed to arise from resonant interactions with levels of high  $\nu_2$ . Until these perturbations are quanti-

tatively accounted for, the apparent values of the effective rotational constants must remain uncertain. However, fairly good values may be obtained in most of the bands by omitting grossly perturbed lines.

A further complication in the spectrum arises because of the Fermi-Dennison type resonance between  $2\nu_4^0$  and  $\nu_1$ . The resonance is not very marked in  $\text{NH}_3$  for the basic levels, but becomes so in the combination bands  $2\nu_4^0 + \nu_3$ ,  $\nu_1 + \nu_3$ , which are of nearly equal intensity. In  $\text{ND}_3$  twice  $\nu_4$  appears to be quite close to  $\nu_1$ , and results in near-equality of the inversion-splitting, rotational constants, and intensity both in the combination with  $\nu_3$ , which has been observed in detail, and in the  $\nu_1$  fundamental, where unfortunately the lower-frequency component cannot be observed, as it is obscured by atmospheric  $\text{CO}_2$  absorption. In order to deduce accurate constants for the interaction, it is necessary to obtain good rotational constants for the  $\nu_4$  fundamentals, which fall outside of the spectral range studied here. These will permit evaluation of the relative degree of mixing of  $2\nu_4$  and  $\nu_1$  in the resonating pairs. Without these data, we estimate that  $2k_{144}$  (the level splitting at exact resonance) is of the order of  $45 \text{ cm}^{-1}$  in  $\text{ND}_3$ ,  $80 \text{ cm}^{-1}$  in  $\text{NH}_3$ . The recognition of this appreciable degree of resonant mixing adds further difficulties to the calculation of harmonic potential constants for the type  $A_1$  vibrations. The low potential barrier to inversion through the planar configuration, which gives rise to high inversion splittings in  $\nu_2$ , and makes that vibrational mode very anharmonic, also complicates the problem of the  $A_1$  vibrations.

## RESULTS

The identified vibrational levels  $G_v^p$  ( $\text{cm}^{-1}$ ) are summarized in Table I. For completeness we include some levels which fall at wavelengths longer than

TABLE I  
VIBRATIONAL LEVELS OF AMMONIA ( $\text{cm}^{-1}$ )

$v_1$	$v_2$	$v_3$	$v_4$	$v_2^p = 0^a$	$0^a$	$1^a$	$1^a$	$2^a$	$2^a$	$3^a$	$3^a$
$\text{NH}_3$											
0	0	0	0	0.00	0.793	932.51	968.32	1597.6	1910	2383.46	2895.48
0	0	0	1	1626.1	1627.4	2539.6?	2585.0?				
0	0	0	2	(3216.4)	(3218.6)					$x_{24} = -14.5?$	
1	0	0	0	3336.18	3337.18	4294.51	4320.06			$x_{12} = +20.58$	
0	1	0	0	3443.59	3443.94	4416.91	4435.40			$x_{23} = +32.36$	
1	0	1	1	4955.94	4956.8					$x_{14} = -6.7$	
0	1	1	1	5052.61	5053.18	6012.72	6036.40			$x_{34} = -17.25;$ $x_{24} = -10.73$	
1	1	1	0	6608.71							
0	1	1	2	(6700?)						$x_{13} = -92??$	
0	2	0	0	6849.96	6850.39					$x_{33} = -18.50$	
$\text{ND}_3$											
0	0	0	0	0.00	0.053	745.7	749.4	1359	1429	1830	2106.60
0	0	0	1	1191							
0	0	0	2	(2359?)		3093.01	3099.46			$x_{24} = -5??$	
1	0	0	0	2420.05	2420.64	3171.89	3175.87			$x_{12} = +5.9$	
0	1	0	0	2563.96		3327.94	3329.56			$x_{23} = +17.1$	
0	1	1	2	4887.29	4887.67					$x_{34} = -18??$	
1	1	1	0	4938.44						$x_{13} = -45.84?$	
0	2	0	0	5100.66						$x_{23} = -13.63?$	

those to which our measurements extend. These are given to one decimal place. Also included, in parentheses, are levels where the analysis is not definitely verified but appears highly probable. The levels given to two decimal places are those for which we have obtained a satisfactory rotational analysis. The  $\nu_2$  levels of  $\text{NH}_3$  were observed in the difference bands  $\nu_3 - \nu_2$  and  $(\nu_2 + \nu_3 + \nu_4) - \nu_2$ . The table includes some values of the anharmonic constants  $x_{ij}$  that may be derived from the data; as discussed above, these may be quite uncertain, as they involve two questionable assumptions, that the Fermi resonance between  $2\nu_4^0$  and  $\nu_1$  is known, and that the  $\nu_2$  vibrations may be expressed by the usual power-series development.

Noteworthy in Table I are the values of the inversion splitting,  $G_v^s - G_v^a$ , which, as has long been recognized, increases rapidly with  $\nu_2$ , and is now also seen to vary with the other vibrational quantum numbers. It shows a large decrease with  $\nu_3$ , a smaller decrease with  $\nu_1$ , and an increase with  $\nu_4$ . The apparent contradictions to these regularities, in that there is increased splitting in  $\nu_1$  of  $\text{NH}_3$ , and an even greater increase in  $\nu_1$  of  $\text{ND}_3$ , are consequences of the Fermi resonance with  $2\nu_4$ .

The rotation-vibration-inversion constants are summarized in Table II. For states with  $\nu_2 < 2$ , the rotation-vibration constants are averaged for the

TABLE II  
ROTATION-VIBRATION-INVERSION INTERACTIONS IN AMMONIA

				Rotation-vibration interactions			Rotation-inversion splittings			
$\nu_1$	$\nu_2^P$	$\nu_3$	$\nu_4$	$B_v-B_0$	$C_v-C_0$	$C_0-C_v^\dagger$	$\Delta G^0$	$\Delta B$	$\Delta C$	$\Delta \zeta$
NH <sub>3</sub>										
0	1	0	0	0.032	-0.105		35.81	-0.179	0.053	
0	0	0	1	0.235	-0.066	7.756	1.3			
1	0	0	0*	-0.085	-0.083		1.00	-0.012	0.003	
1	1	0	0*	-0.1280	-0.1360		25.55	-0.1265	0.0470	
0	0	1	0	-0.176	0.009	5.934	0.35	-0.003	0.001	
0	1	1	0	-0.1975	-0.0863	5.9958	18.49	-0.0984	0.0429	0.0037
0	1	0	1	0.26	-0.14	7.82	44.8	-0.21	0.06	
1	0	0	1*	0.12	-0.105	7.739	0.86			
0	0	1	1	0.035	-0.0535	4.830	0.57			
0	1	1	1	0.012	-0.152	4.882	23.68	-0.130	0.054	0.016
1	0	1	0†	0.03	-0.12	5.98				
0	0	2*	0	-0.33	0.00	6.72	0.73			
0	2*	0	0	0.31	-0.35					
0	3*	0	0	-0.45	-0.09					
0	3*	0	0	-0.76	0.09					
ND <sub>3</sub>										
1	0	0	0†	-0.004	-0.02		0.59			
0	1	0	2*	0.0935	-0.11		6.45	-0.011	0.03	
1	1	0	0	-0.0535	-0.051		3.98	-0.005	0.00	
0	0	1	0	-0.0650	0.0002	2.702				
0	1	1	0	-0.119	-0.0286	2.709	1.62	-0.002	0.0005	
0	0	1	2*	-0.03	-0.058	2.844				
1	0	1	0	0.00	-0.040	2.704				
0	0	2*	0	-0.126	0.0026	3.946				
0	3*	0	0	-0.133	-0.03					

\*Levels are in partial Fermi resonance; constants for resonating level not available.

†Levels are in close Fermi resonance; constants for resonating level not available.

‡Levels are in close Fermi resonance; constants for both levels as listed.

inversion pair. For the higher  $v_2$ , the levels are given separately; here there are very marked curvatures of the plots of rotational energy vs.  $J(J+1)$  and  $K^2$ , so that the constants are only approximate. As mentioned above, for a complete description of the observed energy levels in all of the bands additional higher-order terms are required. It will also be noted that the interactions are not simple linear functions of the vibrational quantum numbers, so that again higher-order interactions must be evaluated before the coefficients  $\alpha_i^B$  and  $\alpha_i^C$  in the equations

$$B_v = B_e + \sum_i \alpha_i^B (v_i + g_i/2) + \dots, \quad C_v = C_e + \sum_i \alpha_i^C (v_i + g_i/2) + \dots,$$

can be found with precision.

The constant  $C_0$  cannot of course be determined directly from any perpendicular band; in symmetric-top molecules it is usually inferred from the  $\zeta$ -sum rule ( $\zeta_3 + \zeta_4 = B/2C - 1$ ). Since however for ammonia, as shown by the variations in  $C_0 - C_3\zeta$ , the values of  $\zeta$  are  $v$ -dependent, this will not lead to high accuracy. A preferred method makes use of  $C_0 - C_3\zeta$  from the  $\nu_3$  and  $2\nu_3^2$  bands. Since for the latter band we have  $\zeta \cong -2\zeta_3$ , and  $C_0 - C_3$  is small,  $C_0 = \frac{1}{3}[2(C_0 - C_3\zeta)_{\nu_3} + (C_0 - C_3\zeta)_{2\nu_3^2}]$ . Combining our  $\text{NH}_3$ ,  $\nu_3$ , results with the Raman-effect data of Cumming and Welsh (1953) yields nearly the same value, but since their resolution is not comparable, the result is less reliable. Table III summarizes the rotational constants and zetas derived

TABLE III  
ROTATIONAL CONSTANTS AND MOLECULAR DIMENSIONS

$v$	$\text{NH}_3$			$\text{ND}_3$		
	$B, \alpha^B$	$C, \alpha^C$	$\zeta$	$B, \alpha^B$	$C, \alpha^C$	$\zeta$
0	9.9443	6.196		5.1426	3.117	
1	-0.135	-0.078		-0.032	-0.052	
2	-0.015	-0.098		-0.054	-0.0288	
3	-0.176	0.009	0.0422	-0.0650	0.0002	0.1331
4	0.230	-0.066	-0.255	0.080	-0.025	(-0.320)
$e$	9.965	6.341		5.1708	3.182	

Molecule, state				
	$\text{NH}_3$ , eq.	$\text{ND}_3$ , eq.	$\text{NH}_3$ , $v=0$	$\text{ND}_3$ , $v=0$
$I^B, 10^{-40}$ g.cm. <sup>2</sup>	2.8088	5.4131	2.8147	5.4428
$I^C, 10^{-40}$ g.cm. <sup>2</sup>	4.4141	8.7963	4.5164	8.9776
$h, 10^{-8}$ cm.	0.3816	0.3805	0.3670	0.3687
$r, 10^{-8}$ cm.	1.0124	1.0108	1.0173	1.0155
$\angle \text{H-N-H}$ , deg.	106.67	106.70	107.78	107.59

in this manner. Making reasonable assumptions as to the influence of interactions on the  $B_v - B_0$  and  $C_v - C_0$ , we obtain estimates for the  $\alpha_i^z$  which are also tabulated, and from these are derived the tabulated equilibrium moments of inertia and molecular dimensions. The last quantities agree satisfactorily for  $\text{NH}_3$  and  $\text{ND}_3$ . The probable error in  $B_e$  and  $C_e$  is  $\pm 0.02 \text{ cm}^{-1}$ .

With the average values of the molecular dimensions,  $r_e = 1.0116 \times 10^{-8}$  cm.,  $h_e = 0.3810 \times 10^{-8}$  cm. ( $h$  is the distance of the N atom above the H plane), we may now test the product rule for vibrations and the Meal-Polo (1956) sum rule. The results are given in Table IV. As would be expected, when the

TABLE IV  
VIBRATIONAL PRODUCT AND SUM RULES IN  $\text{NH}_3$  AND  $\text{ND}_3$

Class considered	Ratio $\text{ND}_3/\text{NH}_3$ , using:		
	$\nu_{\text{obs}}$	$\omega^?$	$\omega$ (theor.)
Product $\omega_e, A_1$	0.5709	0.5522	0.54266
Product $\omega_e, E$	0.5449	0.5370	0.53418
Sum $\omega_e^2(1 - \zeta), E$	0.5157	0.5097	0.50038

positions of the fundamentals are used, the product rules are poorly obeyed, especially for the type  $A$  vibrations, where  $\nu_1$  is perturbed by Fermi resonance with  $2\nu_4^0$ , and where the small-oscillation-harmonic-force assumption breaks down badly for  $\nu_2$ , with its low potential barrier to inversion.

In the second column of Table IV, the frequencies were corrected for anharmonicity using the available  $x$ 's, and making what appear to be reasonable estimates for those as yet undetermined. Although considerable improvement results, the lack of agreement with the theoretical values is evidence that more data are required before final values of the potential constants can be derived.

It is nevertheless possible to obtain harmonic potential constants that fit the data for the frequencies, the  $\zeta$ 's, and the centrifugal stretching constants in a fairly consistent manner. These are given in Table V. Dennison's notation is used for the six potential constants. For each molecule, the three constants  $\alpha, \beta, \gamma$  were determined from  $\omega_3, \omega_4$ , and  $\zeta_3$ .  $a, b$ , and  $c$  were determined from  $\omega_1, \omega_2$ , and  $D^J$ . (Inasmuch as  $D^J$  and  $D^{JK}$  are observed for  $v = 0$ , in their calculation we used the  $v = 0$ , rather than the equilibrium, values of the molecular framework and frequencies.) It will be noted that the constants run similarly for  $\text{NH}_3$  and  $\text{ND}_3$ , and that the tabulated entries, calculated from the averaged constants, reproduce the data adequately.

#### CONCLUSION

It is believed that although the results reported in this paper for the equilibrium moments of inertia and the harmonic potential constants involve a certain amount of uncertainty, they are more soundly based than any previous data. They may accordingly be used with some confidence as the basis for further computations involving the interaction of one vibration with another. These should permit evaluation of the perturbation effects that appear in various of the observed bands, and this in turn may lead to a final determination of the structure. These matters will be discussed in subsequent papers, in which further details of the experimental data will be presented. The present constants may also be checked and refined by applying them to other isotopic forms of ammonia.

TABLE V  
 CONSTANTS DERIVED FROM THE HARMONIC POTENTIAL FUNCTION

Constant	NH <sub>3</sub>		ND <sub>3</sub>	
	Calc.	Obs.	Calc.	Obs.
$\omega_3$ (cm <sup>-1</sup> )	3590.51	3577	2642.18	2651.6
$\omega_4$ (cm <sup>-1</sup> )	1689.11	1691	1226.32	1225
$\xi_3 \times 10^3$	35.98	42.2	139.41	133.1
$\xi_4 \times 10^3$	-249.09	-255	-326.42	
$\omega_1$ (cm <sup>-1</sup> )	3516.98	3506	2496.96	2495
$\omega_2$ (cm <sup>-1</sup> )	1030.93	1021.5	785.51	792.6
$D_0^J$ (10 <sup>-4</sup> cm <sup>-1</sup> )	8.06	8.09	1.953	1.95
$-D_0^K$ (10 <sup>-4</sup> cm <sup>-1</sup> )	14.61	14.55	3.441	3.66
$D_0^K$ (10 <sup>-4</sup> cm <sup>-1</sup> )	8.14	*	1.890	*

Potential constants (10 <sup>3</sup> dyne/cm.)						
	$\alpha$	$\beta$	$\gamma$	$a$	$b$	$c$
NH <sub>3</sub>	9.9766	4.1559	4.0522	2.9368	6.7273	2.9310
ND <sub>3</sub>	10.0210	4.2413	4.1466	3.0034	6.6983	2.9324
Av., this work	9.9988	4.1986	4.0994	2.9701	6.7128	2.9317
Dennison	10.494	4.098	4.168	3.171	6.811	3.078

\*Cannot be measured uniquely, but only as the combination  $D_0^K + \xi_v K$ , where the latter is the coefficient of the term  $\pm \xi_v K^2$  in a degenerate upper state. In the most accurately measured bands of NH<sub>3</sub> ( $\nu_3 + \nu_2$ ),  $D_0^K + \xi_v K = 7.31 \times 10^{-4}$ ; and in ND<sub>3</sub> ( $\nu_3$ ),  $D_0 + \xi_v K = 2.2 \times 10^{-4}$ .

## REFERENCES

- BARKER, E. F. 1939. Phys. Rev. **55**, 657.  
 BENEDICT, W. S., PLYLER, E. K., and TIDWELL, E. D. 1957. J. Research N.B.S. (In press).  
 CUMMING, C. and WELSH, H. L. 1953. J. Chem. Phys. **21**, 1119.  
 DENNISON, D. M. 1940. Revs. Mod. Phys. **12**, 194.  
 HERZBERG, G. 1945. Infrared and Raman spectra of polyatomic molecules (D. Van Nostrand Co., Inc., New York).  
 MEAL, J. H. and POLO, S. R. 1956. J. Chem. Phys. **24**, 1126.  
 NIELSEN, H. H. 1951. Revs. Mod. Phys. **23**, 90.  
 SUTHERLAND, G. B. B. M. 1939. Phys. Rev. **56**, 836.



# THE SPECTRUM OF THE $P_2^+$ MOLECULE<sup>1</sup>

N. A. NARASIMHAM<sup>2</sup>

## ABSTRACT

Two band systems attributed to the  $P_2^+$  molecule have been excited in a hollow cathode discharge tube. The first of these is a  ${}^2\Pi-{}^2\Pi$  band system lying in the region 3400–3850 Å. The lower state of this system probably is the ground state of the  $P_2^+$  molecule. The second system is a  ${}^2\Sigma-{}^2\Sigma$  system lying in the region 3900–4400 Å. High resolution spectra of both the band systems have been analyzed and the rotational and vibrational constants determined.

## I. INTRODUCTION

Many band systems of  $N_2$  and  $N_2^+$  are known but comparatively few are known for  $P_2$  and none at all for  $P_2^+$ . Recently in this laboratory two band systems, a  ${}^2\Pi-{}^2\Pi$  and a  ${}^2\Sigma-{}^2\Sigma$  system, attributed to  $P_2^+$  have been obtained in emission from a hollow cathode discharge. Five bands of the latter system were obtained by Herzberg (1932) under low dispersion and were suggested to be due to  $P_2$ . The present studies, however, show that they belong to the  ${}^2\Sigma-{}^2\Sigma$  system of  $P_2^+$ . Excitation of the two band systems and their analyses are described below.

## II. EXPERIMENTAL

The emission spectrum of  $P_2^+$  was excited in a hollow cathode discharge through helium containing a little phosphorus vapor. The pressure of helium was maintained at 2–3 mm. of mercury. The discharge tube and a side bulb containing phosphorus were enclosed in a water bath at a temperature of 40–44° C. The spectrum was photographed first on a Hilger medium quartz spectrograph and later on a 35 ft. concave grating spectrograph in the second order. Besides the strong ultraviolet bands of  $P_2$ , the spectrum showed many new bands in the region between 3400 and 9000 Å. In the present paper two band systems, one a  ${}^2\Pi-{}^2\Pi$  system in the 3400–3850 Å region and the other a  ${}^2\Sigma-{}^2\Sigma$  system in the 3900–4400 Å region, are described.

## III. THE ${}^2\Pi-{}^2\Pi$ SYSTEM

The bands of the  ${}^2\Pi-{}^2\Pi$  system lie in the region 3400–3850 Å and are degraded to the red. Each band of the system is found to consist of two subbands, a  ${}^2\Pi_{3/2}-{}^2\Pi_{3/2}$  and a  ${}^2\Pi_{1/2}-{}^2\Pi_{1/2}$ , which indicates that the coupling in both the upper and lower  ${}^2\Pi$  states belongs to Hund's case (a) (large spin splitting). The  ${}^2\Pi_{3/2}-{}^2\Pi_{3/2}$  component of the 1–0 band and the  ${}^2\Pi_{1/2}-{}^2\Pi_{1/2}$  component of the 2–0 band are reproduced in Fig. 1 (a) and (b). There is considerable overlapping of the subbands owing to the fact that the vibrational frequency of the upper  ${}^2\Pi$  state is nearly equal to the doublet splitting

<sup>1</sup>Manuscript received June 26, 1957.

Contribution from the Division of Pure Physics, National Research Council, Ottawa, Canada.

Issued as N.R.C. No. 4495.

<sup>2</sup>National Research Laboratories Postdoctorate Fellow.



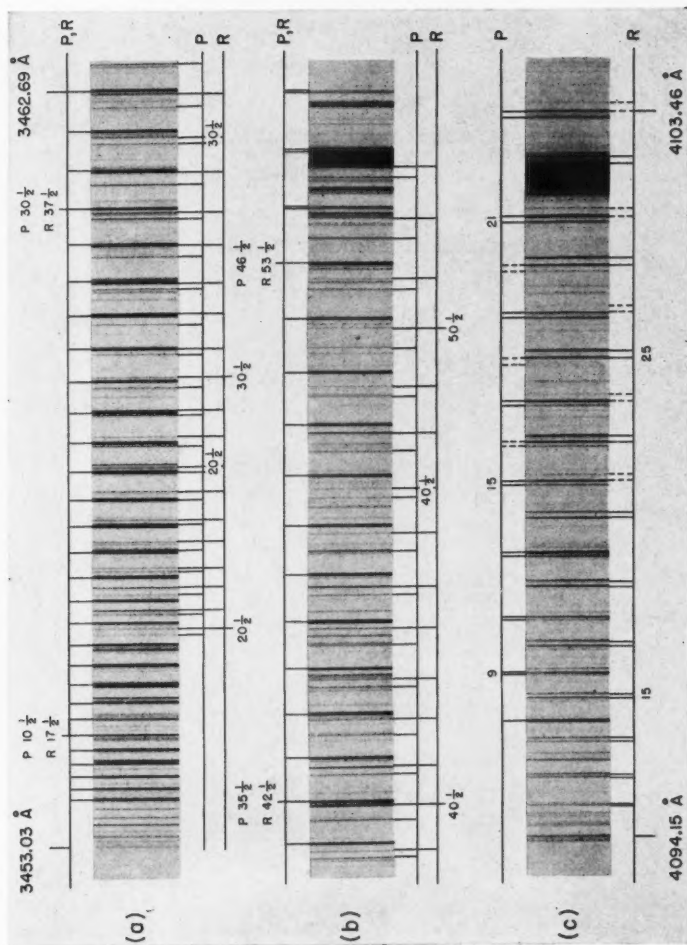


FIG. 1 (a) and (b). The  $21I_{3/2}-21II_{3/2}$  component of the (1-0) band indicated by the leading lines at the top and the  $21I_{3/2}-21II_{3/2}$  component of the (2-0) band indicated by the leading lines at the bottom of the spectrograms (a) and (b). The lines of the  $P$  and  $R$  branches of the  $21I_{3/2}-21II_{3/2}$  subband overlap and they begin to separate out at  $P(47\frac{1}{2})$  and  $R(54\frac{1}{2})$ .  
(c) The (4-0) band of the  $22-25$  system. Weaker doublets of the  $P$  and  $R$  branches are shown by broken leading lines and the stronger doublets by solid leading lines.



TABLE I  
WAVE NUMBERS OF THE LINES OF THE  $\Pi-\Pi$  BANDS OF P<sub>2</sub><sup>+</sup>

J + 1	0-0 Band				0-1 Band				0-2 Band			
	$\Pi_{1/2}-\Pi_{1/2}$		$\Pi_{1/2}-\Pi_{3/2}$		$\Pi_{1/2}-\Pi_{1/2}$		$\Pi_{1/2}-\Pi_{3/2}$		$\Pi_{1/2}-\Pi_{3/2}$		$\Pi_{1/2}-\Pi_{3/2}$	
	P(J+1)	R(J+1)	P(J+1)	R(J+1)	P(J+1)	R(J+1)	P(J+1)	R(J+1)	P(J+1)	R(J+1)	P(J+1)	R(J+1)
10												
11												
12												
13	28506.42	28517.54			27843.39	27855.42	27405.46	27417.50	27173.90	27181.12		
14	04.37	16.35			41.28	54.14						
15	†	15.08			39.01	52.77						
16	496.95	13.73			36.72	51.34						
17	97.54	12.15			34.43	49.91						
18	95.03	10.50			32.10	48.48						
19		06.88			29.05	46.18						
20	86.70*	04.89			26.31	44.26						
21	86.92	†			23.34	42.22						
22	83.90	00.51			20.29	40.03						
23	80.82	498.17			17.18	37.74						
24	77.62	83.70			14.02	35.45						
25	74.30	65.70			10.87	33.16						
26	70.98	47.69			7.74	30.87						
27	67.30	28.84			4.61	28.58						
28	63.61	25.42			07.10	26.29						
29	59.80	49.38			03.48	24.00						
30	55.90	81.54*			799.75	21.71						
31	51.84	78.36			95.93	19.42						
32	47.69	56.19			87.03	17.13						
33	43.44	34.00			83.76	14.84						
34	39.06	68.12			79.46	12.55						
35	34.51*	†			75.11	10.26						
36	29.95	60.67			70.82	07.97						
37	25.18	56.78			66.53	05.68						
38	20.34	52.89			62.24	03.39						
39	15.51	48.99			57.95	01.10						
40	10.21	44.39			53.66	00.00						
41	05.02	39.99			49.37	00.00						
42	399.67	35.57			45.08	00.00						
43	94.22	†			40.79	00.00						
44	88.63	20.19			36.50	00.00						
45	83.07	16.35			32.21	00.00						
46	77.12	†			27.92	00.00						
47	71.18	†			23.63	00.00						
48	65.14	†			19.34	00.00						
49	58.97	†			15.05	00.00						
50	52.31	†			10.76	00.00						

\*Overlapped lines.

†Overlapped but not measured.



of the bands. For a  ${}^2\Pi\text{--}{}^2\Pi$  transition, each subband is expected to show a  $P$ , a very weak  $Q$ , and an  $R$  branch each consisting of narrow  $\Lambda$ -doublets. The  $\Lambda$ -doublets are well resolved only in the  ${}^2\Pi_{1/2}\text{--}{}^2\Pi_{1/2}$  subband. One  $\Lambda$ -component of each doublet is observed to be strong and the other to be weak. These strong and weak lines alternate successively in each of the  $P$  and  $R$  branches. Such an intensity alternation indicates that the bands arise from a homonuclear molecule. The weaker lines cannot be seen distinctly in the reproduction of the  ${}^2\Pi_{1/2}\text{--}{}^2\Pi_{1/2}$  subband in Fig. 1 (a) and (b) and the  $\Lambda$ -doubling shows up only as a marked "staggering" of the stronger lines of the  $P$  and  $R$  branches. In the  ${}^2\Pi_{3/2}\text{--}{}^2\Pi_{3/2}$  component where only a negligibly small  $\Lambda$ -doubling is to be expected (Mulliken and Christy 1931), the  $P$  and  $R$  branches were observed as series of unresolved doublets with no apparent staggering of the lines.

Six bands of the  ${}^2\Pi_{3/2}\text{--}{}^2\Pi_{3/2}$  transition and five of  ${}^2\Pi_{1/2}\text{--}{}^2\Pi_{1/2}$  have been measured and analyzed. The wave numbers of the lines of the bands are given in Table I. The effective rotational constants of the upper and lower  ${}^2\Pi$  states were determined from the following relation:

$$\Delta_2 F(J) = 4B_v(J + \frac{1}{2}) - 8D_v(J + \frac{1}{2})^3,$$

where the combination differences,  $\Delta_2 F(J)$ , of the upper and lower states are obtained from

$$\Delta_2 F'(J) = R(J) - P(J)$$

and

$$\Delta_2 F''(J) = R(J-1) - P(J+1).$$

The resulting  $B_v$  values are given in Table II.

TABLE II  
THE EFFECTIVE  $B_v$  VALUES AND BAND ORIGINS

Band $v'-v''$	$\nu_0$	$B''$	$B'$
${}^2\Pi_{1/2}\text{--}{}^2\Pi_{1/2}$ subbands			
0-0	28083.87	0.274 <sub>4</sub>	0.214 <sub>4</sub> <sup>a</sup>
1-0	28517.13		0.212 <sub>5</sub> <sup>b</sup>
2-0	28945.53		0.211 <sub>1</sub>
0-1	27422.58	0.272 <sub>4</sub>	0.214 <sub>4</sub> <sup>a</sup>
1-1	27855.84		0.212 <sub>8</sub> <sup>b</sup>
${}^2\Pi_{3/2}\text{--}{}^2\Pi_{3/2}$ subbands			
0-0	28521.74	0.273 <sub>4</sub>	0.214 <sub>8</sub> <sup>c</sup>
1-0	28950.78		0.213 <sub>0</sub> <sup>d</sup>
2-0	29374.53		0.211 <sub>5</sub> <sup>e</sup>
0-1	27860.58	0.271 <sub>7</sub>	0.214 <sub>8</sub> <sup>c</sup>
1-1	28289.62		0.213 <sub>0</sub> <sup>d</sup>
0-2	27204.68	0.270 <sub>5</sub>	0.211 <sub>5</sub> <sup>e</sup>

<sup>a, b, c, d, e</sup> These are not independent  $B_{eff}$  values but are determined from the averages of the common combination differences.

In the lower state, the effective  $B_0''$  value (0.2744) of the  ${}^2\Pi_{1/2}$  component is larger than the  $B_0''$  value (0.2734) of the  ${}^2\Pi_{3/2}$  component. This implies that the two spin components of the  ${}^2\Pi$  state form an inverted doublet. On the

other hand, the  $B_0'$  values of the  ${}^2\Pi_{1/2}$  and the  ${}^2\Pi_{3/2}$  components of the upper  ${}^2\Pi$  state indicate that they form a regular doublet.

The effective  $B_v$  values of the  ${}^2\Pi_{1/2}$  and  ${}^2\Pi_{3/2}$  components of the  ${}^2\Pi$  states belonging to Hund's case (a) differ from the true  $B_v$  values of the  ${}^2\Pi$  states by an amount  $B_0/A$  as given below (Mulliken 1931):

$$B_{\text{eff}} = B_v(1 \pm B_0/A),$$

where  $A$  is the coupling constant between the spin  $S$  and the orbital angular momentum  $\Lambda$ . From this relation, the spin splittings,  $A'$  and  $A''$ , of the upper and lower  ${}^2\Pi$  states were determined and included in Table III. In the  ${}^2\Pi$ — ${}^2\Pi$  transition, where the upper state is a regular and the lower an inverted doublet, the sum of the values of  $A'$  and  $A''$  gives the doublet splitting of the bands. The calculated  $A' + A''$  value for the two  ${}^2\Pi$  states with  $v = 0$  agrees well with the observed doublet splitting of the bands.

TABLE III  
CONSTANTS OF THE  ${}^2\Pi$ — ${}^2\Pi$  BANDS IN  $\text{cm}^{-1}$

	Lower ${}^2\Pi$ state	Upper ${}^2\Pi$ state
$B_v$	0.2748	0.2154
$r_e$	2.2480 Å	1.9902 Å
$\alpha$	0.0017	0.0017
$A$	-150	~230

The vibrational levels of the upper and lower  ${}^2\Pi$  states are given in an energy level diagram in Fig. 2. In the drawing, the values of  $A'$  and  $A''$  (Table III) were used for the spin splitting of the upper and lower  ${}^2\Pi$  states. The  $B_{\text{eff}}$  and  $\Delta G$  values were also included in the diagram.

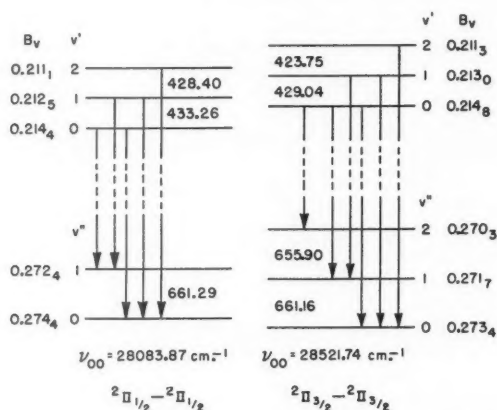


FIG. 2. An energy level diagram of the vibrational levels of the  ${}^2\Pi$ — ${}^2\Pi$  band system. The  $B_v$  and  $\Delta G$  values ( $\text{cm}^{-1}$ ) are shown in the diagram.

TABLE IV. WAVE NUMBERS OF THE LINES OF THE  $2\Sigma^+ - 2\Sigma_g^+$  BANDS OF THE  $P_2^+$  MOLECULE

N	0.0	1.0	2.0	3.0	4.0	5.0	6.0	7.1	8.1	
	P(N)	R(N)	P(N)	R(N)	P(N)	R(N)	P(N)	R(N)	P(N)	R(N)
5 {	23622.12	20.31	24016.22	24415.79	24791.08	25177.69	25471.09	25169.04		
7 {	23622.12	20.31	24016.22	24415.79	24791.08	25177.69	25471.09	25169.04		
9 {	19.02	28.12	24016.22	24016.22	24016.22	24016.22	24016.22	24016.22		
11 {	18.87	27.95	24016.22	24016.22	24016.22	24016.22	24016.22	24016.22		
13 {	18.87	27.95	24016.22	24016.22	24016.22	24016.22	24016.22	24016.22		
15 {	18.87	27.95	24016.22	24016.22	24016.22	24016.22	24016.22	24016.22		
17 {	18.87	27.95	24016.22	24016.22	24016.22	24016.22	24016.22	24016.22		
19 {	18.87	27.95	24016.22	24016.22	24016.22	24016.22	24016.22	24016.22		
21 {	18.87	27.95	24016.22	24016.22	24016.22	24016.22	24016.22	24016.22		
23 {	18.87	27.95	24016.22	24016.22	24016.22	24016.22	24016.22	24016.22		
25 {	18.87	27.95	24016.22	24016.22	24016.22	24016.22	24016.22	24016.22		
27 {	18.87	27.95	24016.22	24016.22	24016.22	24016.22	24016.22	24016.22		
29 {	18.87	27.95	24016.22	24016.22	24016.22	24016.22	24016.22	24016.22		
31 {	18.87	27.95	24016.22	24016.22	24016.22	24016.22	24016.22	24016.22		
33 {	18.87	27.95	24016.22	24016.22	24016.22	24016.22	24016.22	24016.22		
35 {	18.87	27.95	24016.22	24016.22	24016.22	24016.22	24016.22	24016.22		
37 {	18.87	27.95	24016.22	24016.22	24016.22	24016.22	24016.22	24016.22		
39 {	18.87	27.95	24016.22	24016.22	24016.22	24016.22	24016.22	24016.22		
41 {	18.87	27.95	24016.22	24016.22	24016.22	24016.22	24016.22	24016.22		
43 {	18.87	27.95	24016.22	24016.22	24016.22	24016.22	24016.22	24016.22		
45 {	18.87	27.95	24016.22	24016.22	24016.22	24016.22	24016.22	24016.22		
47 {	18.87	27.95	24016.22	24016.22	24016.22	24016.22	24016.22	24016.22		
49 {	18.87	27.95	24016.22	24016.22	24016.22	24016.22	24016.22	24016.22		
51 {	18.87	27.95	24016.22	24016.22	24016.22	24016.22	24016.22	24016.22		
53 {	18.87	27.95	24016.22	24016.22	24016.22	24016.22	24016.22	24016.22		

\*Overlapped lines.

†Overlapped but not measured.

IV. THE  $^2\Sigma-^2\Sigma$  SYSTEM

The bands of the  $^2\Sigma-^2\Sigma$  system are also degraded to the red and lie in the region 3900–4400 Å. Only eight bands of this system were observed. They form two  $v'-v''$ -progressions with  $v'' = 0$  and 1. Only the relative vibrational numbering of the bands is known. The band at 4094 Å is reproduced in Fig. 1 (c). For a  $^2\Sigma-^2\Sigma$  transition, the rotational structure is expected to have a  $P$  and an  $R$  branch, each of which is composed of the subseries  $P_1$ ,  $P_2$ , and  $^PQ_{12}$  and  $R_1$ ,  $R_2$ , and  $^RQ_{21}$ . However, except for very small  $N$  values, the satellite branches,  $^PQ_{12}$  and  $^RQ_{21}$ , are of negligible intensities so that the band shows a doublet  $P$  and a doublet  $R$  branch. The  $P$  and  $R$  branches show an intensity alternation which indicates that the emitter of the band system is a homonuclear molecule. The weaker doublets are indicated by broken leading lines and the stronger doublets by solid leading lines. The measurements of only the stronger doublets were used in the analysis of the bands. The wave numbers of the lines of the  $^2\Sigma-^2\Sigma$  bands are given in Table IV.

The rotational constants of the  $^2\Sigma$  states were obtained from the relation:

$$\Delta_2 F(N) = 4B_v(N + \frac{1}{2}) - 8D_v(N + \frac{1}{2})^3.$$

The combination differences  $\Delta_2 F(N)$  of the lower and the upper states were obtained in the usual manner taking

$$\Delta_2 F''(N) = R(N-1) - P(N+1)$$

and

$$\Delta_2 F'(N) = R(N) - P(N).$$

For  $P(N)$  and  $R(N)$ , average values of each doublet, viz.,

$$P(N) = \frac{1}{2} \{ P_1(N) + P_2(N) \}$$

and

$$R(N) = \frac{1}{2} \{ R_1(N) + R_2(N) \},$$

were used.

The band origins were determined using the strong lines of the  $P$  and  $R$  branches from the following relation:

$$R(N) + P(N) = 2\nu_0 + 2B_v' + 2(B_v' - B_v'')N(N+1) - 2(D_v' - D_v'')N^2(N+1)^2.$$

The resulting rotational constants and band origins are given in Table V.

TABLE V  
BAND ORIGINS AND ROTATIONAL CONSTANTS OF THE  
 $^2\Sigma_u^+ - ^2\Sigma_g^+$  BANDS

Band* $v'-v''$	$\nu_0$	$B''$	$B'$
0-0	23224.89	0.3027	0.240 <sub>6</sub>
1-0	23629.01		0.238 <sub>6</sub>
2-0	24026.30		0.236 <sub>3</sub>
3-0	24417.15		0.234 <sub>6</sub>
4-0	24801.53		0.233 <sub>0</sub>
5-0	25179.53	0.3006	0.230 <sub>5</sub>
6-0	25551.37		0.228 <sub>5</sub>
7-1	25183.69		0.226 <sub>0</sub>
8-1	25543.37		0.223 <sub>7</sub>

\*Only the relative vibrational numbering of the bands is known.



In this band system the odd-numbered  $P$  and  $R$  doublets are found to be more intense than the even-numbered doublets. Since the phosphorus nuclei obey Fermi statistics (with spin  $= \frac{1}{2}$ ), the above observation indicates that the transition of the band system is either a  ${}^2\Sigma_g^+ \rightarrow {}^2\Sigma_g^+$  or a  ${}^2\Sigma_g^- \rightarrow {}^2\Sigma_u^-$ . A consideration of the low lying electronic states of  $\text{P}_2^+$ , given below, shows the former transition is involved in this band system.

## V. DISCUSSION

Phosphorus and nitrogen have similar electronic structures, namely,

$$K K (\sigma_a 2s)^2 (\sigma_u 2s)^2 (\pi_u 2p)^4 (\sigma_a 2p)^2 \quad \text{for N}_2$$

and

$$KKLL(\sigma_g 3s)^2(\sigma_u 3s)^2(\sigma_g 3p)^2(\pi_u 3p)^4 \quad \text{for } P_2.$$

Both configurations give rise to  $1\Sigma_g^+$  ground states. However, since the order of the molecular orbitals of  $P_2$  is different from that of  $N_2$ , the first excited electron configuration of  $P_2$  is  $\dots (\pi_u 3p)^3 \pi_g 3p$  instead of  $\dots (\sigma_g 2p)\pi_g 2p$  of  $N_2$  (Herzberg 1950). This accounts for the different excited states,  $1\Sigma_u^+$  and  $1\Pi_g$ , observed respectively in the absorption spectra of  $P_2$  ( $1\Sigma_u^+ \rightarrow 1\Sigma_g^+$ ) and of  $N_2$  ( $1\Pi_g \rightarrow 1\Sigma_g^+$ ). A further consequence of the changed order of the molecular orbitals is that  $P_2^+$  is expected to have a  $2\Pi_{u(\text{inv})}$  state for its ground state rather than a  $2\Sigma_g^+$  state as for  $N_2^+$ . For  $N_2^+$ , the corresponding  $2\Pi_u$  state is the well-known  $A\ 2\Pi_u$  state which lies  $9168\text{ cm}^{-1}$  above the ground state. It is very likely that the lower  $2\Pi_{(\text{inv})}$  state of the  $2\Pi \rightarrow 2\Pi$  band system of the  $P_2^+$  molecule discussed above is its ground state.

The electronic states involved in the two band systems may be correlated with the following low electronic states of  $P_2^+$ :

$$\begin{array}{llll}
KKLL(\sigma_g 3s)^2(\sigma_u 3s)^2(\sigma_g 3p)^2(\pi_u 3p)^3 \dots & {}^2\Pi_u(\text{inv}) \\
'' & '' & (\sigma_g 3p)(\pi_u 3p)^4 \dots & {}^2\Sigma_g^+ \\
(\sigma_u 3s)(\sigma_g 3p)^2(\pi_u 3p)^4 \dots & {}^2\Sigma_u^+ \\
(\sigma_u 3s)^2(\sigma_g 3p)^2(\pi_u 3p)^2\pi_g 3p^2 & {}^2\Pi_g(\text{reg})
\end{array}$$

The last of these electron configurations gives rise to two  ${}^2\Pi_{\theta(\text{inv})}$ , one  ${}^2\Phi_{\theta(\text{reg})}$ , and one  ${}^4\Pi_{\theta(\text{reg})}$  states besides the  ${}^2\Pi_{\theta(\text{reg})}$  state.

## ACKNOWLEDGMENTS

I wish to thank Dr. A. E. Douglas for his ready help and advice during the course of this investigation. My sincere thanks are also due to Drs. G. Herzberg and B. Kleman for many helpful discussions.

## REFERENCES

- HERZBERG, G. 1932. *Ann. Physik*, **15**, 677.  
 ——— 1950. *Molecular spectra and molecular structure*, Vol. I, Spectra of diatomic molecules (D. Van Nostrand Company, Inc., Princeton, N.J.).  
 MULLIKEN, R. S. 1931. *Revs. Modern Phys.* **3**, 89.  
 MULLIKEN, R. S. and CHRISTY, A. 1931. *Phys. Rev.* **38**, 87.

## NOTES

### A SIMPLE RECTANGULAR PULSE GENERATOR\*

H. L. ARMSTRONG†

A generator of rectangular pulses is frequently required for applications in instrumentation, testing, etc. Sometimes the elaborations of a commercial instrument are not needed, and quite simple and economical circuits will suffice.

The cathode coupled multivibrator (Chance *et al.* 1949), in the modification shown in Fig. 1, has been found to be very useful as such a pulse generator. The capacitor coupling between cathodes permits the output voltage to fall to

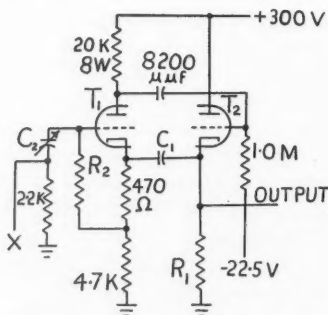


FIG. 1. The circuit diagram of the pulse generator.  $R_1$  is 4.7 K,  $R_2$  is 1.0 M,  $C_1$  is 0.5  $\mu\text{f.}$ , and  $C_2$  is a variable, about 1000  $\mu\text{f.}$  maximum. If desired,  $R_1$  may be replaced by a 5 K potentiometer, and the output taken from the slider. Negative triggers are applied at point X.

zero between pulses, which is often desirable. Negative triggers are applied at point X; positive triggers at the grid of  $T_2$  will also work, but the former arrangement is usually preferable. The use of a variable capacitor for  $C_2$ , as shown, will provide variable pulse lengths up to 300 microseconds or so.

For longer pulses,  $R_2$  may be made variable instead. By replacing  $R_1$  by a 5 K potentiometer, and taking the output from the slider, a variable amplitude output may be obtained with very little waveform distortion.

The component values not shown on the drawing were as follows:  $R_1$  was 4.7 K,  $R_2$  was 1.0 M,  $C_1$  was 0.5  $\mu\text{f.}$ , and  $C_2$  was a variable with a maximum setting of about 1000  $\mu\text{f.}$ ;  $T_1$  and  $T_2$  were each one-half of a 12BH7A.

The 12BH7A is probably one of the best small tubes for this application if a large output is desired; with this circuit over 100 volts was obtained. For other needs, other types may be better; the writer once had some very good results

\*Issued as N.R.C. No. 4471.

†Present address: Pacific Semiconductors, Inc., Culver City, California.

generating short, rapidly rising pulses with a similar circuit using a 6BK7. The new triode-pentode combinations offer interesting possibilities of having similar circuits, all in one envelope, and with an extra electrode for various uses. Some of these possibilities have already been pointed out (Armstrong 1956).

Figure 2 shows the waveform obtained with this pulse generator. The horizontal scale is 50 microseconds per centimeter, the vertical, 25 volts per centimeter.

Figure 3 shows a simple trigger generator which was used to provide triggers for this multivibrator. The variable resistor, typically from 5 to 10 megohms maximum, controls the repetition rate. The triggers are applied to the multivibrator by having points *X* in Figs. 1 and 3 joined. The inductor is added to delay the pulse until an oscilloscope, triggered from the lead worked "to C.R.O.", can start; a 500 millihenry inductor gave a delay of about 20 microseconds. The trigger amplitude and duration are not very critical; 10 to 20

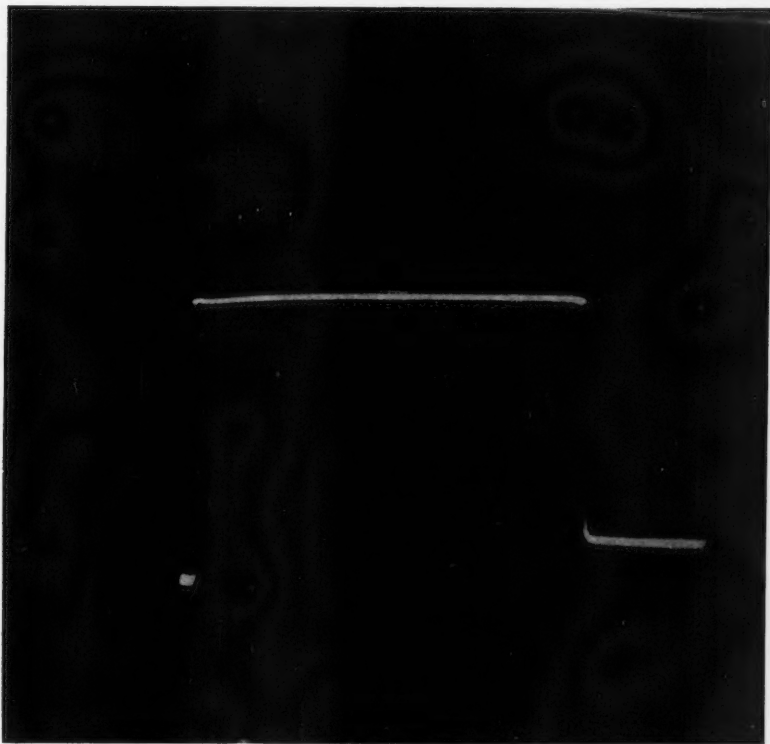


FIG. 2. The waveform produced by the pulse generator. The horizontal scale is 50 microseconds per cm. (main division), the vertical, 25 volts per cm.

volts, and duration from 1/10 microsecond up to a few per cent of the pulse length, will suffice.

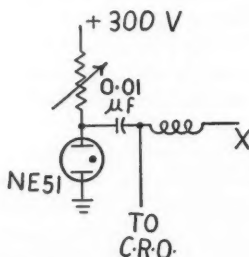


FIG. 3. The trigger generator used with this pulse generator. The repetition rate is varied by varying the variable resistor. The triggers are applied to the pulse generator by having the points marked "X" on Figs. 1 and 3 connected.

In conclusion, the circuit discussed can provide a simple and economical source of pulses of amplitude up to more than 100 volts, durations from a few microseconds to a few milliseconds, and rise times typically from 1/10 to 1 microsecond.

ARMSTRONG, H. L. 1956. *Electronics*, July, p. 210.

CHANCE, B., HUGHES, V., MACNICHOL, E. F., SAYRE, D., and WILLIAMS, F. C. 1949. *Waveforms* (McGraw-Hill Book Co., Inc., New York), Section 5.10.

RECEIVED APRIL 26, 1957.

DIVISION OF RADIO AND ELECTRICAL ENGINEERING,  
NATIONAL RESEARCH COUNCIL,  
OTTAWA, CANADA.

## THE PHYSICAL SOCIETY

MEMBERSHIP of the Society is open to all who are interested in Physics.

FELLOWS pay an Entrance fee of £1 1s. (\$3.00) and an Annual Subscription of £2 2s. (\$6.00).

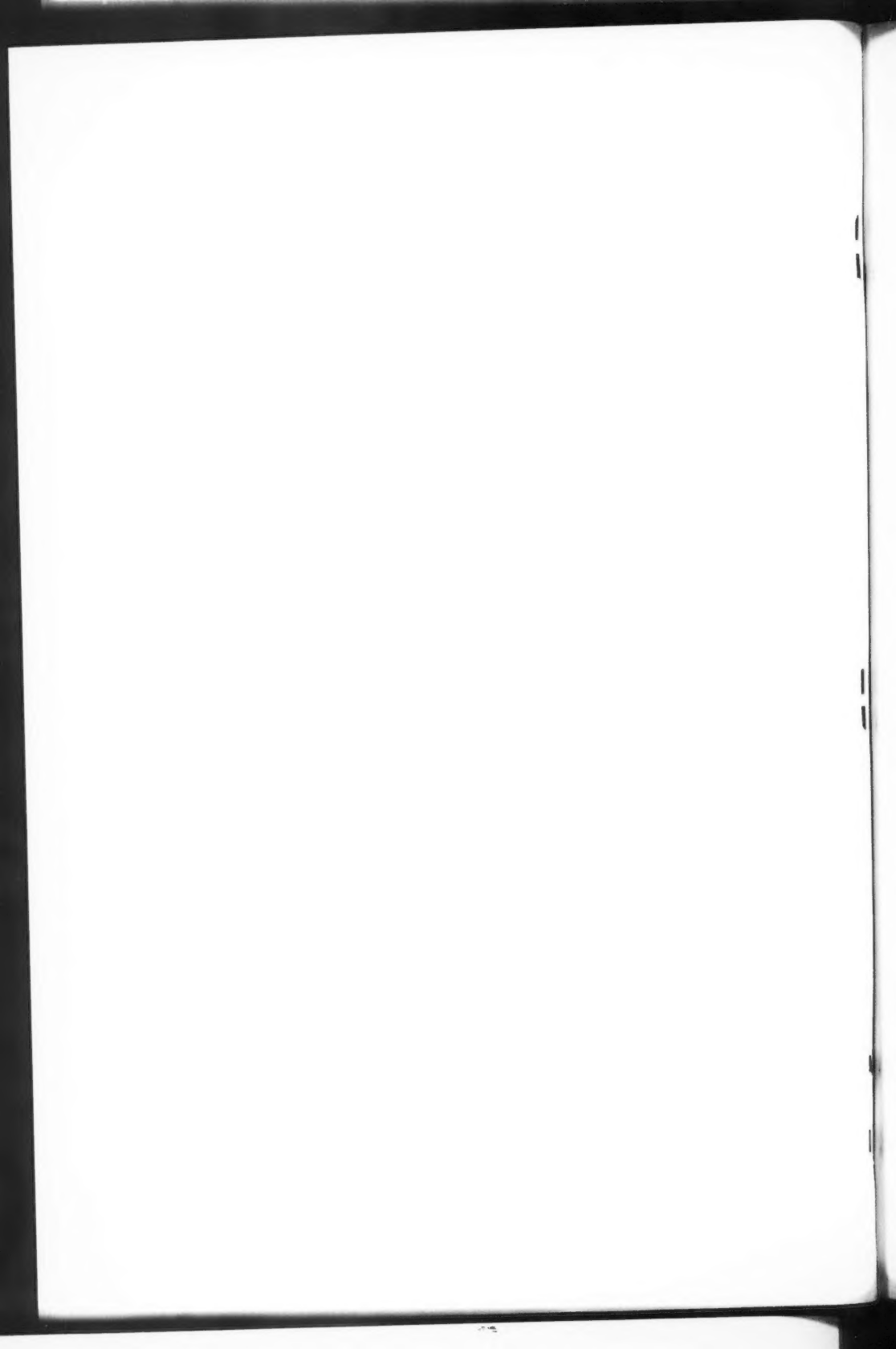
STUDENTS: A candidate for Studentship must be between the ages of 18 and 26, and pays an Annual Subscription of 5s. (\$0.75).

MEETINGS: Fellows and Students may attend all Meetings of the Society including the annual Exhibition of Scientific Instruments and Apparatus.

PUBLICATIONS include the *Proceedings of the Physical Society*, published monthly in two sections, and *Reports on Progress in Physics*, published annually. Volume XIX, 1956, is now available (price 50s. (\$7.15)). Members are entitled to receive any of the Publications at a reduced rate.

Further information can be obtained from:

THE PHYSICAL SOCIETY  
1, LOWTHER GARDENS, PRINCE CONSORT ROAD  
LONDON, S.W.7, ENGLAND



# CANADIAN JOURNAL OF PHYSICS

## Notes to Contributors

### Manuscripts

(i) **General.** Manuscripts, in English or French, should be typewritten, double spaced, on paper  $8\frac{1}{2} \times 11$  in. **The original and one copy are to be submitted.** Tables and captions for the figures should be placed at the end of the manuscript. Every sheet of the manuscript should be numbered.

Style, arrangement, spelling, and abbreviations should conform to the usage of this journal. Names of all simple compounds, rather than their formulas, should be used in the text. Greek letters or unusual signs should be written plainly or explained by marginal notes. Superscripts and subscripts must be legible and carefully placed.

Manuscripts and illustrations should be carefully checked before they are submitted. Authors will be charged for unnecessary deviations from the usual format and for changes made in the proof that are considered excessive or unnecessary.

(ii) **Abstract.** An abstract of not more than about 200 words, indicating the scope of the work and the principal findings, is required, except in Notes.

(iii) **References.** References should be listed **alphabetically by authors' names**, unnumbered, and typed after the text. The form of the citations should be that used in current issues of this journal; in references to papers in periodicals, titles should not be given and only initial page numbers are required. The names of periodicals should be abbreviated in the form given in the most recent *List of Periodicals Abstracted by Chemical Abstracts*. All citations should be checked with the original articles and each one referred to in the text by the authors' names and the year.

(iv) **Tables.** Tables should be numbered in roman numerals and each table referred to in the text. Titles should always be given but should be brief; column headings should be brief and descriptive matter in the tables confined to a minimum. Vertical rules should be used only when they are essential. Numerous small tables should be avoided.

### Illustrations

(i) **General.** All figures (including each figure of the plates) should be numbered consecutively from 1 up, in arabic numerals, and each figure referred to in the text. The author's name, title of the paper, and figure number should be written in the lower left corner of the sheets on which the illustrations appear. Captions should not be written on the illustrations (see Manuscripts (i)).

(ii) **Line Drawings.** Drawings should be carefully made with India ink on white drawing paper, blue tracing linen, or co-ordinate paper ruled in blue only; any co-ordinate lines that are to appear in the reproduction should be ruled in black ink. Paper ruled in green, yellow, or red should not be used unless it is desired to have all the co-ordinate lines show. All lines should be of sufficient thickness to reproduce well. Decimal points, periods, and stippled dots should be solid black circles large enough to be reduced if necessary. Letters and numerals should be neatly made, preferably with a stencil (**do NOT use typewriting**) and be of such size that the smallest lettering will be not less than 1 mm. high when reproduced in a cut 3 in. wide.

Many drawings are made too large; originals should not be more than 2 or 3 times the size of the desired reproduction. In large drawings or groups of drawings the ratio of height to width should conform to that of a journal page but the height should be adjusted to make allowance for the caption.

**The original drawings and one set of clear copies (e.g. small photographs) are to be submitted.**

(iii) **Photographs.** Prints should be made on glossy paper, with strong contrasts. They should be trimmed so that essential features only are shown and mounted carefully, with rubber cement, on white cardboard with no space or only a **very** small space (less than 1 mm.) between them. In mounting, full use of the space available should be made (to reduce the number of cuts required) and the ratio of height to width should correspond to that of a journal page ( $4\frac{1}{4} \times 7\frac{1}{2}$  in.); however, allowance must be made for the captions. Photographs or groups of photographs should not be more than 2 or 3 times the size of the desired reproduction.

**Photographs are to be submitted in duplicate;** if they are to be reproduced in groups one set should be mounted, the duplicate set unmounted.

### Reprints

A total of 50 reprints of each paper, without covers, are supplied free. Additional reprints, with or without covers, may be purchased.

Charges for reprints are based on the number of printed pages, which may be calculated approximately by multiplying by 0.6 the number of manuscript pages (double-spaced typewritten sheets,  $8\frac{1}{2} \times 11$  in.) and including the space occupied by illustrations. An additional charge is made for illustrations that appear as coated inserts. The cost per page is given on the reprint requisition which accompanies the galley.

Any reprints required in addition to those requested on the author's reprint requisition form must be ordered officially as soon as the paper has been accepted for publication.

## Contents

	Page
The Decay of $\text{Os}^{185}$ — <i>M. W. Johns, S. V. Nablo, and W. J. King</i>	1159
Meteor Signal Rates Observed in Forward-scatter— <i>E. L. Vogan and L. L. Campbell</i> - - - - -	1176
Scandium Isotope of Mass 42— <i>J. A. R. Cloutier and A. Henrikson</i>	1190
Time Reversal Effects in Muon Decay— <i>Robert T. Sharp and Glen Bach</i> - - - - -	1199
Ultraviolet Spectra of $\text{LiH}$ and $\text{LiD}$ — <i>R. Velasco</i> - - - -	1204
Reactor Neutron Capture Cross Section of 51-Day $\text{Sr}^{89}$ — <i>L. P. Roy and J. C. Roy</i> - - - - -	1215
Isotope Shift in the Resonance Lines of $\text{Mg I}$ — <i>F. M. Kelly</i> - -	1220
Growth Conditions for Stability of a Cellular Solid-Liquid Interface— <i>E. L. Holmes, J. W. Rutter, and W. C. Winegard</i> - -	1223
The Constitution of Nickel-Gallium Alloys in the Region 0-35 Atomic % Gallium— <i>W. B. Pearson and D. M. Rimek</i> -	1228
Vibration-Rotation Bands of Ammonia. II. The Molecular Dimensions and Harmonic Frequencies of Ammonia and Deuterated Ammonia— <i>W. S. Benedict and Earle K. Plyler</i>	1235
The Spectrum of the $\text{P}_2^+$ Molecule— <i>N. A. Narasimham</i> - -	1242
Notes:	
A Simple Rectangular Pulse Generator— <i>H. L. Armstrong</i> -	1250



